UNIVERSITÀ
DEGLI STUDI
DI PADOVA

Università degli Studi di Padova

Dipartimento di Scienze Chimiche

Dipartimento di Fisica e Astronomia "Galileo Galilei"

Corso di Laurea magistrale in
Material Science

Synthesis and optimization of nanocatalysts for the thermocatalytic reduction of CO2 into fuel

Relatore:

Prof.ssa Antonella Glisenti

Contro relatore:

Prof.ssa Sara Bonacchi

Laureanda:

Ambra Meneghello

Matricola: 1209934

ANNO ACCADEMICO 2022/2023

“Lo scienziato nel suo laboratorio non è solo un tecnico,
è anche un bambino davanti a fenomeni della Natura
che lo affascinano come un racconto di fate”.
La capacità di sorprendersi non deve svanire con il tempo,
ma per essere scienziati il ‘fanciullino’ che c’è in noi
deve perdurare nel tempo

Marie Curie

Summary

Abstract

In this thesis various metal oxides have been employed to tackle the issue of atmospheric pollution with the final perspective of climate change mitigation.

Efforts have been devoted to the abatement of CO_2 deriving from energy production. The final aim is to valorize carbon dioxide by producing an easily usable fuel, methane, through a highly selective and efficient process. The advantages are several: firstly, this allows to decrease its concentration in the atmosphere, while also allowing the production of a valuable fuel, with well established applications, closing the carbon cycle.

Extensive characterization of the materials developed allowed to correlate such results with their catalytic activity performance, shedding light on the mechanisms involved while also giving fundamental clues about methods to enhance their catalytic performance.

Together with conventional approaches to heterogeneous catalysis techniques, an innovative procedure was developed to incorporate nickel and copper (the active catalysts) into a perovskite support. The support was chosen in order to maximize the catalytic performance while minimizing the use of Platinum Group Metals that nowadays represent critical raw materials, both in terms of supply are recycling potential.

I. Introduction

In the latest decade, sustainable energy production has become a topical issue, with an increasing shift in energy production towards more sustainable, renewable energy sources. Nonetheless, non-renewable energy sources still contribute for the predominant share of the energy produced worldwide.

The rapid and consistent increase in world population (Figure 1– which is expected to reach 8.6 bilion in 2030, 9.9 bilion in 2050 and 11.6 bilion in 2100 according to the UN 2012 Revision of World Population Prospects (https://population.un.org/wpp/) - together with the overall increase in global population density and urbanization – a worldwide phenomenon, through mainly taking place in the least developed countries (https://ourworldindata.org/urbanization#what-share-of-people-will-live-in-urban-areas-in-the-future) – poses urgent challenges to satisfying the increasing demand of materials and energy, while also maintaining good environmental standards.

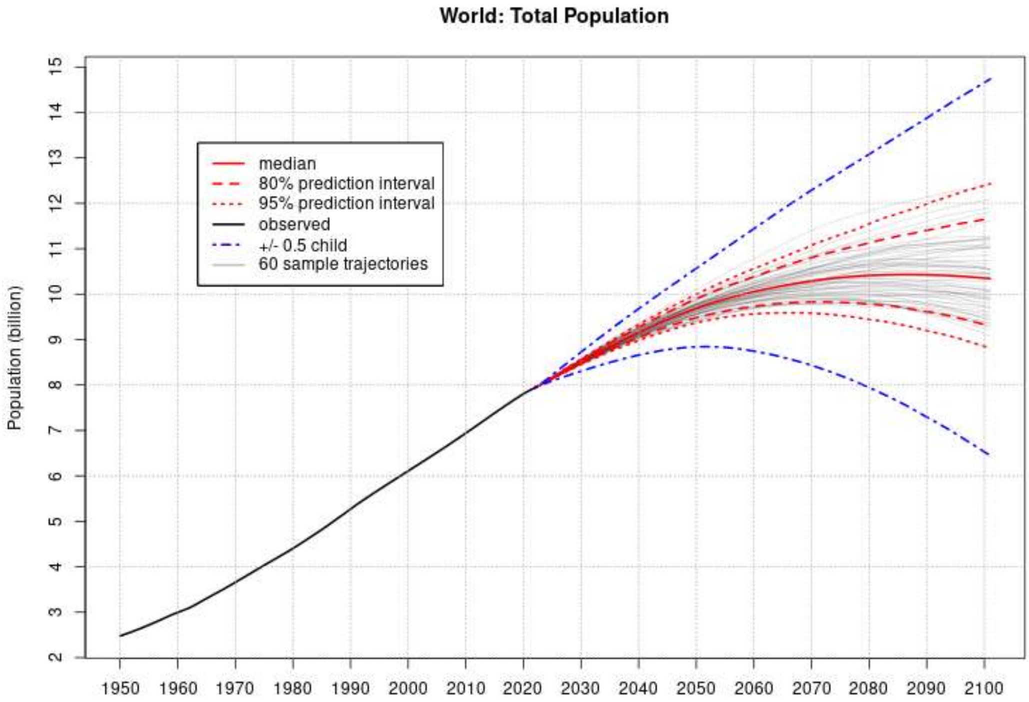
World: Total Population

© 2022 United Nations, DESA, Population Division. Licensed under Creative Commons license CC BY 3.0 IGO.
United Nations, DESA, Population Division. *World Population Prospects 2022*. http://population.un.org/wpp/

Figure 1: 2022 World Population Projection (source: UN)

Together with the increasing use of renewable energy sources, several efforts at the national and international scale are being made in the context of energy efficiently to reduce energy needs, which in the turn would reduce the environmental drawbacks related to energy production: but also in the context of cleaner energy production: regarding the latter issue, it is worth mentioning that clean energy is the seventh of the 17 UN Sustainable Development Goals (Figure 2).

Moreover, the energy issue is especially critical regarding political and economic balances: for this reason, a highly diversified energy mix plays a fundamental role in establishing more stable energy systems.

Figure 2: The 17 Sustainable Development Goals

Although clean energy source – e.g. solar energy, wind energy, hydropower – are deemed to cause lesser CO_2 emissions, the use of these types of installation is often linked with several issues of different nature, such as their low energy density – i.e. the need for larger plants compared to non-renewable source based energy plants – but also technical difficulties in locating new plants appropriately, either because of natural constraints – e.g. solar radiation, wind velocity, etc. – or because of the lack of an appropriate electrical network to receive the energy produced.

Regarding the latter issue, a more interesting perspective is offered by the use of energy in order to produce renewable fuels starting from industrial, agricultural or civil waste: in this context, a very strong incentive is being given by national governments toward the production of "sustainable fuels", i.e. fuels which are produced by means of chemical or biological processes, thus reducing CO_2 emission related to the production of new fuels while reducing the amount of residual waste and closing the carbon cycle.

The production of fuels instead of electrical energy is particularly interesting, since it solves several of the issues related with electrical energy production:

- Fuel production plants can be much smaller than renewable energy plants while delivering the same energy output;
- Fuel production plants output a fuel which can be easily transported where needed by trucks: although some emissions are produced for the transportation of the product, this aspect eliminates the need of a adequate electric network for the marketing of energy, while also eliminating the issue of energy losses by delivery;
- Because of their nature, fuel production plants do not pose particular issues regarding their placement, as long as an adequate infrastructure is available for their operation;
- Because of their nature, fuel production plants also integrate in a very interesting way within the context of already existing industrial areas – in this sense, fuel production can also constitute an example of industrial symbiosis, as their input materials can also be represented by waste produced by the surrounding manufactures.

In the context of a circular economy model, the production of sustainable fuels constitutes a form of recycling, as less raw materials are needed to produce new energy and less emissions and wastes are produced.

Although the adoption of a circular economy model (Figure 3) is fundamental at the global scale from the environmental point of view, it is also worth mentioning that the reduction in emissions and wastes would be strongly evident on the local scale itself with regard to several other aspects; as an example, recycling of industrial waste reduces the small scale impact of local industries, while also giving new value to materials which would be otherwise disposed of an reducing the need for external energy, which in turn facilitates the energy system management at a wider scale.

Figure 3: Circular Economy model diagram

In light of the consideration expressed, the following work constitutes an example of research in the field of sustainable fuel production, as it focuses on the development, optimization and testing of catalyst supported on perovskites for the thermos-catalytic reduction of carbon dioxide (CO_2) in the presence of hydrogen (H_2), with the consequent production of methane (CH_4), carbon monoxide (CO) or methyl alcohol (CH_3OH).

An interesting aspect which characterizes the work performed for this study is the analysis of non-noble metals, such as copper (Cu) and nichel (Ni), as the materials chosen for the role of catalyst: although this choice affects the system performance, it is still very interesting from an industrial point of view, as it is deemed to drastically lower the cost of manufacturing of the proposed device.

1. CO_2 reduction reaction

With regard to the aforementioned issues, the use of CO_2 is receiving increasing interest in both the scientific and industrial communities, in part due to climate change considerations and because the use of carbon dioxide could eventually be the starting point for cheaper and more efficient production of synthetic fuels less impactful than conventional fossil fuels. However, this is only possible if the cost of these processes becomes cheaper and if the overall sustainability is preserved (1). Carbon dioxide is produced and released in industrial processes, power generation, biomass combustion and gasification, cement kilns and oil refinery.

Emissions of CO_2 (GHGs in general) are the main driver of climate change: just to give some reference data, the concentration of CO_2 in the atmosphere has increased from about 277 ppm in 1750, the beginning of the industrial age, to 405ppm in 2017; moreover, the flow of carbon into the atmosphere has reached a worrying value of 34Gt CO_2 year^{-1}. The drastic increase in the concentration of CO_2 is held to be the main driver for the increase in the Earth's temperature (2). This urgency has repercussions on the scientific community, which is now called upon to provide an effective solution to this universal problem.

While climate change is a fundamental issue to be solved, the need to obtain consistent and stable energy production is rapidly becoming another critical factor to be considered: in this perspective, one of the approaches that have been proposed is the so-called Power-to-Gas.

Power-to-Gas (PtG) is an option for producing fuel gases by using electric and thermal energy and thus for storing energy it into chemical bonds. This method allows to solve some of the main issues linked with electrical energy production, e.g. energy losses during the transportation of electricity.

Using electricity, an electrolyser splits water into its two components: oxygen on the one hand and hydrogen on the other. The hydrogen can now be fed into a downstream methanation process (3). This technology is currently considered useful because it is the most cost-effective long-term storage option for energy: as a matter of fact, renewable energy sources are typically discontinuous over time and often geographically remote from energy consumers (e.g. solar, wind, wave energy sources). This technology also supports cross-sectorial decarbonization and the replacement of fossil energy carriers. The literature shows that, with renewable energy production on the rise, long-term storage with PtG will become necessary and cost-effective. (3). In this project, hydrogen (in principle green hydrogen) is used for direct conversion of CO_2 to methane by means of the Sabatier reaction, which only provides water as a side product:

$$CO_2 + H_2 \rightarrow CH_4 + 2H_2O$$

The main advantage of obtaining methane lies in its already existing distribution infrastructure and high energy content. Well aware of the fact that methane belongs to the greenhouse gas family, the methane produced from the recycling of carbon dioxide is actually less harmful than natural fossil methane as it helps to reduce global greenhouse gas emissions by reducing the use of new carbon which was previously stored in the Earth's crust. Carbon dioxide methanation has a wide range of applications including purification of synthesis gas for ammonia production and syngas production (4). The National Aeronautics and Space Administration (NASA) has considerable interest in the applications of this reaction in manned space colonization on Mars. (5)

In order to maximize the efficiency of the Sabatier reaction, temperature must be kept between 200°C and 500°C to avoid the water gas reverse displacement reaction:

$$CO_2 + H_2 \rightarrow CO + H_2O$$

which occurs at higher temperatures. A calculation of the thermodynamic constraints at the reaction conditions gave the results shown in the graph below, Figure 4.

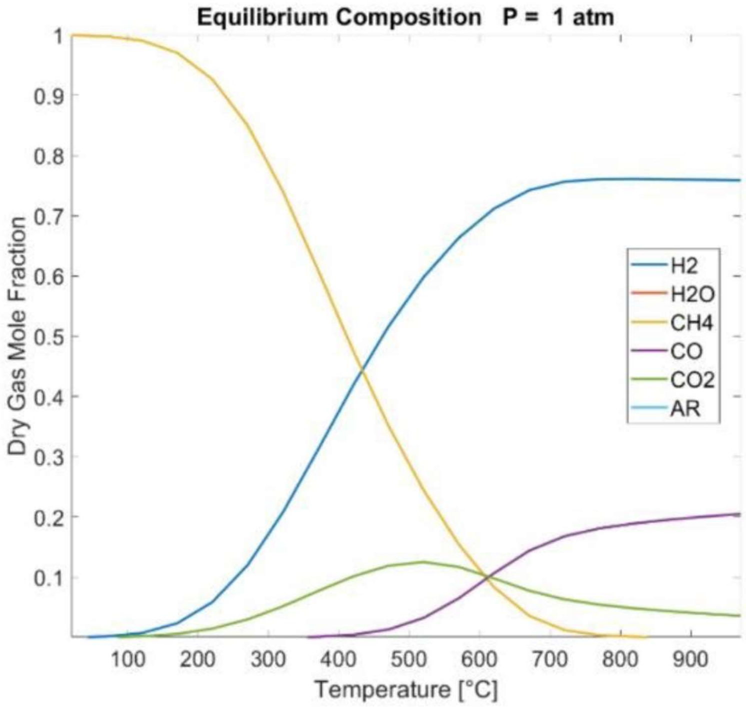

Figure 4: Theoretical composition at equilibrium of the mixture of reagents for the methanation of CO2 at 1atm.

As it can be seen from the graph, CO concentration starts to rise above 500°C in a dry mixture of reactants and products, which means that the water gas backshift reaction is favored over methanation, resulting in lower methane yield.

Moreover, the conversion of CO_2 to methane presents many challenges because CO_2 is a linear molecule with two double bonds between carbon and oxygen atoms and is a very stable molecule. In fact, its free Gibbs energy is very high (ΔG^0 = -400 kJ/mol) and, therefore, a substantial energy input, optimized reaction conditions and catalysts with high stability and activity are required (6).

Different processes are available to produce methane from CO_2 such as thermal catalytic, electrocatalytic, photocatalytic and photoelectrocatalytic ones (Figure 5). In this work, the thermocatalytic process has been chosen due to their potential sustainable development and the possible synergism in the fundamental of catalysis.

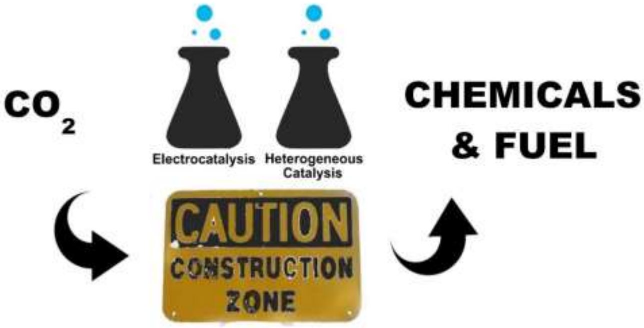

Figure 5: Heterogeneous catalysis

Direct conversion of CO_2 and hydrogen to CH_4 can be achieved with higher selectivity and lower reaction temperature than hydrogenation of CO.

However, the CO_2 hydrogenation reaction depends on the development of an effective catalyst, since the same catalysts used in commercial processes for CO hydrogenation ($Cu/ZnO/Al_2O_3$) are not as effective at hydrogenating CO_2 to methane under similar operating conditions. For this reason, the direct conversion of CO_2 and hydrogen to CH_4 has been extensively investigated, looking for different catalyst compositions and preparation methods. Extensive experimental and theoretical investigations of the hydrogenation of CO_2 have been conducted in recent decades.

2. Perovskite support

Thermocatalitic reactions are obtained by introducing a mixture of gases inside a high temperature reactor: inside the reactor, the reaction is facilitated through the use of a catalyst, which has been previously deposited on a stable support material. Throughout this thesis, perovskite ($LaFeO_3$) was chosen as the support material.

The naturally occurring perovskite mineral, $CaTiO_3$, has simple origins, but the perovskites' structure, characterized by a general chemical formula of ABX_3 (7), is rather complex:

- A: mono-, di- and/or trivalent cations
- B: tri-, tetra- and pentavalent ions
- X: mono-, di- and trivalent anions

The ideal cubic crystal structure of perovskite consists of compact AX_3 layers with ¼ of the octahedral holes filled with B-site cations. The A-site cation is usually large and coordinated by 12 anions, while the B-site is small and octahedrally coordinated by anions. The B-site octahedra form a structure in which they share corners, and depending on the size of the B-site cation, different interstitial spaces are created that can accommodate different A-site cations of the ion radius in the perovskite framework.

The crystal structure of a cubit perovskite $ABO_3 \approx SrTiO_3$ is shown in Figure 6. The ideal cubic perovskite structure is not very common due to the lack of cations with ideal ionic radii in their ideal crystallographic sites. When the A-site cation is smaller than the Sr^{2+} ion, a phenomenon known as octahedral tilt occurs. This leads to structural changes that produce interesting electrical and magnetic properties. As the perovskite structure deviates from the ideal cubic shape, octahedral inclinations act to stabilize the structure and grade.

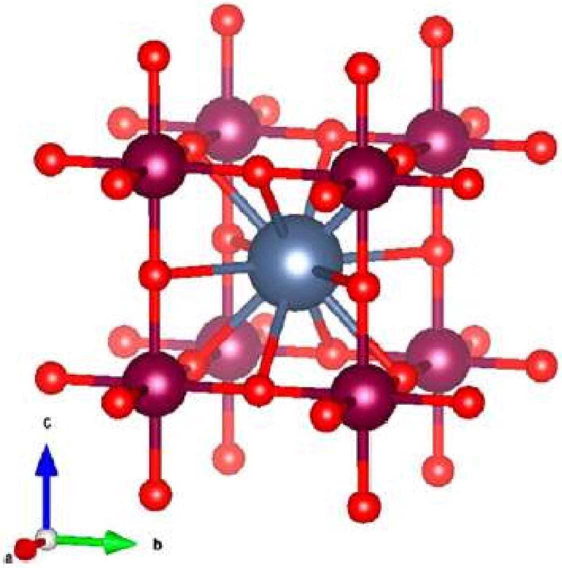

Figure 6: Primitive cubic perovskite (ABO3) unit cell of SrTiO3 (Sr: blue, Ti: purple, O: red)

In order to determine the stability of possible perovskite materials, Goldschmidt developed a formula that uses the geometric structural identity of the perovskite structure and the ionic radii of the A- and B-site cations (r_A and r_B) and anion (r_O). (8). The Goldschmidt tolerance factor (t) is defined as

$$t = \frac{r_A + r_O}{\sqrt{2}(r_B + r_O)}$$

The Goldschmidt tolerance factor when equal to 1 represents an ideal cubic perovskite. If the number falls below 0.9, the structure shifts towards an orthorhombic or rhombohedral distortion caused by a different octahedral tilt. When the tolerance factor is greater than 1, the perovskite structure typically shifts towards a tetragonal or hexagonal distortion.

2.1 Structural characteristics of $LaFeO_3$

The structure of the perovskite crystal lattice greatly impacts the stability of the material to changes in pressure and temperature, as well as its electric characteristics – e.g. its ability to transport oxygen ions.

The undoped $LaFeO_3$ structure adopts an orthorhombic perovskite arrangement (Pbnm space group No. 62) at room temperature up to about 957°C.

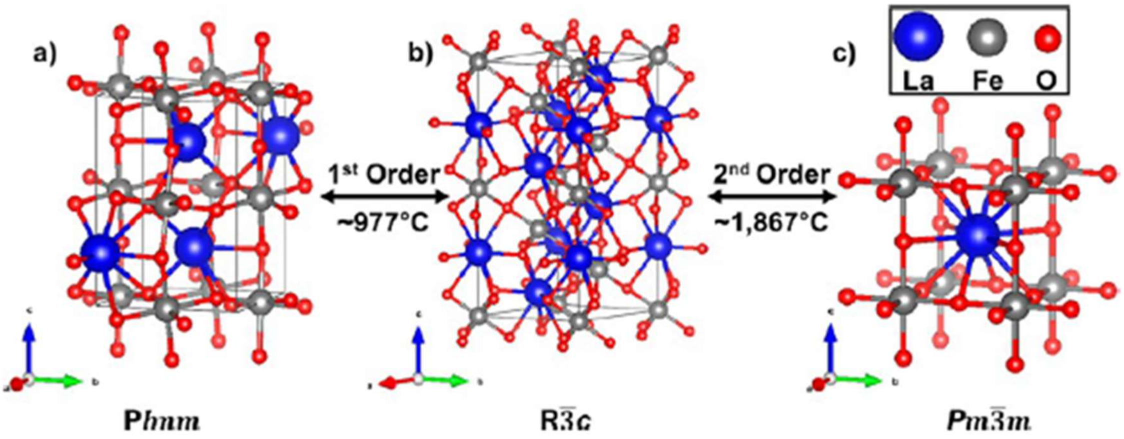

Figure 7: Perovskite structure of LaFeO3 adopting three distinct phases, (a) a low-temperature orthorhombic phase (Pbnm), (b) a high-temperature rhombohedral phase ($R\bar{3}c$), and (c) a high-temperature cubic phase ($Pm\bar{3}m$).

The crystal structure of $LaFeO_3$ is shown in Figure 7 (9). The unit cell at room temperature has four structural units (Z=4) and edge lengths of a=5.55 Å, b=5.56 Å and c=7.86 Å. Table 1 lists the structural parameters of the perovskite with the space group Pbnm.

Table 1: Crystallographic data for LaFeO3 in the Pbnm space group

Elemento	Simbolo Wyckoff	x	y	z	Occupazione
Lantanio (La)	4c	-0.00614	0.02840	1/4	1
Ferro (Fe)	4b	0	1/2	0	1
Ossigeno (O1)	4c	0.0731	0.4875	1/4	1
Ossigeno (O2)	8d	-0.2809	0.2815	0.0394	1

There are two inequivalent atomic positions of oxygen; the first oxygen (O1) is tetrahedrally coordinated by two lanthanum cations and two iron cations and is located within the lanthanum layers, and the second oxygen (O2) is coordinated by three lanthanum cations and two iron cations and it is found between the layers of iron. The Goldschmidt tolerance factor for $LaFeO_3$ is 0.9543, which indicates that this material should crystallize in the cubic perovskite structure. This deviation from the cubic shape is commonly caused by the fact that the A-site cation is too small to fit into the B-site cation gaps. The structure is stabilized by neighboring octahedra leaning in opposite directions.

The unit cell can be related to a pseudocubic perovskite lattice a ≈ b ≈21/2ap and c≈2ap. The expansion of the unit cell correlates with the degree of octahedral tilt observed. The nature of the octahedral tilt observed in LaFeO3 was discussed by Woodward as being caused by a strong covalent bond interaction between lanthanum and oxygen, and the structure distorts to maximize the degree of orbital overlap.

$LaFeO_3$ undergoes a first order orthorhombic to rhombohedral structural phase transition between ~960 and ~1005 °C (Figure 8). The nature of this nonlinear thermal expansion can be explained by the octahedral tilt of the B-site cations, which can be further related to the observed magnetic properties.

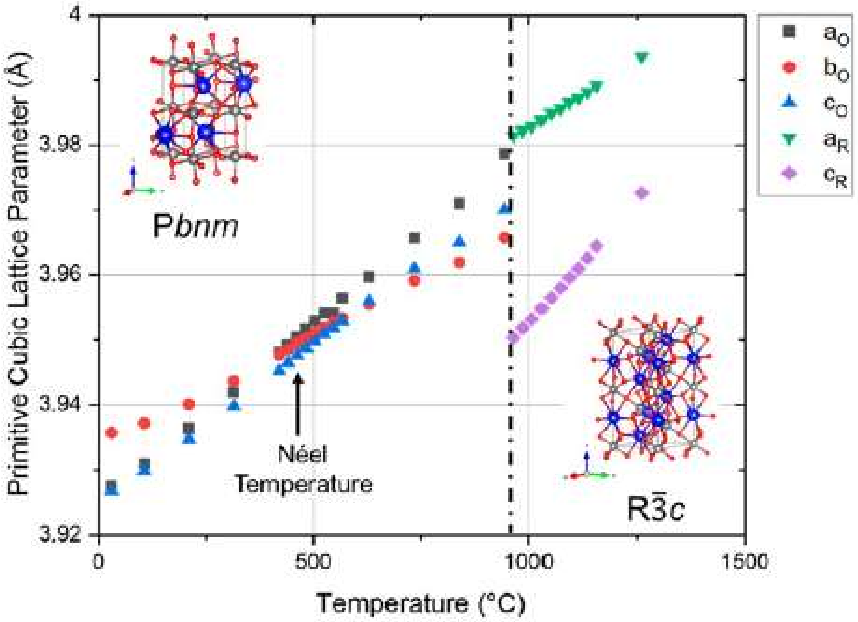

Figure 8: Nonlinear thermal expansion of lattice parameters observable in primitive cubic lattice parameters between 30 and 1200 °C. The dotted line marks the phase transition from orthorhombic (Pbnm) to rhombohedral (R$\bar{3}$c) at 966 °C. The Neel transition was marked at 462°C. (10)

2.2 Role of the A site doping in the properties of the LaFeO3 phase

The A site is typically doped with alkaline earth ions to control the ionic conductivity of the doped $LaFeO_3$ material. A-site substitution necessary to ensure that CO_2 reduction is driven efficiently, as diffusion of oxygen through the crystal structure is limited. Sr doping is typically preferred over Ca and Ba due to higher overall conductivity, which is intensified by higher solubility limits and disorder caused by mismatching cation ionic radii.

Alkaline earth cations (Ca^{2+}, Sr^{2+}, Ba^{2+}) are the most common A-site dopants. The ionic radius of calcium is very close to that of lanthanum, while strontium and barium are much larger. The most common dopant used to manipulate the ionic conductivity for this material is Strontium which has an ionic radius greater than ~0.1 Å and forms more ionic bonds with oxygen. $LaFeO_3$ has two compensating mechanisms which can occur when the material is replaced with cations of lower valence: iron can change its valence or oxygen vacancies can be created; the combination of both is possible. Therefore, the incorporation of these dopants is typically used to control the ionic conductivity of the material. Strontium has a higher solubility limit and increases the conductivity of oxide ions more than calcium and barium.

When Sr is inserted into the structure of $LaFeO_3$ ($La_{1-x}Sr_xFeO_{3-\delta}$), it appears to randomly disperse at the A site of the perovskite lattice, as no cation or oxygen vacancy order is observed. The solubility of Sr in $LaFeO_3$ is quite unique as several phase transitions and two-phase regions are involved.

Doping with Ca in $LaFeO_3$ offers a unique opportunity to study the effect of defects on the structure without changing the size of the A site cation.

The Ba-substituted $LaBaFeO_3$ crystallizes in the primitive cubic space group $Pm\bar{3}m$ (#221) with a unit cell edge length of a = 3.935 Å and a formula unit per unit cell (Z = 1). The A-site cations have polyhedral units that share faces. Neither the order of site A nor site B cations was observed. The addition of Ba to the LaFeO3 lattice greatly increases the bond length between site A and oxygen to accommodate the larger cation, and the mean bond length between the B site and oxygen shortens slightly (Table 2) (7)

Table 2: Average bond lengths between iron and oxygen which can be observed to shrink when any group II cation is doped at the lanthanum site while the average bond length between the A site (La and Ca, Sr or Ba) and oxygen increases as function of cation size and cation mismatch (Ca first grows and then shrinks after x = 0.20)

Composizione	Lunghezza media del legame Fe–O (Å)	Lunghezza media del legame A–O (Å)	Angoli di legame Fe–O–Fe (deg)	Volume standardizzato (Å)
$LaFeO_3$	2.006	2.605	156.3	60.756
$La_{0.90}Ca_{0.10}FeO_3$	1.995	2.604	155.9	60.115
$La_{0.80}Ca_{0.20}FeO_3$	1.989	2.610	157.2	59.821
$La_{0.667}Ca_{0.333}FeO_3$	1.983	2.593	157.4	58.817
$La_{0.90}Sr_{0.10}FeO_3$	1.946	2.557	157.9	56.205
$La_{0.80}Sr_{0.20}FeO_3$	1.983	2.623	166.7	60.3975
$La_{0.60}Sr_{0.40}FeO_3$	1.976	2.646	172.9	59.99
$La_{0.50}Sr_{0.50}FeO_3$	1.962	2.681	166.32	59.1817
$La_{0.40}Sr_{0.60}FeO_3$	1.953	2.688	168.70	58.8117
$La_{0.30}Sr_{0.70}FeO_3$	1.945	2.745	171.35	58.4183
$La_{0.50}Ba_{0.50}FeO_3$	1.937	2.738	175.69	58.0267

2.3 Role of the B site doping in the properties of the LaFeO3 phase

Site B is responsible for the catalytic sequestration of CO_2 and electron transfer that initiates the reduction of CO_2 into useful chemical streams. The use of multivalent cations at site B helps improving both the electronic conductivity of the material and the transfer of electrons between the electrode material and the feed gas.

The B site of $LaFeO_3$ is commonly doped with transition metal cations due to similar ionic radii between the dopant and iron. The most common dopants are Co and Ni as these late transition metals can change the structure from orthorhombic to rhombohedral.

The solid solution between $LaFeO_3$ and $LaNiO_3$ is regular with a phase transition of the composition around the 50−50 composition from Pnma to $R\bar{3}c$ (11). This composition commonly exhibits both phases, due to a first order phase transition near room temperature; the structure is orthorhombic below ∼27 °C and rhombohedral above ∼27 °C.

3. Nanocatalysts

For the reaction studied in this work, heterogeneous catalysts were used, which consist of three main components: active phase, support and promoter. An active phase is the part of the catalyst where the reaction takes place, generally transition metals (in this case Ni and Cu) are preferred due to their unique ability to catalyze reactions. Due to the multiplicity of low energy surface electronic states, transition metals can readily accept or donate electrons thus facilitating the breaking or formation of chemical bonds on the surface. (12)

For many heterogeneous reactions, the formation of metal nanocatalyst particles with effective control over size and morphology and their subsequent immobilization on a suitable support have both proven effective ways to increase catalyst activity and selectivity. However, the methodology for obtaining supported metal nanocatalysts with simultaneously enhanced activity and stability is of vital importance and remains a challenging goal, because many factors (e.g., surface morphology, electronic structure, and metal-support interaction) would significantly influence catalytic performance. Concerning the catalytic reactions, it is known that the surface defects of the nanocatalysts, acting as the active sites play a decisive role in the adsorption and reactivity. The formation or introduction of abundant and specific sites/defects on the surface of supported nanocatalysts is a promising approach for tailoring surface morphology and electronic structure to enhance heterogeneous catalytic activity.

Although nanoparticles immobilized on various supports via physicochemical deposition pathways often suffer from rapid deactivation (especially at high temperatures) due to nanoparticle sintering and/or aggregation, it has been hypothesized that nanoparticle migration or sintering is to be significantly inhibited if a strong interaction (e.g. a covalent bond) is involved between the metal nanoparticles and the support.

Given the two problems discussed above, an effective immobilization approach and adequate support are two key factors in the design and fabrication of highly efficient supported metal nanocatalysts.

Noble metals (e.g. Ru, Rh and Pd) have been shown to be the most effective catalysts for CO_2 methanation under relatively mild temperature and pressure conditions, but their high cost and limited availability limit their practical applications.

Therefore, this work has focused on the study of non-noble metal catalysts. Since transition metal-based catalysts exhibit lower activity than noble metals, it is critical to find ways to fabricate supported transition metal catalysts characterized by stability and with excellent activity for CO2 methanation, in order to make replacement of transition metals more cost-effective. (13)

Among transition metals, in general, Ni-based catalysts are more active than Cu-based catalysts in the temperature range 500-700°C. Another relevant aspect concerns the particles size and morphology. For the supported nickel catalyst, the optimal particle domain size was observed to decrease with increasing temperature. Particle size has a significant impact on the reaction rate. It is likely that a self-organizing system could adjust the appropriate particle size to match the reaction conditions. Support materials can be strategically chosen to control catalyst particle size and dispersion by physical interactions (porous support) or chemical interactions (charge transfer effect).

Cu nanoparticles (NPs) are of particular interest due to the natural abundance and relatively low cost of copper (with respect to noble metals) and the multiple practical and direct ways of preparing Cu-based nanomaterials.

Despite the strong background on the applications of bulk Cu in various fields, the use of Cu NPs is limited by the intrinsic instability of copper under atmospheric conditions, which makes it subject to oxidation.

Copper is a 3d transition metal and has some interesting physical and chemical properties. Cu-based materials can promote and undergo a variety of reactions due to Cu's wide range of accessible oxidation states (Cu0, CuI, CuII, CuIII), which allow for reactivity through one- and two-electron pathways.

An inexpensive way to create advanced Cu-based nanomaterials for catalysis is to anchor copper NPs on supports. Additionally, Cu's high boiling point makes it compatible with high temperature and high pressure chemical reactions. (14)

Compared to elemental Ni, supported Ni-Cu catalysts have been extensively studied, and a great improvement in the stability of supported Ni-Cu compared to supported Ni catalyst has generally been observed. Beside stability the co-presence of Ni and Cu seems also to un-favor Ni C-poisoning. Cunha et al. investigated the effect of copper in nickel catalysts and stated that the formation of encapsulating carbon on nickel can be prevented by "ensemble control". This resulted in the dilution of the active metal phase with an inactive phase (Cu), separating the Ni active sites from each other and thus reducing the rate of encapsulation carbon formation. The complex role played by Ni and Cu makes difficult to identify the optimal Ni/Cu ratio which is still a debated question. (15)

II. Experimental approach

1. Synthetic approach

For the assessment of the influence of Ni and Cu catalysts presence and type on the Sabatier reaction, twelve different samples based on $LaFeO_3$ have been synthesized: three of the samples were not doped during the synthesis phase, while the remaining samples have been doped during the synthesis procedure. The nine doped samples differ with regard to the different type of catalyst (Cu, Ni and the NiCu alloy) and the presence or absence of the dopant element in B.

To observe the different effects of doping procedure on the catalytic activity, two different methods of insertion of the Ni/Cu were tried. At first three samples were obtained by depositing the active species on the $LaFeO_3$ support prepared with the sol-gel method. The other samples were always synthesized with the sol-gel method, but inserting the dopants inside the solution of precursors. Once obtained the precursor perovskite, the active specie (Ni and/or Cu) are pushed on surface by ex-solution.

As can be seen in table 3, a substoichiometric lanthanum perovskite was produced, obtaining the formulas $La_{0,9}FeO_3$. This also alters the oxygen balance by altering the La/Fe ratio in the perovskite lattice itself. The reason for the non-stoichiometric is the ability to more easily release oxygen, increasing activity compared to stoichiometric perovskites, as well as reducing the segregation of lanthanum oxide on the sample surface.

Table 3: Sample list and legend

SAMPLES		
LFO_1	$La_{0.9}FeO_3$	Synthesis by sol-gel method
LFO_2	$La_{0.9}FeO_3$	Synthesis by sol-gel method
LFO_3	$La_{0.9}FeO_3$	Synthesis by sol-gel method
LFO_a1	$Ni/La_{0.9}FeO_3$	Synthesis as for sample LFO1+Ni deposition by template impregnation
LFO_a2	$Cu/La_{0.9}FeO_3$	Synthesis as for sample LFO1+Cu deposition by template impregnation
LFO_a3	$NiCu/La_{0.9}FeO_3$	Synthesis as for sample LFO1+NiCu deposition by template impregnation
LFNO_b1	$La_{0.9}FeNi_{0.05}O_3$	Synthesis by sol-gel method of Ni doped LFO with direct doping
LFCO_b2	$La_{0.9}FeCu_{0.05}O_3$	Synthesis by sol-gel method of Cu doped LFO with direct doping
LFCNO_b3	$La_{0.9}FeNi_{0.025}Cu_{0.025}O_3$	Synthesis by sol-gel method of NiCu doped LFO with direct doping
LBFNO_c1	$La_{0.9}\ Ba_{0.1}FeNi_{00.5}O_3$	Synthesis by sol-gel method of LFO doped Ni, in B, and Ba, in A, with direct doping
LBFCO_c2	$La_{0.9}\ Ba_{0.1}FeCu_{0.05}O_3$	Synthesis by sol-gel method of LFO doped Cu, in B, and Ba, in A, with direct doping
LBFCNO_c3	$La_{0.9}\ Ba_{0.1}FeNi_{0.025}Cu_{0.025}O_3$	Synthesis by sol-gel method of LFO doped NiCu, in B, and Ba, in A, with direct doping

There are several methods for the synthesis of perovskites:

- Co-precipitation method: involves the precipitation of metal in the form of hydroxide from a salt precursor with the help of a base in a solvent. The controlled release of anions and cations helps regulate the nucleation and growth kinetics of the particles
- Solid-state reactions: using solid-state reactions, perovskites can be synthesized by mixing B-site oxides or carbonates and metal A ions in the perovskite formula ABO_3 in the stoichiometric proportion
- Hydrothermal synthesis: is a method of synthesis of single crystals which depends on the solubility of minerals in high pressure hot water.
- Pechini method: it is a two-stage synthesis method, the first is chelation in an acidic environment and the second is polymerization in an alcoholic solution
- Gas phase preparations: cooling a dense saturated gas under specific conditions induces the nucleation and growth of nanoparticles as the gas condenses
- Sol-gel method: there is the synthesis of colloidal solutions (sol) which constitute the precursors for the subsequent formation of a gel. Thermal post-treatments are employed to remove the liquid phase from the gel, promote further condensation and increase the mechanical properties.
- Low temperature solution combustion method: it is based on the gelation of organic fuel and on the combustion of an aqueous solution containing salts of the desired metals, giving a voluminous and soft product with a large surface area
- Microwave synthesis: the use of microwave irradiation is a promising alternative heat source for the synthesis of perovskite oxides, this heat source is used in combination with the methods described in this slide
- Roll of PVD methods – laser ablation, MBE
- Wet chemical methods (solution preparation): this procedure involves the preparation of sol-gels, the co-precipitation of metal ions using different precipitating agents and heat treatment

1.1 Sol-gel method

In this work the sol-gel method has been exploited, as it is one of the simplest techniques to synthesize high quality nano and microstructures.

Furthermore, this method offers several advantages over other synthesis routes such as control over the structure, size and surface properties of materials, ease of implementation, low cost, high quality and production of materials with large surface.

For the preparation of the materials, the sol-gel method is performed using citric acid as a complexant – Figure 9 (16).

A stoichiometric amount of precursors cations are dissolved in about 80ml of distilled water. Distilled water is used to avoid introducing impurities and contaminating the synthesized sample. Following dissolution, citric acid monohydrate is added; citric acid is used as a chelating agent. We work with a metal ion/citric acid molar ratio of 1/2. Using a plate with magnetic stirrer, the solution is continuously mixed and brought to 120°C. After about 12 hours, part of the solution has evaporated, there is an increase in viscosity due to the chelating effect of the acid and a gel is obtained.

We proceed with the dehydration process, increasing the temperature to 300°C until a powder is obtained. Finally, after breaking in the mortar to obtain a material with a finer particle size, we continue with the calcination. Work is carried out with a ramp of 5°C/min from room temperature up to 600°C, followed by a 6-hour hold at this temperature. In the calcination phase, the volatile components still present are eliminated and the active catalyst is obtained which will be used in subsequent tests. Temperature and duration of calcination, influence the catalytic properties, the specific surface area and, above all, the thermal stability of the catalyst. In general, the calcination temperature is chosen considering the need of obtaining the correct crystalline phase while minimizing sintering and the reduction of specific surface area. Moreover, the working conditions to which the catalyst will have to be exposed, have also to be considered, so as not to have significant variations of the initial structure due to the thermal effect during the test or in real applications.

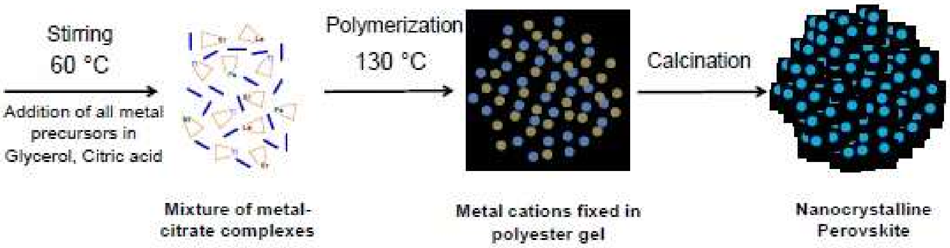

Figure 9: Formation mechanism of mesoporous perovskite oxides via a sol-gel route. Citric acid molecules in the initial mixture polymerize to form a gel with fixed and highly distributed metal cations. This gel yields a porous nanocrystalline perovskite after calcination.

The figure 10-12 show the images of the synthesized samples relating to the evaporation, dehydration and calcination phase:

Figure 10: Dissolution of perovskite precursors and gel formation

Figure 11: Perovskite after the dehydration step

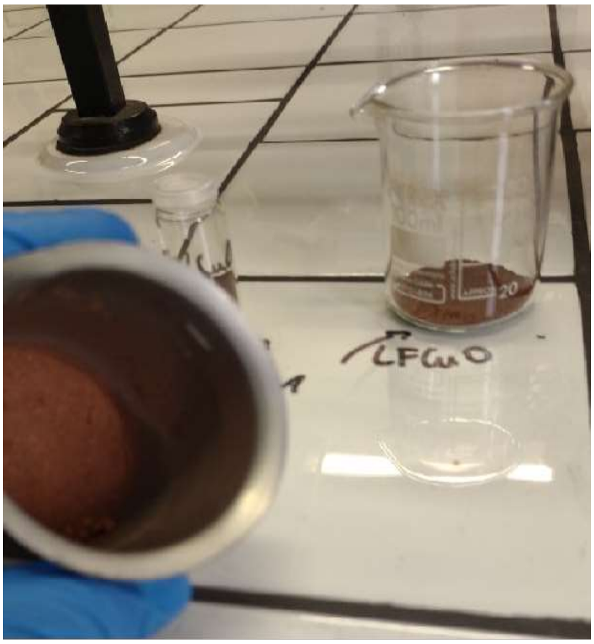

Figure 12: Perovskite after the calcination step

Tables 4-6 show in detail the quantities in grams of the precursors: Oxides of lanthanum and barium, nitrates of iron, copper and nickel, citric acid.

Table 4: Quantities of precursors for the sol-gel synthesis of undoped perovskite

	Theoretical quantity required	**LFO 1**	**LFO 2**	**LFO 3**
La_2O_3	3,22 g	3,21 g	3,21 g	3,21 g
$Fe(NO_3)_3$	8,86 g	8,86 g	8,86 g	8,86 g
$C_6H_8O_7$	13,08 g	17,62 g	13,09 g	13,08 g

Table 5: Quantities of precursors for the sol-gel synthesis of perovskite doped only in B

Doping in B	LFNO b1		LFCO b2		LFCNO b3	
5% by weight of dopant	Quantity required	Quantity weighted	Quantity required	Quantity weighted	Quantity required	Quantity weighted
La_2O_3	3,22 g	3,20 g	2,84 g	2,83 g	2,84 g	2,84 g
$Fe(NO_3)_3$	8,54 g	8,53 g	8,54 g	8,55 g	8,54 g	8,57 g
$C_6H_8O_7$	13,08 g	13,09 g	13,08 g	13,08 g	13,08 g	13,17 g
$Ni(NO_3)_2$	0,41 g	0,41 g	-	-	0,21 g	0,21 g
$Cu(NO_3)_2$	-	-	0,43 g	0,43 g	0,21g	0,22 g

Table 6: quantities of precursors for the sol-gel synthesis of perovskite doped in both A and B

Doping in A and in B	LBFNO c1		LBFCO c2		LBFNCO c3	
5% by weight of dopant	Quantity required	Quantity weighted	Quantity required	Quantity weighted	Quantity required	Quantity weighted
La_2O_3	2,84 g	2,85 g	2,84 g	2,82 g	2,83 g	2,84 g
$Fe(NO_3)_3$	8,54 g	8,55 g	8,54 g	8,55 g	8,54 g	8,59 g
BaO	0,70 g	0,71 g	0,70 g	0,71 g	0,70 g	0,72g
$C_6H_8O_7$	13,08 g	13,09 g	13,08 g	13,08 g	13,08 g	13,10g
$Ni(NO_3)_2$	0,42 g	0,42 g	-	-	0,21 g	0,20 g
$Cu(NO_3)_2$	-	-	0,43 g	0,37 g	0,21 g	0,22 g

1.2 Introduction of the catalyst by template impregnation method

A stoichiometric quantity of precursors, the nitrate salts of dopants, are dissolved in about 80ml of distilled water and the supporting perovskite powder is added. Successively, citric acid monohydrate is added. Using a plate with magnetic stirrer, the solution is continuously mixed and brought to 120°C. After about 12 hours, part of the solution evaporated allowing to obtain a gel. We then proceeded with the dehydration process, increasing the temperature to 300°C until a powder is obtained. Finally, after breaking in the mortar, calcination is carried out again, following a ramp of 5°C/min from room temperature to 400°C, which is maintained for 4 hours. In this case the temperature can be lower because the perovskite crystalline structure is already formed.

Table 7 shows in detail the quantities in grams of the precursors: Oxides of lanthanum and barium, nitrates of iron, copper and nickel, citric acid.

Table 7: Quanities of precursors for the deposition of catalysts by wet impregnation

	Ni in LFO1		**Cu in LFO2**		**Ni+Cu in LFO3**	
5% by weight of dopant	Quantity required	Quantity weighted	Quantity required	Quantity weighted	Quantity required	Quantity weighted
$C_6H_8O_7$	0,33 g	0,34 g	0,38 g	0,38 g	0,36 g	0,36 g
$Ni(NO_3)_2$	0,52 g	0,52 g			0,26 g	0,26 g
$Cu(NO_3)_2$			0,31 g	0,31 g	0,15 g	0,16 g
$LaFeO_3$	2,00 g	2,01 g	2,00 g	2,00 g	2,00 g	2,00 g

1.3 Exsolution

Exsolution of B-site metal can result in metallic nanoparticles uniformly embedding on the surface when perovskite oxides under reduction condition, which can return to the bulk lattice under oxidation condition. The exsolution catalyst of uniformly dispersed noble metal nanoparticles in perovskites was demonstrated to avoid problems of traditional poisoning and sintering during reaction. It is reasonable to optimize the exsolution process and catalyst stability via doping suitable amount of active metal ions at B site of $LaFeO_3$.

Functional materials consisting of metallic particles dispersed on the surface of oxides have been fundamental in enabling various catalytic and energy conversion applications. For the last decades, such materials have been generally prepared by deposition methods, whereby catalyst precursors are deposited over the surface of the oxide support, followed by various thermal decomposition or reduction processes to form the metallic nanoparticles.

An alternative preparation route has emerged in the last years, in which the catalyst in its ionic form is substituted into the crystal lattice of an oxide support under oxidizing conditions and subsequently released as metallic nanoparticles at the surface upon reduction at temperature (Figure 13). This process has been referred to as solid-state recrystallization or intelligent self-regeneration when carried out in a reversible manner and as redox exsolution when particle release at the surface is irreversible (17).

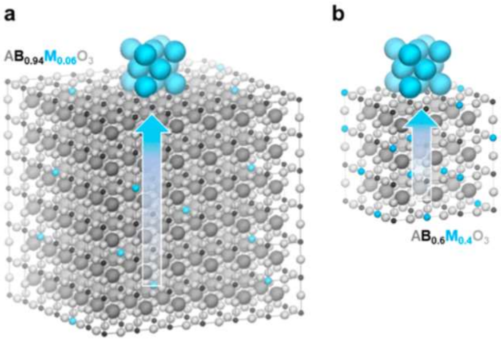

Figura 13: Exsolution from perovskites with different substitution level. Illustration of the number of perovskite unit cells required to form one metal unit cell (14 metal atoms) from perovskites $A_{1-\alpha}B_{1-x}M_xO_3$ *with substitution of M: (a) x = 0.06 (6 × 6 × 6 cells)*

Compared to particles prepared by deposition methods, which usually form relatively shallow interfaces with the oxide support, exsolved particles are not only more uniformly dispersed but also partially immersed (or socketed) into the surface of the host oxide support (Figure 14). In turn, this makes them considerably better anchored and more resistant to degradation by agglomeration or carbon deposition while also generating strain, which provides opportunities for accessing higher catalytic activity. Therefore, exsolution has emerged as an exciting platform for the design of advanced nanostructures, unlocking additional levels of reactivity and stability for various applications including fuel cells, H_2O, CO_2, and/or CH_4 (co)electrolysis, chemical looping H_2 production, membrane reactors, and catalysis of CO and NO oxidation, CO_2 reduction, photocatalysis, and hydrocarbon reforming.

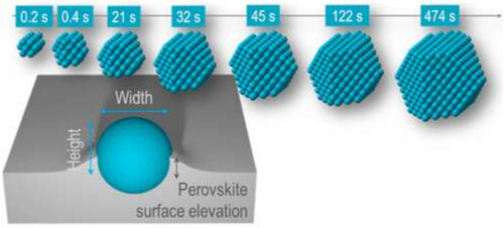

Figure 14: Exsolution perovskites

2. Characterization techniques

Throughout the laboratory phase, several analytical techniques have been performed on the samples to test for their purity and their morphology, as well as to assess the optimal operational temperature.

Catalytic reduction test have also been performed to assess for overall performance.

The techniques which have been used are the following:

- X ray diffraction (XRD)
- Temperature Programmed Reduction (TPR)
- Scanning Electron Microscopy (SEM)
- Energy Dispersed X ray spectroscopy (EDX or EDS)
- X ray Photoelectron Spectroscopy (XPS)
- Catalytic tests

2.1 X ray diffraction (XRD)

X-ray diffraction is a non-destructive analytical technique aimed at identifying the crystalline phase present in powders and solid samples. This technique also allows structural-crystallographic analysis (shape, size and characteristics of the unit cell), as well as microstructural analysis of the crystalline phases present in the material under examination.

XRD analysis is performed by the use of X-rays, i.e. high-energy electromagnetic radiation characterized by a wavelength comparable to the interatomic distance.

Due to their low absorption coefficient, X-rays pentrate deeply into matter and generate diffraction phenomena, which allow to obtain information on atomic positions and their nature.

Diffraction occurs when a wave passes through slits with dimensions comparable to its wavelength.

Slits act as sources of spherical radiation: the incidence of waves through slits causes interference phenomena through changes in the direction of propagation of the wave, caused by incidence on slits.

A crystal is a periodic system whose atoms are equidistant and parallel. X radiations interacting with a crystal interact with a huge number of slits, which constitute a diffraction grating, inside which each atom becomes a secondary source of a radiation.

When an X radiation hits an atom, the innermost electrons get excited and begin to oscillate, thus producing a spherical wave, whose intensity proportional to the number of its electrons.

The XRD technique is based on Bragg reflection or diffraction, whose law correlates the wavelength of the radiation to the interplanar distance by means of the diffraction angle: a collimated monochromatic X-ray beam is reflected by the adjacent and equivalent crystalline planes, generating a diffraction pattern.

Each plane of atoms only reflects a small part of the incident radiation: diffraction peaks are observed when rays from adjacent planes add up constructively.

Considering two adjacent lattice planes (Fig. 15), equivalent and at least partially reflective, separated by a distance d, two monochromatic X-rays with wavelength λ, incident under an angle θ with respect to these planes, interfere constructively if the difference in optical path between the reflected rays equals an integer number of wavelengths (18):

$$n\lambda = 2d_{hkl}sen\theta \qquad \text{Bragg's law}$$

where d_{hkl} is the interplanar distance between the lattice planes defined by the Miller indices hkl, λ corresponds to the wavelength of the incident ray, θ is the angle of reflection, equal to the angle of incidence, while n is a positive integer.

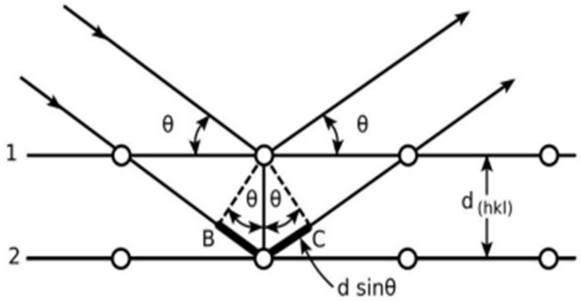

Figure 15: Bragg's Law (wikiToLearn, 2020) (19)

In order to evaluate a sample, it must be reduced to a crystalline powder, composed of fine particles randomly oriented in order to obtain a statistical distribution of the orientation of the families of lattice planes.

The final result consists of a diffraction spectrum, consisting of a series of peaks with different intensities and angular positions relating to the various phases present in the sample investigated. By plotting the intensities of the diffraction peaks as a function of the angular position of the detector 2θ, the *characteristic pattern* of the examined sample is obtained (Fig. 16-17).

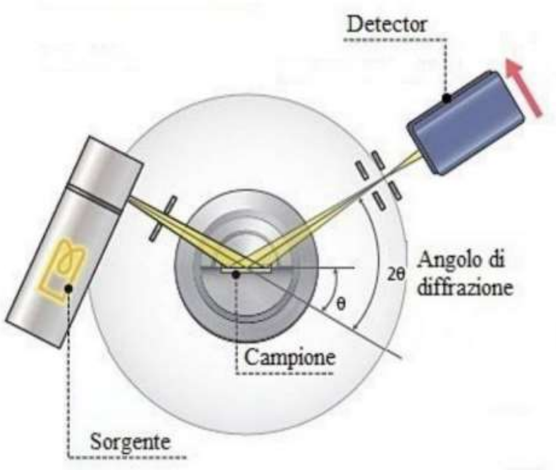

Figure 16: Operation diagram of a diffractometer for XRD (Samis et al., 2017)

Figure 17: Photo of a difractometer for XRD

Typically X-ray diffractometers are based on the Bragg-Brentane scheme (20), in which the X-ray source is kept fixed while the sample and detector rotate at the same angular speed, while the sample is in a horizontal position, rotating on itself at a chosen speed. The radiation incident on the sample is given by a parallel and monochromatic X-ray beam, with a well defined wavelength. The diffracted radiations are collected by a detector, which translates them into electrical impulses: such electrical impulses are then amplified and sent to a computer for data processing.

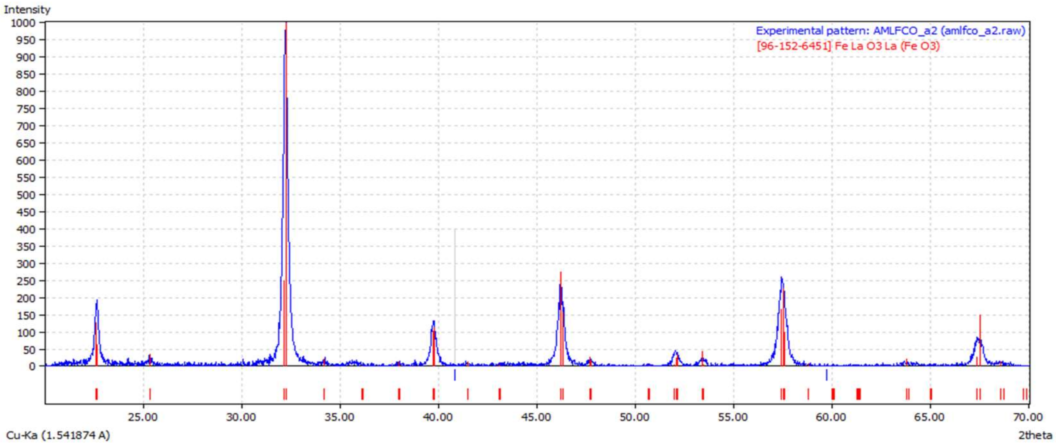

Figure 18: Example of XRD spectrum of a lanthanum ferrite perovskite

An image called "diffraction pattern" is obtained from an X-ray diffraction experiment and is characteristic for each type of material (Fig. 18). The pieces of information that can be obtained directly are:

- angular position: structure and phases
- intensity of the peaks: structure and relative abundance of the phases
- peak profile: crystallinity, disorder, stress state and grain size

2.2 Temperature programmed reduction (TPR)

It is now appropriate to study the behavior of La-perovskite and of materials derived from it in a reducing enviroment, following their usa as redox/oxygen storage components in the supply of catalysts. As a requisites for such usa, the lanthanum ferrite must be able to absorb and release oxygen following changes in the stoichiometric composition of the feed stream. In doing so the catalyst is continuously subjected to reduction and oxidation involving alternating creation and removal of oxygen vacancies.

The temperature programmed reduction (TPR) simply analyzes the reduction profile as a function of temperature. (21)

TPR is a very useful technique in the characterization of metal oxide-based catalysts, because it allows to obtain important information on the oxidation state of the reducible species present in the catalyst. In particular, TPR is used when one wants to determine:

- The number and quantity of reducible species present in the analyzed sample
- The reduction temperature of the reducible species
- The type and number of active sites present on the catalytic surface
- Different kinetic and thermodynamic parameters
- Qualitative measurements of the chemical-physical properties of the analyzed compound.

The reaction on which the technique is based is the following:

$$MeO + H_2 \rightarrow Me + H_2O$$

From a TPR graph (thermogram), it is possible to obtain qualitative information: on the basis of the number of TPR peaks obtained, it is possible to determine not only the number of reducible species present but also their oxidation state and the reduction temperature. Furthermore, quantitative information is also obtained since it is possible to determine the amount of reduced sample, calculating the amount of H2 consumed by the integration of the area of the TPR peak.

The instrument (Fig. 19-20) consists of two different and independent circuits:

- Sample pre-treatment circuit: before being analysed, the sample is treated with a current of inert gas, to remove any absorbed water or any contaminants present from its surface;
- Analysis circuit: the sample is analyzed by sending a gas mixture (H_2 in Ar at 5%) to the surface.

The sample is introduced into a packed fixed bed reactor placed in an electric furnace. The gas first passes into the boiler, where it is heated to the desired temperature, passes through the catalyst bed in the reactor and interacts with the sample present. Using a bath, the water is condensed, and the products are sent to a detector where their concentration are monitored.

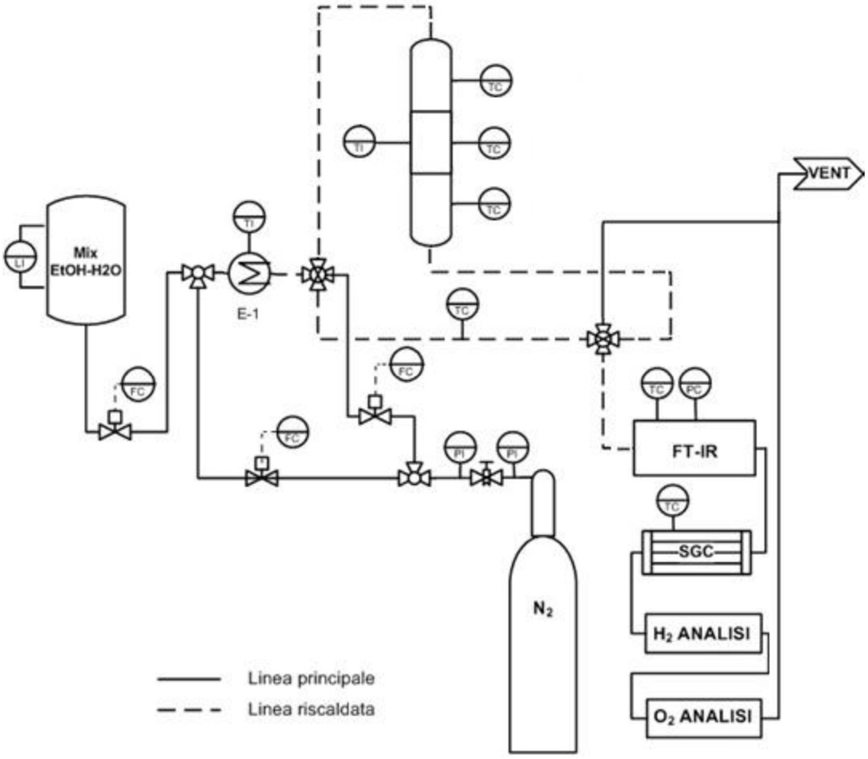

Figure 19: Schematic of the TPR instrumentation

Figure 20: TPR tool used in laboratory

2.3 Scanning Electron Microscopy (SEM)

Electron microscopy has been a revolutionary imaging technology over the past 80 years, opening up the world of nanomaterial and allowing for the characterization of their unique properties: the ability of electron microscopes to image submicron-sized objects, down to single atomic position, has led to the development of entirely new nanotechnologies while enabling remarkable advances through nanoscale engineering of macro-sized components.

The most common microscopes in the world today are light microscopes. However, most of them cannot distinguish objects and features smaller then about 0,1mm (100nm) (23, 24) (Fig. 21).

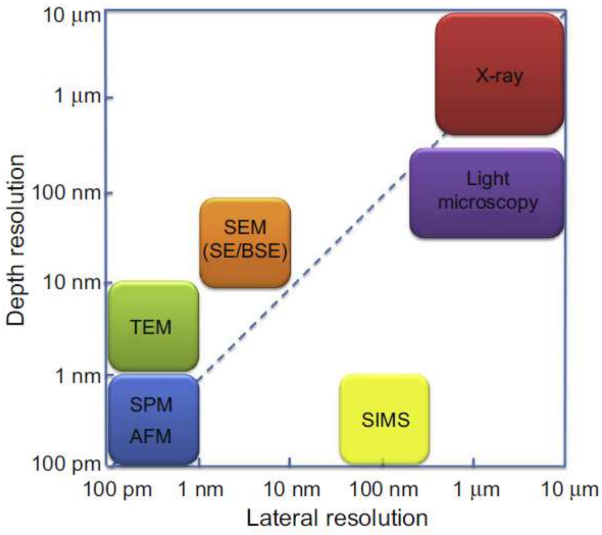

Figure 21: Comparison of typical spatial resolution of leading imaging methods for material characterization SPM, AFM, TEM, SEM, SIMS, X-ray imaging, and optical microscopy.

The resolution of a microscope is the ability to separate two elements at a given distance as individual objects in the image.

The shorter wavelengths interact more strongly with nanoscale materials and can produce higher resolution images (25). Looking across the electromagnetic spectrum, radiations with wavelengths shorter than visible light include ultraviolet (100-400 nm) and X-rays (10 pm and 10 nm).

Particles can also behave like waves: this phenomenon is known as wave-particle duality. The wavelengths of electrons depend on their momentum, which can be increased by accelerating them across a range of voltages. Higher accelerating voltages produce higher energy electrons with smaller wavelengths. A microscope designed to use 200 and 300 keV can potentially offer an image spatial resolution, down to less than 0.1 nm (100 pm) (26).

This atomic-level resolution is comparable to non-destructive surface imaging techniques such as scanning probe microscopy (SPM) and atomic force microscopy (AFM) (Fig. 21).

There are two generic classes of electron microscopy, SEM and TEM, depending on the type of microscope used: both technologies generate highly focused electron beams, which strike the sample inside a vacuum chamber. However, SEM microscopes are primarily designed to examine the surfaces of materials, while TEM microscopes are primarily designed to examine the internal structure of samples.

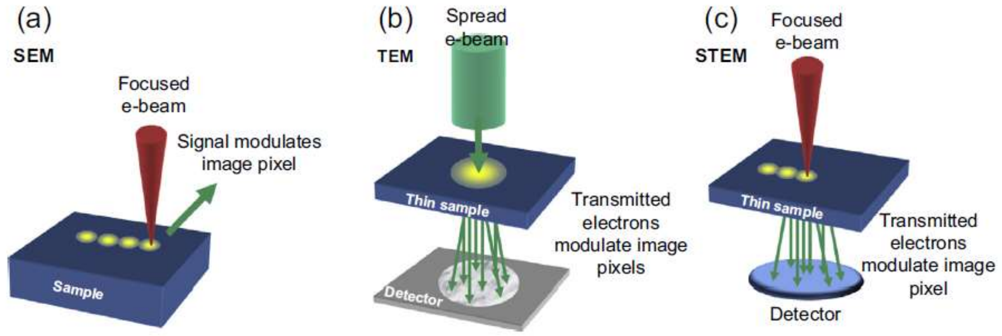

Figure 22: Outline of SEM, TEM and STEM imaging methodology. (a) Serial collection of data points in SEM. (b) Acquisition of parallel images in TEM. (c) Serial collection of transmitted electrons in STEM.

To this end, the two tools work differently:

- In the SEM the electron beam is focused on a point and is scanned sequentially through the sample (Fig. 22(a)) (27). At each location, signals are emitted from the sample and picked up by detectors. The detector signal is synchronized with the known position of the beam on the sample and the intensity of the signal is used to modulate the corresponding image pixel. The collected signals are combined to form an image whose size/pixel distribution depends on the scan pattern chosen.

- In the TEM the electron beam impinges on a defined area of the sample (Fig. 22(b)). Electrons transmitted through the sample are focused by lenses and collected by a parallel detector to form an image.

Hybrid versions of SEM and TEM are also possible in modern machines. SEM microscopes can be equipped with detectors to collect electrons transmitted through thin samples (Fig. 22(c)). This scanning mode methodology with transmitted signal collection is usually called scanning transmission electron microscopy (STEM) (28). Modern TEMs equipped with extra scanning instrumentation can also scan a highly focused beam, allowing for the deployment of STEMs at higher electron energies (29).

There are a range of mechanisms by which electrons interact with matter, which are exploited in electron microscopy to generate a range of signals which are collected and used to form an image of the sample.

We distinguish the primary electrons that hit the sample, from the secondary electrons (SE) that come from inside the sample:

The primary electrons incident on the sample each follow an individual trajectory through the sample. Primary electron interactions with atoms and electrons cause scattering, resulting in a change in direction of electrons from their original path (30).

The spectrum of exemplary electron interactions can be divided into elastic interactions and inelastic interactions.

- Elastic scattering occurs when there is no loss of energy from the incident primary electron. Elastically scattered electrons can change direction but not change their wavelength.
- Inelastic scattering occurs when there is an interaction that causes the incident primary electron to lose energy.

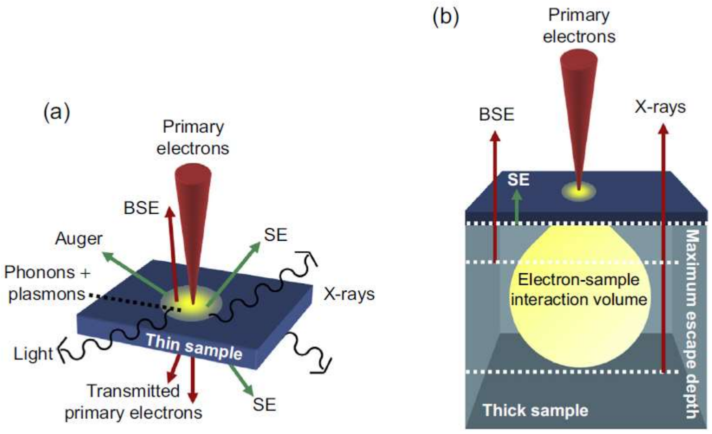

Figure 23: The interaction of incoming primary electrons with a sample. (a) Useful signals generated by electromatter interactions in a thin sample. (b) Absorption of SE, BSE and X-rays in thick samples, by inelastic dispersion within the interaction volume, limits the depth of the sample from which they can escape.

When an electron beam strikes a sample, key signals emitted by the sample are scattered primary electrons, SE and X-rays (Fig. 23) (31). These signals are abundant, easy to collect, and form the basis of most microstructural characterization studies using SEM.

The primary electrons, which are scattered and emerge from the sample surface are called backscattered electrons (BSE).

Instead, the SEs are generated by different inelastic scattering mechanisms. The most common SEs are slow SEs, which are ejected from the outer shell or loosely bound valence electrons with very low energies between 0 and 50 eV. Fast SEs are knocked out of inner atomic shells and can have up to 50% of the incident primary energy. Low-energy Auger electrons with specific energies also occur from electron transitions between energy levels.

X-rays are generated by two main mechanisms of inelastic diffusion (32). Bremstrahlung X-rays are caused by the slowing down of primary electrons as they pass through atoms and have a continuous range of energies up to the incident energy of the primary electron. Characteristic X-rays are produced when primary electrons knock an electron out of an atom and the subsequent transition of a second electron between energy states results in the generation of an X-ray of specific energy (the difference in energy levels) (Fig. 24).

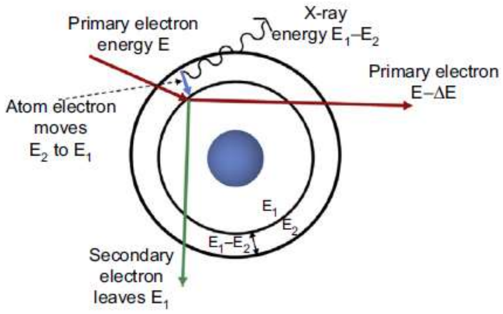

Figure 24: Electron-induced X-ray emission. Characteristic generation of X-rays. An X-ray is generated when an electron moves to fill the energy level of the empty electron vacated by the secondary electron.

Scanning electron microscopy is the technique of choice for the analysis of sample surfaces. Fig. 25-26 shows the typical layout of an SEM, which includes the electron gun (electron source and accelerating anode), electromagnetic lenses to focus the electrons, a vacuum chamber housing the sample stage, and a selection of detectors to collect the signals emitted by the sample.

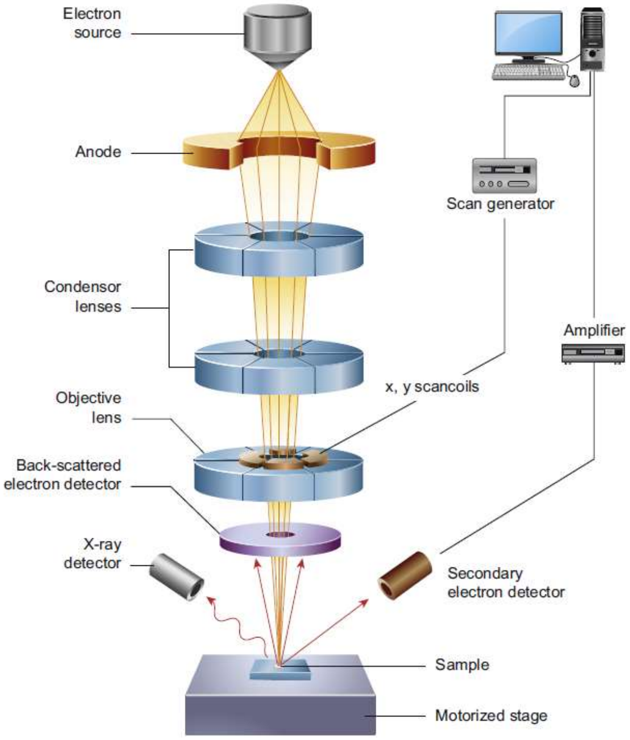

Figure 25: Schematic diagram of the main components of a SEM microscope.

Figure 26: Photo of the SEM instrument used in the laboratory.

2.4 X ray energy dispersion (EDX)

EDX (Energy Dispersive Spectroscopy) is considered a useful tool for elemental composition estimation and X-ray mapping. Each atom is characterized by its electron configuration. When bombarding a sample with high-energy electrons (X-rays), the electrons that are ejected produce an electron vacancy in their inner shell: as a result, high energy electrons are transferred to lower energy level (Fig. 27). The collateral phenomenon linked to the transfer of electrons is the production of X-rays. By measuring the characteristic energy and intensity of X-rays, it is possible to determine the elemental composition of the sample.

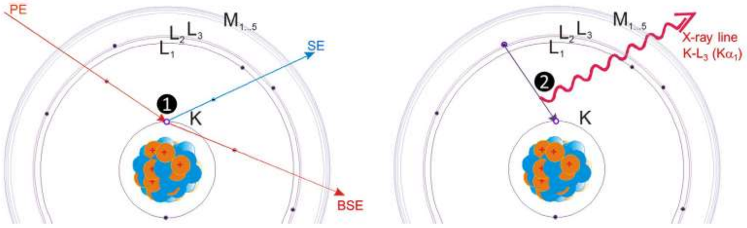

Figure 27: Illustration of the two-step process of emitting characteristic X-rays by electron excitation: (1) A primary electron (PE) with energies in the keV range collides with a sample atom and knocks out a secondary electron (SE) from a shell , creating a vacation spot; PE loses energy and can leave the sample. (2) The excited ion relaxes to the equilibrium state after.

EDX Quantitative Assay can be successfully applied on bulk samples, as long as the volume analyzed has a homogeneous elemental composition, the surface of the sample is flat and the energy of X-ray lines analyzed are greater than 1keV (33).

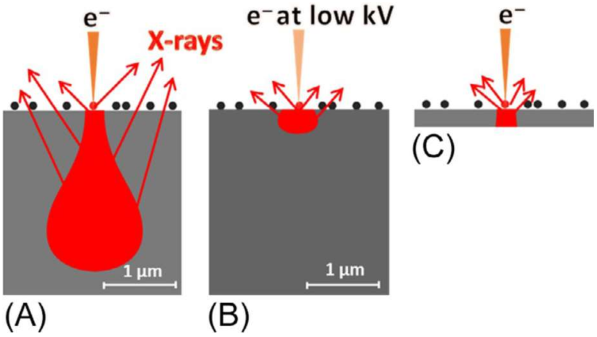

Figure 28: From conventional SEM/EDS analysis of nanoparticles on bulk substrates (A) to submicrometer EDS analysis operating at low accelerating voltages (B) and beyond EDS analysis well below 100 nm by tailoring sample preparation of nanoparticles on a transparent support for electrons (C).

The volume of sample information addressed by EDX analysis can be significantly reduced from the micrometer range for conventional bulk samples to well below 100nm for electron transparent samples by considering only the excitation volume bottleneck (see Fig. 28). This variant results in superior X-ray spatial resolution even compared to operation at low beam voltages on a bulk substrate, when high-energy X-ray lines cannot be excited (34, 35- 36).

Two geometries are used in the analysis of the transmission mode with a SEM:

- The first geometry is based on the use of a semiconductor detector (STEM) placed under the electron-transparent

- The second geometry consists of a sample holder dedicated to the "transmission" which allows primary electrons to pass through the sample and arrive at a gold converter layer on which they are multiplied - in this configuration the detector collects only the transmitted electrons, while the secondary and backscattered electrons are blocked by a closing loop.

In order to successfully use EDX analysis of nanoparticles, the use of sensitive EDX detectors is decisive, even in the transmission operating mode. The low number of X-rays emitted by electron-transparent samples, resulting in low signal-to-noise ratios of the spectra, must be compensated for by long measurement times or large solid angles enclosed by the EDX detector. Therefore, the only solution to obtain EDX spectra from single nanoparticles with a good signal-to-noise ratio is to efficiently collect the emitted X-rays. Modern EDX spectrometers not only provide high signal rates, but are also available with large nominal detector crystal areas (Fig. 29).

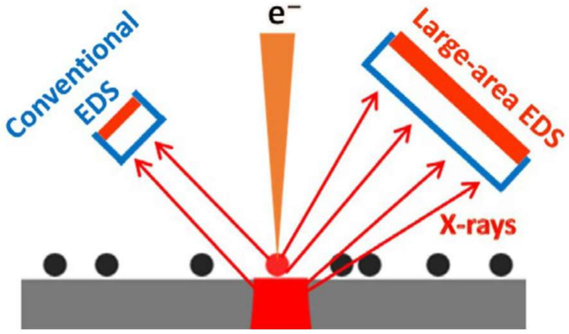

Figure 29: Diagram showing higher collection efficiency of a large EDS detector than a conventional EDS detector.

Analytical modeling of EDX spectra emitted from non-planar samples, such as nanoparticles deposited on a substrate, is not possible. However, Monte-Carlo simulations are a powerful tool to simulate EDX spectra corresponding to complex sample geometries including various shapes of nanoparticles (37)

Monte-Carlo programs are based on the consideration of elastic and inelastic collisions of single electrons within the sample, allowing the simulation of radiation transport, thus the numerical prediction of the number of X-ray quanta emitted with defined interaction probabilities.

Fig. 30 shows the result of the Monte-Carlo simulations of the EDS spectra performed for a single spherical SiO2 particle located on a bulk titanium substrate.

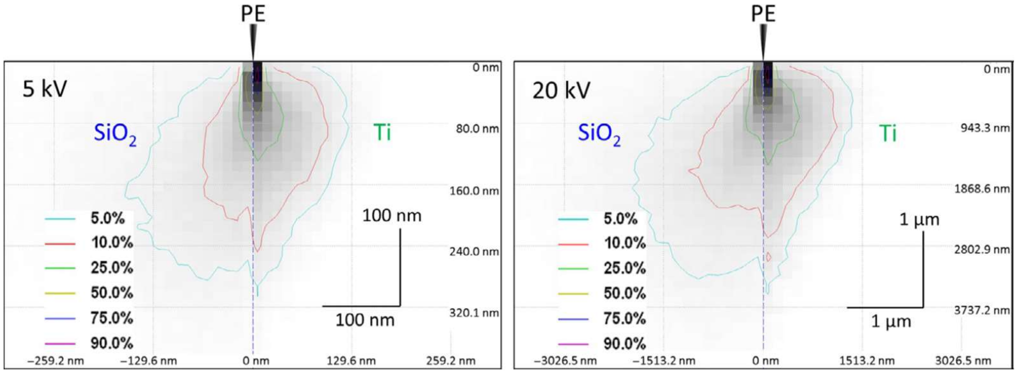

Figure 30: Visualization of interaction volume between primary electrons (PE) and sample atoms resulting in X-ray generation using Monte-Carlo simulation at 5 kV (left) and 20 kV (right) electron beam voltage for a sample defined as composed of SiO2 (left half) and titanium (right half) (36).

2.5 X ray photoelectron spectroscopy (XPS)

X-ray photoelectron spectroscopy is a surface-sensitive analytical technique in which X-ray are used to bombard the surface of material, which in turn emits electrons whose kinetic energy is measured. The two main characteristics of this technique, which make it powerful as powerful analytical method, are its surface sensitivity and its ability to reveal information about the chemical state of the elements in the sample.

XPS is based on the photoelectric effect, first discovered by Heinrich Hertz who noticed that electrons were emitted from surface when irradiate with light (38).

To understand why XPS is a surface-sensitive technique, it is necessary to examine the physical processes that affect electrons traveling in solids. The X-ray irradiating the sample can penetrate quite deep (a few µm) into the sample. Electrons generated this deep in the sample will experience many inelastic collisions, resulting in energy loss, and will eventually lose all of their energy before leaking out of the sample, these electrons are denote by the letter C in figure 31:

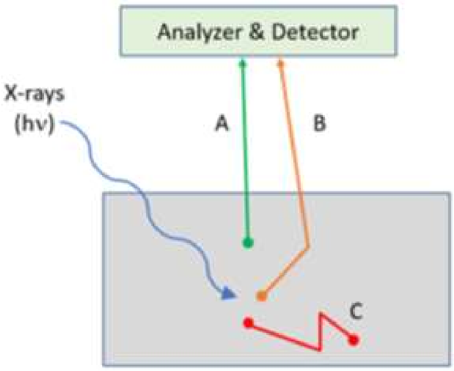

Figure 31: The emitted electrons interact with the sample in different ways depending on the depth at which they are generated. The electrons emitted without interaction, labeled A, produce XPS and Auger photoelectron peaks. Electrons that undergo at least one inelastic collision, labeled B, contribute to the background. Electrons that undergo multiple collisions and do not escape the sample are labeled C (39)

Electrons generated close to the surface may have only one or two inelastic collisions before escaping the sample and reaching the detector. These electrons leave the sample with less kinetic energy than expected because they lost a random amount of energy on their way to the4 detector. In Figure 31, these electrons are labeled B; their contribution to the vertical step in the background signal that accompanies any large photoelectron or Auger electron peak, as shown in figure 32.

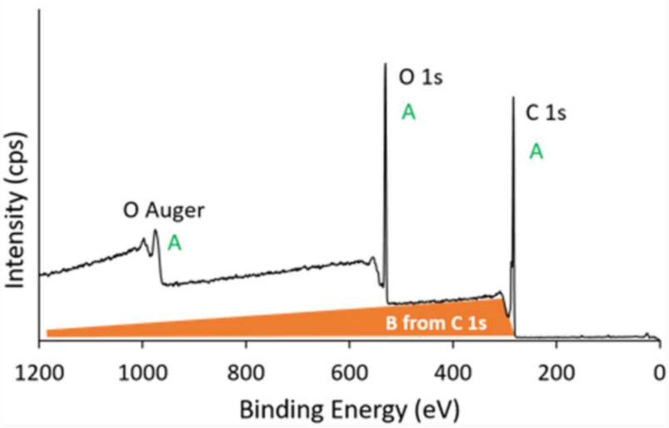

Figure 32: XPS spectrum with labeled photoelectrons and Auger peaks. The orange shaded area shows the contribution to the background signal that comes from the C 1s electrons. Similar background contributions are also made by the electrons of the O 1s and O Auger transitions, forming the vertical "steps" in the baseline observed for each major peak (39).

The background contribution from the C 1s peaks is shaded orange, and similar background contributions are provided by the O 1s and O Auger peaks. Only electrons that escape the surface without inelastic collisions will contribute to the characteristic photoelectron spikes we use in the XPS analysis. These are labeled A in figures 31 and 32.

The surface sensitivity of XPS is determined by how deep an electron can be generated and still escape without inelastic scattering. Beer's law describes the intensity, I, of the electrons emitted by a sample at depths greater than d, where I0 represents the total number of electrons generated by the sample:

$$I = I_0 \exp\left(-\frac{d}{\lambda}\right)$$

The λ term is the electron attenuation length, which will depend on the energy of the electron and the material through which it is traveling. The attenuation length is similar to the inelastic mean free path (IMFP) of the electrons, which is defined as the average distance that an electron with a certain kinetic energy can travel before inelastic scattering, but the attenuation length also takes into account the effect of elastic scattering (40). Using Beer's law, it can be shown that approximately 95% of the electrons escape from a depth of 10nm or less, and 10nm is often cited as the information depth for XPS. Informative depth, commonly called sampling depth, is defined as the maximum depth normal to the surface from which useful information is obtained. (41) And in this case 95% of the total signal is obtained useful information.

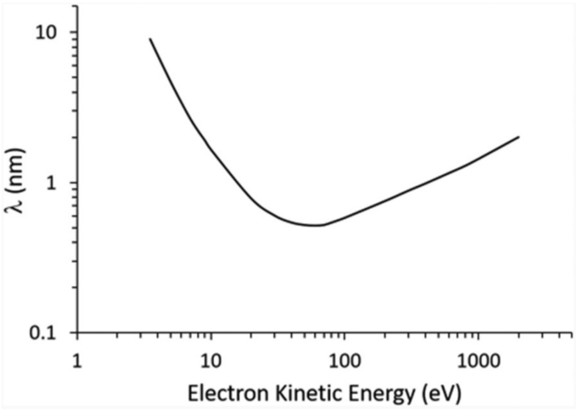

Figure 33: The inelastic mean free path (IMFP or λ) is shown as a function of the kinetic energy of the electron.

For electrons typically analyzed with XPS (E_k>100eV), the IMFP increases as the kinetic energy of the electron increases, are shown in Figure 33. High-energy X-ray sources generate electrons with higher kinetic energies:

$$BE = hv - KE - \Phi_{spec}$$

therefore, electrons will be able to escape from the deepest area of the sample.

An XPS instrument contains an x-ray source, sample stage, extraction lenses, analyzer, and detector housed in a very high vacuum environment. A schematic diagram of an XPS system is shown in Fig. 34, illustrating all the major components, described in detail in references 42-43:

XPS instruments are housed in an ultra-high vacuum (UHV) environment for two reasons. First, emitted electrons must not scatter air molecules on their way to the analyzer. As XPS is a surface sensitive technique, it is very sensitive to surface contamination. For this reason, XPS instruments utilize the UHV environment to reduce surface contamination that occurs within the chamber.

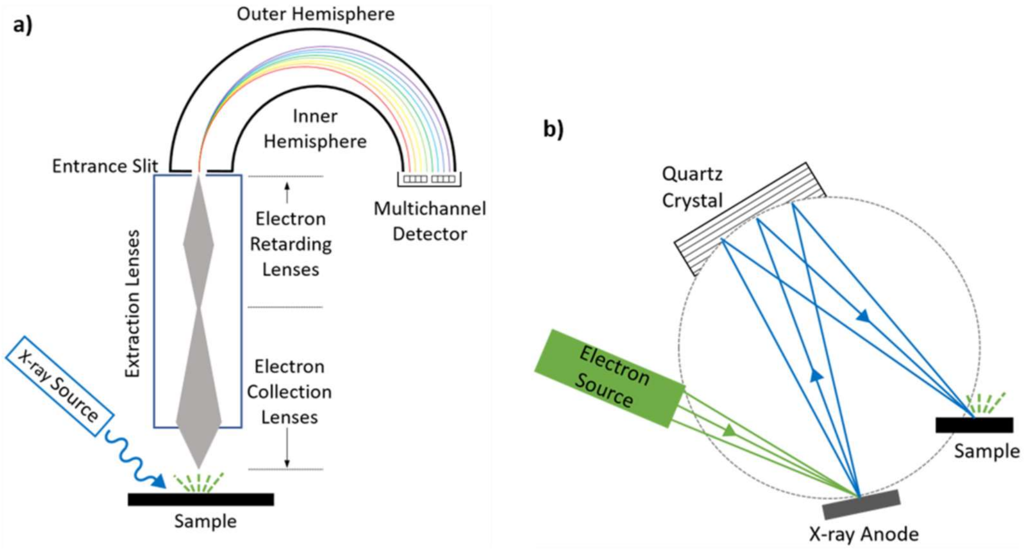

Figure 34: The schematic diagrams show the main components of an (a) XPS and (b) monochromator instrument.

2.6 Catalytic tests

The measurements of the catalytic activity were carried out using a reactor subjected to flows of three different gases (hydrogen, carbon dioxide and argon), with a progressive increase in temperature; using in a system (Fig. 35) consisting of:

- 3 gas injection lines, respectively flowmeter 1 was used to regulate the transport of CO2 from the cylinder to the reactor, flowmeter 2 was used for the transport of H2 (in cylinder with 10% dilution in helium) and the flowmeter 3 for the transport of the Ar.
- A thermocouple heating furnace
- A tubular quartz reactor with an internal diameter of 8mm, in which the catalytic bed will be placed
- A gas chromatograph (Agilent 7820) for analysis of reaction products

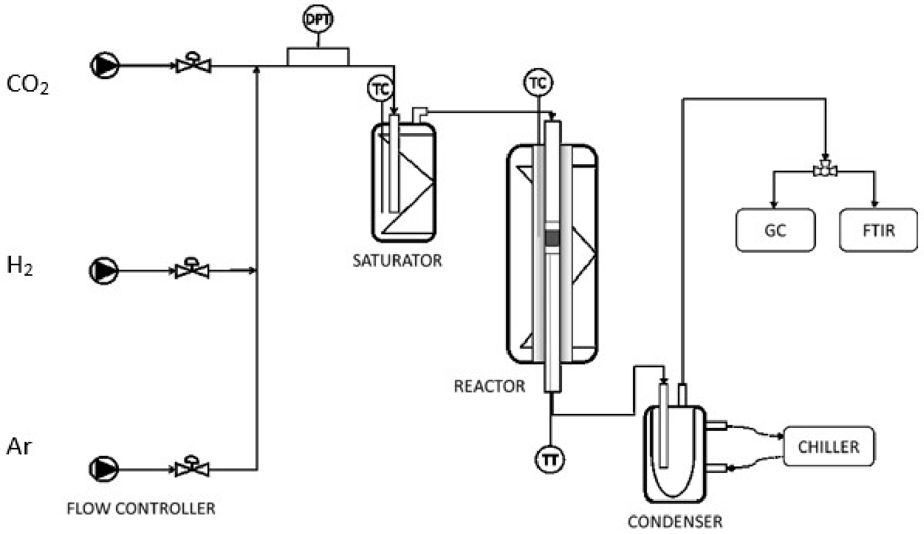

Figure 35: Catalytic setup for testing.

The electrically heated quartz reactor contains a shallow bed of catalyst powder (50mg of sample). The temperature is monitored upstream of the bed; was varied between 200°C and 500°C. The vapor in the offgas was then condensed and the dry mixture was analysed. The following gases were determined: CO2, CO and CH4 by gas chromatograph. The set up is summarized in the diagram in figure 1.
The standard test sequence in these measurements is:

- Heating of the catalyst from room temperature to 600°C in an atmosphere of diluted hydrogen Argon
- 2 hours of exolution at 600°C in diluted hydrogen

- Fast cooling (about 10°C/min) up to 150°C
- Fast heating (about 10°C/min) up to 200°C followed by a 30-minute hold in a reaction atmosphere (80% H2, 10% CO2 and 10% Ar)
- Slow temperature increase (about 2°C/min) to measure the catalyst activity at different temperatures, up to a maximum of 500°C

It has been verified that the selected heating rate of 2°/min is slow enough to obtain stationary operation of the catalyst, at each scanned temperature. Since the test is basically conducted on small isothermal plateaus, the exothermicity of the reactions involved (such as CO, H2 oxidations) does not represent a major problem for the accuracy of the test.

This instrumental configuration was chosen for the catalytic tests due to the ease and speed with which it is possible to obtain the required data. Furthermore, a particularly interesting feature of this technique is that most of the physicochemical properties of the solid catalyst can be studied under the operating conditions of the catalyst (in some cases during the catalysis); and also allows for the simultaneous determination of physicochemical properties and catalyst activity, which is useful in the direct correlation of these parameters to explain the exact mechanism of a surface-catalyzed reaction and, ultimately, to understand the catalytic process.

III. Results and discussions

This Chapter presents the results obtained from the characterization of the materials and from the catalytic tests of the methanation process.

1. X ray diffraction (XRD)

X-ray diffraction analysis was performed on our sample set and diffractograms were acquired. The spectra have been reported in the graph in the figure (fig. 36), which shows the diffraction angle 2θ on the abscissas and the diffraction intensity in dimensionless units on the ordinates.

The analysis of the diffractometric results obtained was done in the Match! using a reference database. It was therefore possible to identify the characteristic peaks of the lanthanum ferrite, as well as the presence of impurities of barium carbonates recognizable thanks to the presence of low intensity peaks at low angles in the diffractograms of the LBFNCO_c3 and LBFNO_c1 samples (highlighted in red in Fig.36).

Extensive research within scientific literature was performed to infer the structure of perovskite samples: by comparing XRD results with those obtained by Wu et al. in 2021 (44) during XRD analysis of Cu-doped perovskite samples, it was possible to infer that the structure of the perovskite samples obtained is orthorhombic. In Figure 37-38, an example of such comparison is reported.

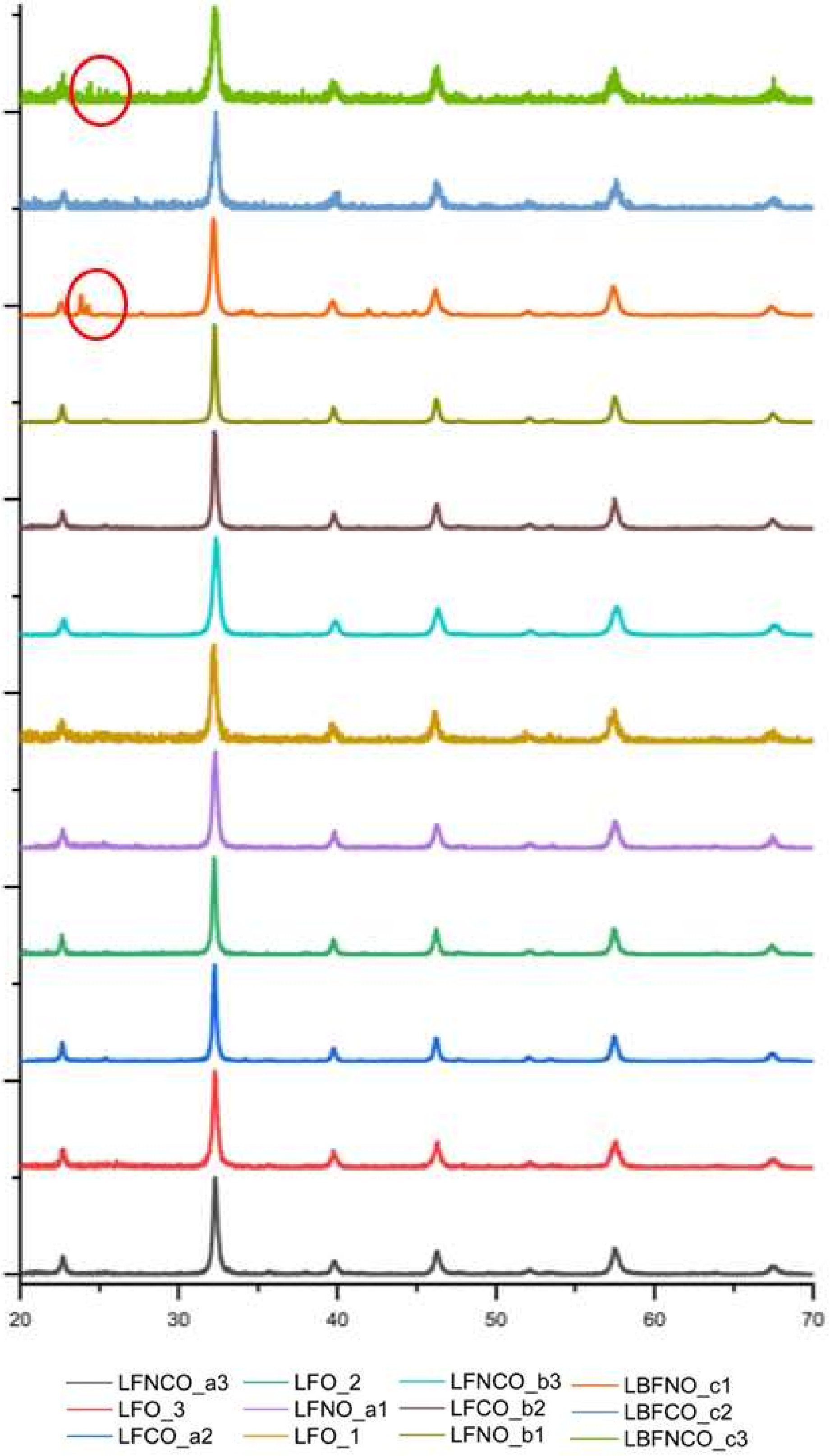

Figure 36: Diffractogram of the samples related to the X-ray diffraction analysis.

a = template impregnation, b = direct doping, c = direct doping + A site doping

N / 1= doping with Ni, C / 2= doping with Cu, NC / 3 = doping with Ni-Cu alloy

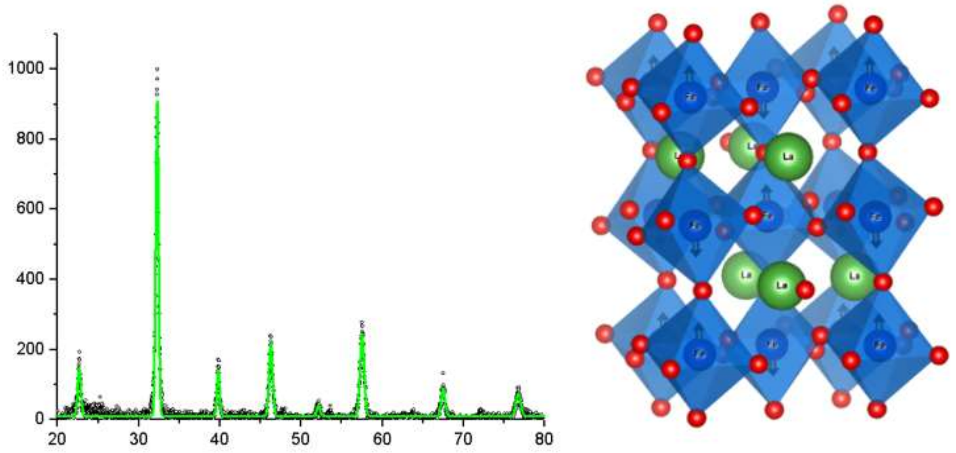

Figure 37: Spectrum of LFNO_a1, graphical representation of lanthanum ferrite with orthorhombic structure

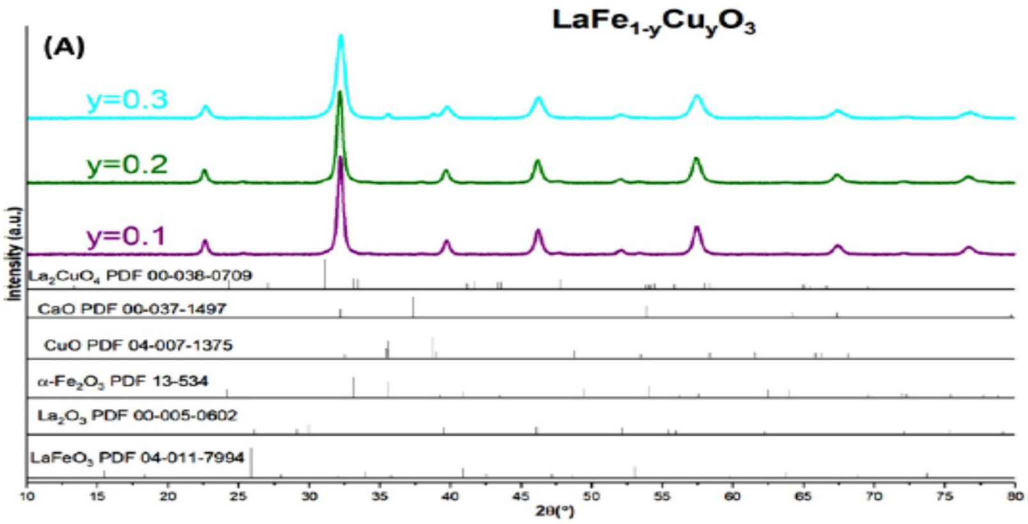

Figure 38: Reference spectrum from literature (44)

To qualitatively analyze the surface of the samples in a standardized way, the data extracted from the XRD were interpolated using bell-type functions: the width of the bells was evaluated as the width at half height Γ.

For simplicity and comparability with the scientific literature, the function chosen for the analysis was the Gaussian function (Figure 39), with the following formulations:

$$Intensity = peak \cdot \exp\left(-\frac{2\theta - \theta_{peak}}{2\sigma}\right)$$

$$\Gamma = 2\sqrt{2ln2}\sigma = 2{,}355\sigma$$

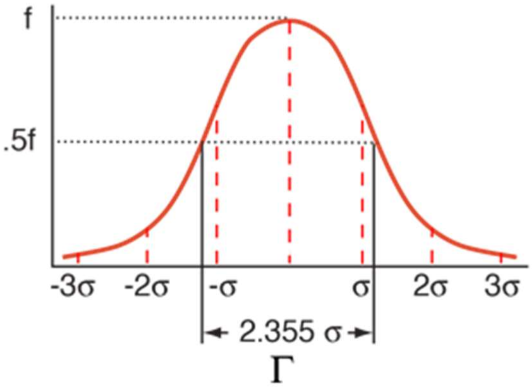

Figure 39: example of a bell curve

The calculated amplitude of the bell curves of the analyzed samples is shown in the table 8.

The reported data were used to estimate crystallite size using the Scherrer equation (Table 9), which expresses the inverse proportionality between peak width and active surface area:

$$d = \frac{0{,}94 \cdot \lambda}{\Gamma \cdot cos\theta}$$

where d is the crystallite diameter, λ is the X-ray wavelength (0.15418nm), Γ is the peak width (rad), and θ is the peak position.

Table 8: Width at half height of the peaks of the diffraction spectrum

Length	$2\theta=23$	$2\theta=32$	$2\theta=40$	$2\theta=46$	$2\theta=52$	$2\theta=57$	$2\theta=67$	$2\theta=70$	$2\theta=77$
LFO_1	0,70	0,76	0,78	0,82	1,00	1,13	1,17		1,45
LFO_2	0,46	0,54	0,59	0,66	1,14	0,80	0,94	0,73	1,05
LFO_3	0,64	0,71	0,78	0,89	0,75	1,05	1,02	0,51	1,13
LFNO_a1	0,76	0,70	0,69	0,84	0,73	1,01	0,88	0,01	1,15
LFCO_a2	0,45	0,53	0,58	0,65	0,55	0,79	0,86		
LFNCO_a3	0,59	0,67	0,72	0,81	0,79	0,97	0,97		
LFNO_b1	0,36	0,43	0,48	0,54	0,53	0,65	0,72	0,56	0,84
LFCO_b2	0,56	0,58	0,61	0,72	0,67	0,83	0,90	0,58	0,99
LFNCO_b3	0,58	0,72	0,72	0,85	0,70	0,99	1,07	0,70	1,23
LBFNO_c1	0,49	0,63	0,67	0,79	0,60	0,87	0,91	1,09	0,49
LBFCO_c2	0,62	0,69	0,76	0,79	0,85	0,99	0,95	0,98	0,62
LBFNCO_c3	0,88	0,78	0,94	0,89	0,37	1,12	1,11	1,12	0,88

Table 9: Crystallite size calculated using the Scherrer equation

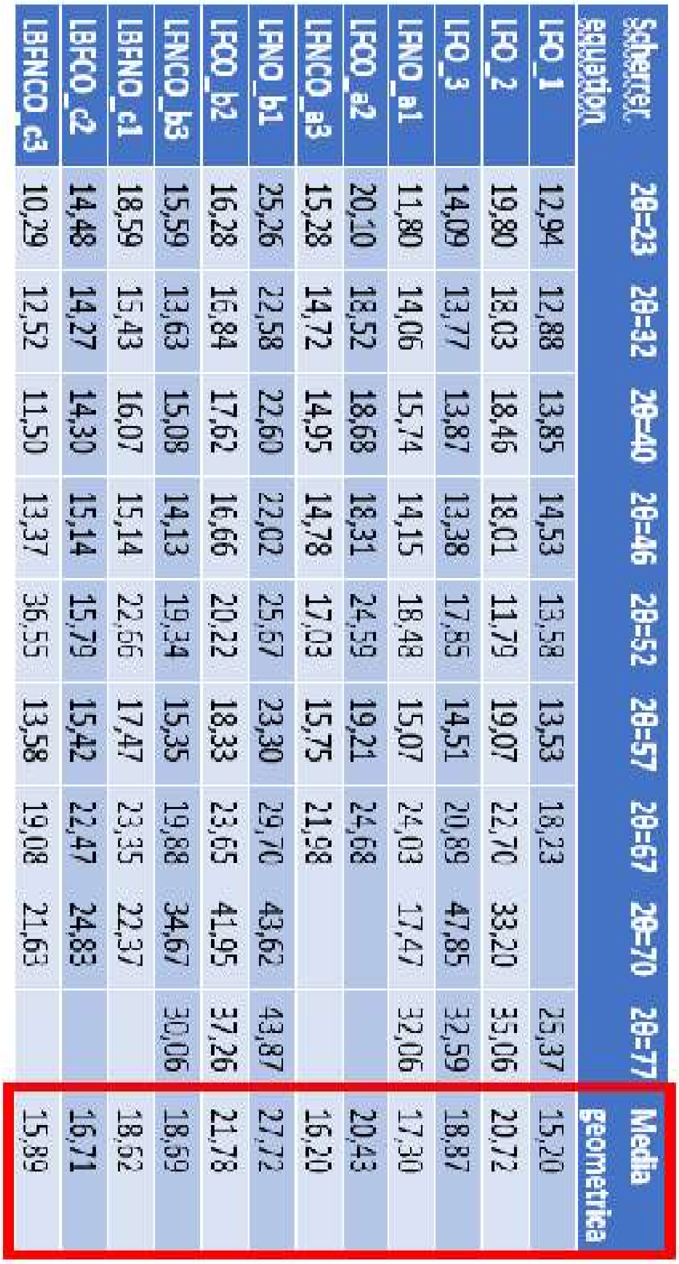

Scherrer equation	2θ=23	2θ=32	2θ=40	2θ=46	2θ=52	2θ=57	2θ=67	2θ=70	2θ=77	Media geometrica
LFO_1	12,94	12,88	13,85	14,53	13,58	13,53	18,23		25,37	15,20
LFO_2	19,80	18,03	18,46	18,01	11,79	19,07	22,70	33,20	35,06	20,72
LFO_3	14,09	13,77	13,87	13,38	17,85	14,51	20,89	47,85	32,59	18,87
LFNO_a1	11,80	14,06	15,74	14,15	18,48	15,07	24,03	17,47	32,06	17,30
LFCO_a2	20,10	18,52	18,68	18,31	24,59	19,21	24,68			20,43
LFNCO_a3	15,28	14,72	14,95	14,78	17,03	15,75	21,98			16,20
LFNO_b1	25,26	22,58	22,60	22,02	25,67	23,30	29,70	43,62	43,87	27,72
LFCO_b2	16,28	16,84	17,62	16,66	20,22	18,33	23,65	41,95	37,26	21,78
LFNCO_b3	15,59	13,63	15,08	14,13	19,34	15,35	19,88	34,67	30,06	18,69
LBFNO_c1	18,59	15,43	16,07	15,14	22,56	17,47	23,35	22,37		18,52
LBFCO_c2	14,48	14,27	14,30	15,14	15,79	15,42	22,47	24,83		16,71
LBFNCO_c3	10,29	12,52	11,50	13,37	36,55	13,58	19,08	21,63		15,89

The Scherrer equation showed that the different methods of deposition of the catalysts did not have an important impact on the size of the crystallites, which have an average size of about 19 nm.

After preliminary reduction of the samples, in an atmosphere of hydrogen diluted in argon, for 2 hours at 600°C, XRD analyses were carried out and the diffractograms were acquired, to evaluate the formation of metallic nanoparticles of the catalysts. The spectra of the LFNO_a1 and LFNO_b1 samples are shown in figure 40.

The metallic nickel peaks have been highlighted in yellow: for the LFNO_a1 sample its presence is evident, this cannot be said for the LFNO_b1 sample. The presence of Ni in the LFNO_b1 sample was confirmed by subsequent tests. The absence of XRD signals due to Ni in LFNO_b1 could be due to the lower amount (0,52g in LFNO_a1 and 0,42g in LFNO_b1).

Another possibility is the different procedure for the addition of Ni: template deposition in LFNO_a1 and exsolution from precursor perovskite in LFNO_b1. Both samples are 5% nickel doped, however the LFNO_a1 catalysts, being on the surface, should be less visible than in the LFNO_b1 sample given that in the second case they are found in the bulk of the material.

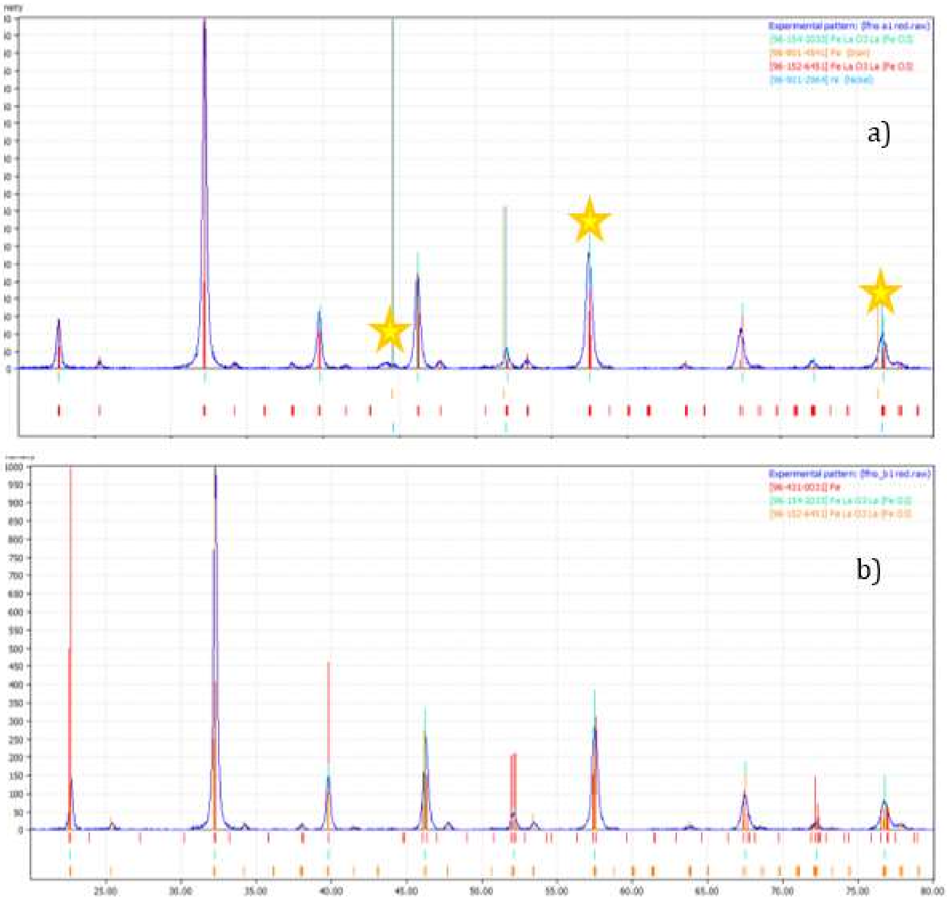

Figure 40: XRD spectrum of LFNO_a1 (a) and LFNO_b1 (b).

Figure 41 shows the diffractograms of the copper doped samples: LFCO_a2 and LFCO_b2. The peaks of metallic copper have been highlighted in green: for the

LFCO_a2 sample its presence is evident, this cannot be said for the LFCO_b2 sample. The presence of Cu in the LFCO_b2 sample was confirmed by subsequent tests: probably Copper was not detected in this analysis because in low quantities in the sample used, or due to the different synthesis method used - template deposition in sample a and deposition in the mixture of summary for the sample b.

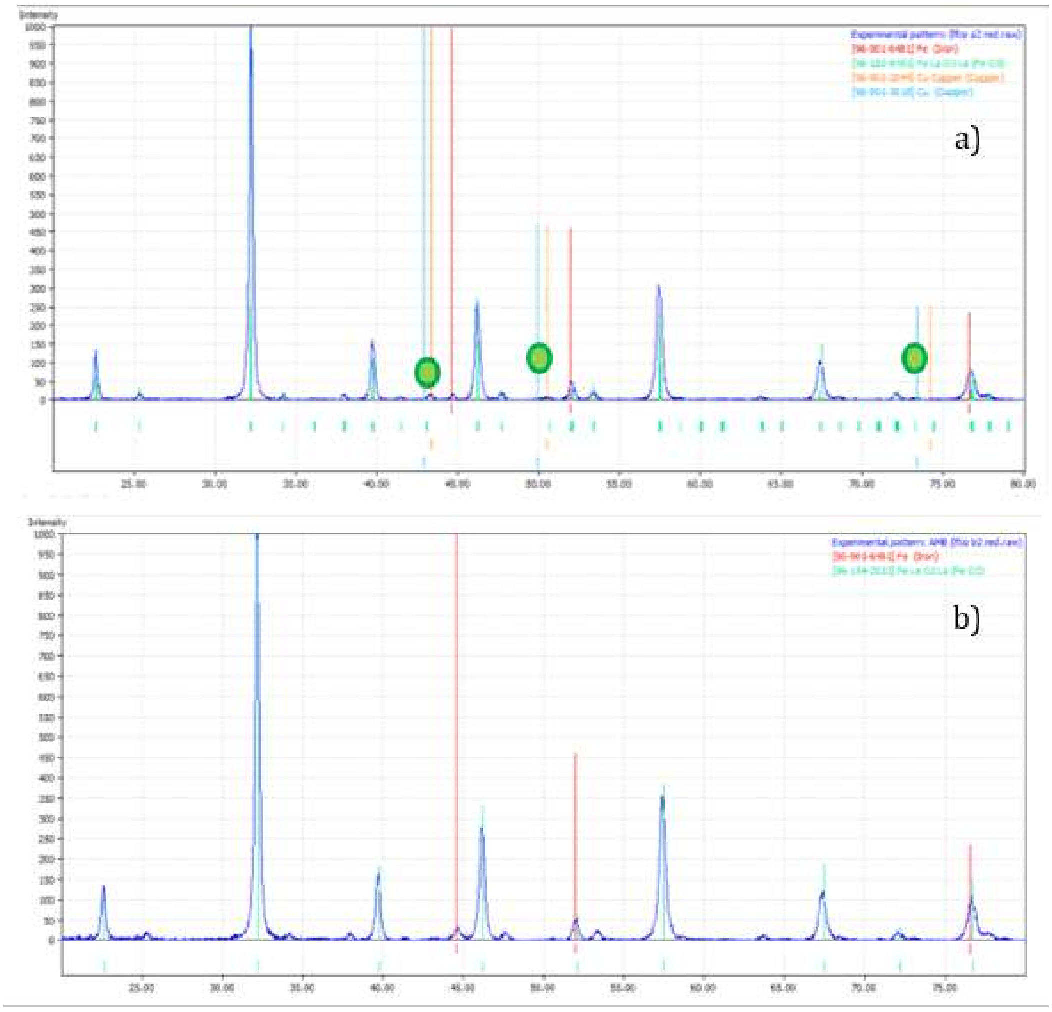

Figure 41: XRD spectrum of LFCO_a2 (a) and LFCO_b2 samples

Lastly, the graph in figure 42 shows the diffractograms of the samples doped with both in Ni-Cu catalysts: LFNCO_a3 and LFNCO_b3

The peaks of metallic copper have been highlighted in green and those of metallic nickel in yellow: for sample LFNCO_a3 the presence of metallic copper is evident while the presence of nickel is not noted, this cannot be said for sample LFNCO_b3 which shows the opposite situation. However, the presence of both nanocatalysts was confirmed in subsequent tests. As already said, this may be due to the different method of dopant deposition.

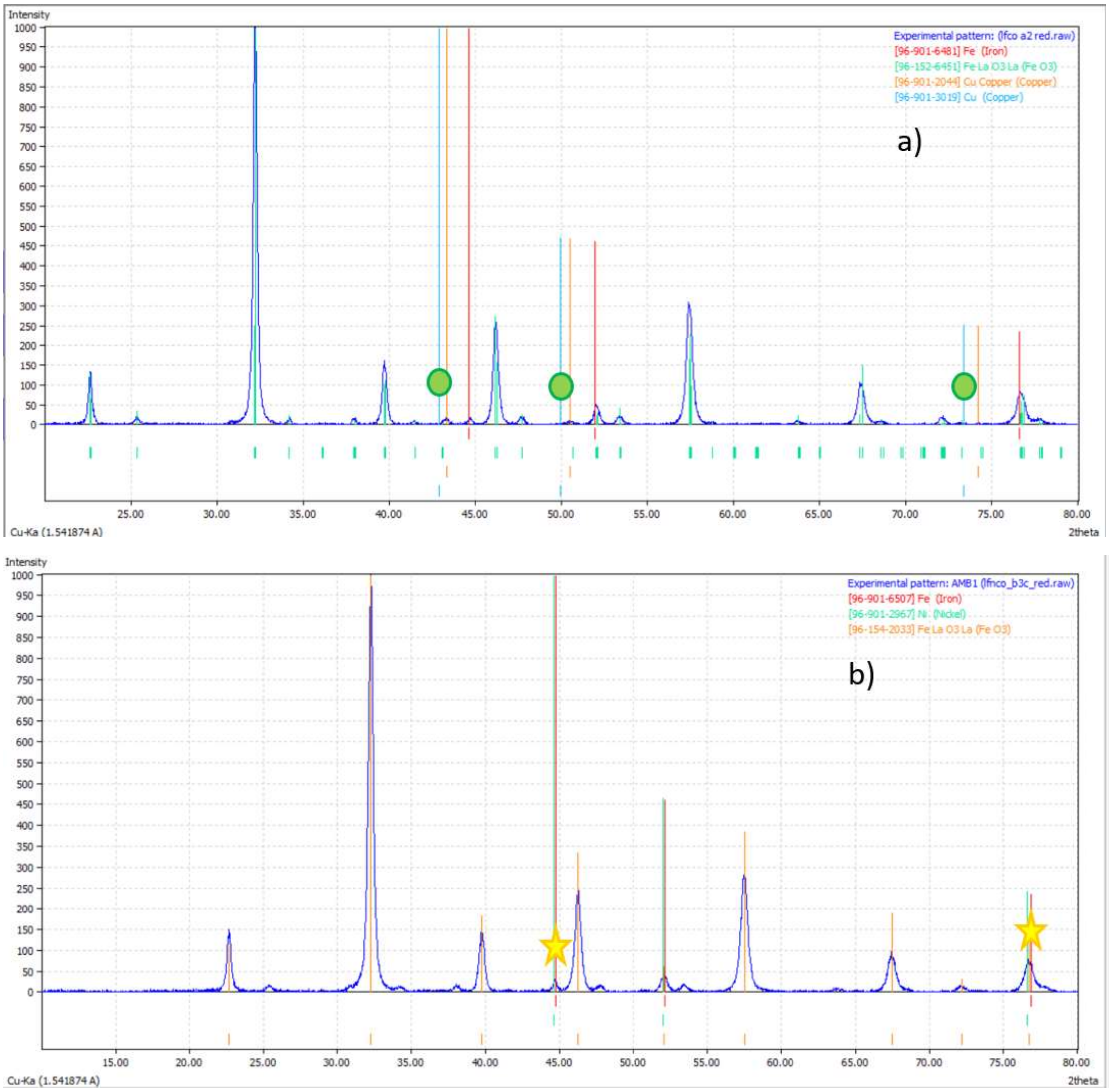

Figure 42: XRD spectrum of LFNCO_a3 (a) and LFNCO_b3 (b) samples

In conclusion, it can be said that XRD shown the formation of the desired perovskitic phase; only in Ba doped catalyst impurities of barium carbonate can be observed. No significant differences have been observed as a function of the synthesis procedure of the La-pervskite or the amount of complexant. After the templated deposition the active phase is observed (Ni or Cu) whereas the supporting perovskite structure is not modified. No traces of Ni and/or Cu have been observed in the catalysts obtained by exsolution. Likely this can be attributed to the lower amount of active species. However higher amounts of active species can not be inserted by means of this procedure (being dependent on the solubility of the precursor cations in the perovskite structure). The exsolution process (treatment under reductive atmosphere at high temperature) does not damage the perovskite structure. In the exsoluted samples, however, the presence of the metal nanoparticle could not be confirmed by XRD.

2. Temperature programmed reduction (TPR)

Through TPR analysis, it was possible to obtain the graph showing the percentage of hydrogen consumed with respect to the temperature increase. Data processing envisaged a fitting procedure, in order to identify the reduction temperatures of the species present in the sample.

The deconvolution of the curve using Gaussians was carried out using the OriginPro 8 software; at the peak of each curve, the temperatures of interest were identified, then compared with the literature data.

The fitting operation consisted of:

- draw a baseline that would allow for a closed curve to be obtained
- subtract the baseline from the curve of the experimental data
- identify the position of the peaks
- verify the fitting of the curve obtained by measuring R2

Data obtained through TPR analyses were compared with those obtained by Spinicci et al in 2002 during the analysis of perovskite samples with varying stoichiometric ratios, reported in Figure 43:

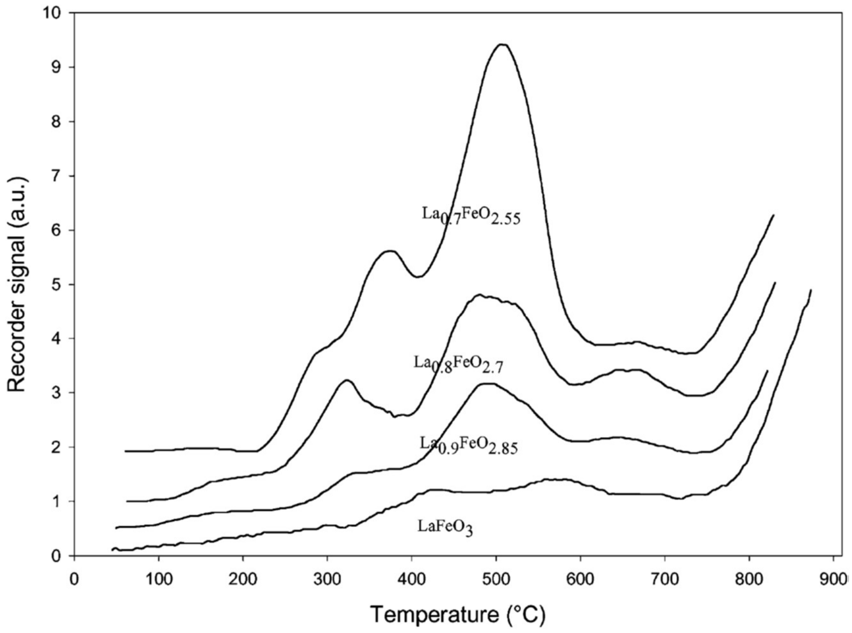

Figure 43: TPR spectrum of LaFeO3 from literature (45)

Fig. 44 shows TPR spectra obtained from undoped perovskites: apart from a peak at very high temperatures, two peaks are highlighted, at 300-350°C and at 450-500°C, respectively.

In the TPR spectrum of LFO_3 a third peak appears in addition to the two already described, probably due to the fact that in this type of support there is a large availability of oxygen, due to the different method of synthesis of the sample: the solution of synthesis, before proceeding with the dehydratation phase, was basified until a pH 7 was reached.

Comparing TPR results with those obtained by Spinicci et al, it is possible to observe that perovskite samples behave like the sub-stoichiometric "$La_{0.9}FeO_{2.85}$" sample, which is expected, since the synthesis procedure for all samples was performed to achieve slight La deficiency.

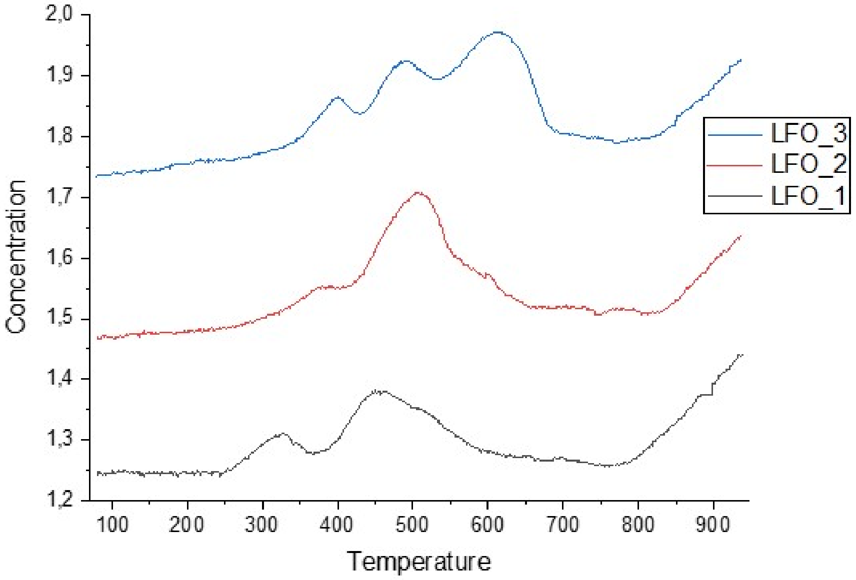

Figure 44: TPR spectrum obtained from undoped perovskite on a H2+Ar flux

Fig. 45 and 46 show TPR spectra obtained from Ni B-doped samples and Cu B-doped samples: the results reported for Ni doped samples are very similar to those obtained from undoped samples, while those reported for Cu doped samples are quite different, with two peaks at lower temperatures: the former is detected at temperatures between 200 °C and 400 °C, while the latter is detected at 450-500 °C.

The large size of the crystallites of pure NiO slow down the hydrogen diffusion process and, consequently, the reduction of the nickel oxide occurs in two stages suggesting that two not-equivalent NiO particles are present in the catalyst:

$$NiO \rightarrow Ni^{2+} + Ni^{0}$$

The first stage is observed at temperatures around 400°C, while the second is observed around 550°C. In general, however, the entity of the second reduction peak is much lower than that of the first peak, showing that the nickel oxide is almost totally reduced to metallic nickel already in the first stage.

Copper oxide is reduced more easily, in fact the first peak is observed at temperature of about 200-220°C.

$$CuO \rightarrow Cu^{2+} + Cu^{0}$$

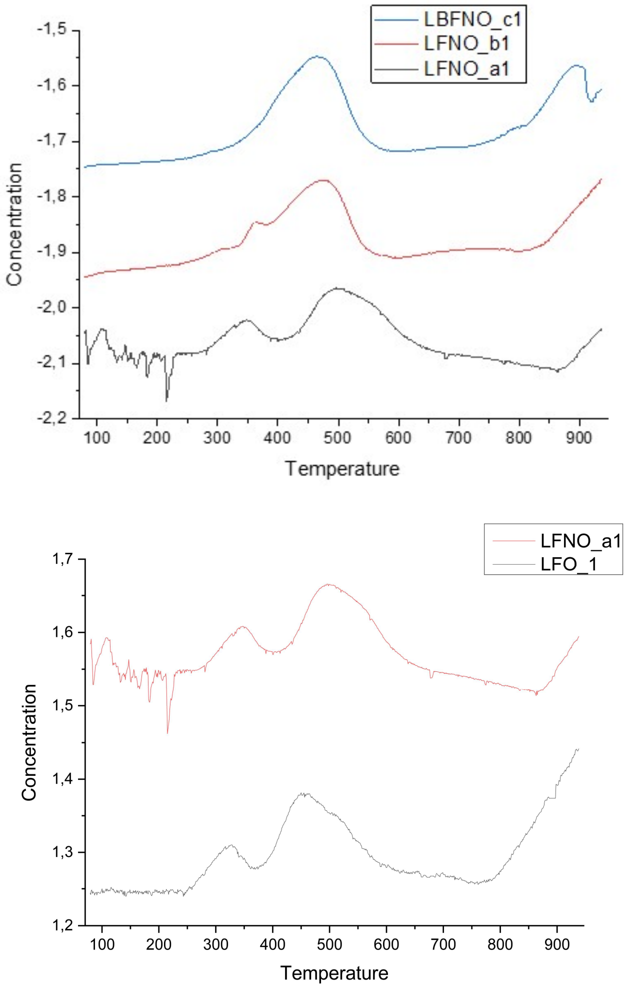

Figure 45: TPR spectrum of the nickel-doped perovskite and comparison with the starting undoped perovskite (LFO_1, LFNO_a1 template impregnation)

It is interesting to observe that the presence of nickel does not cause evident variations on the perovskite reduction, probably due to the low doping (5%).

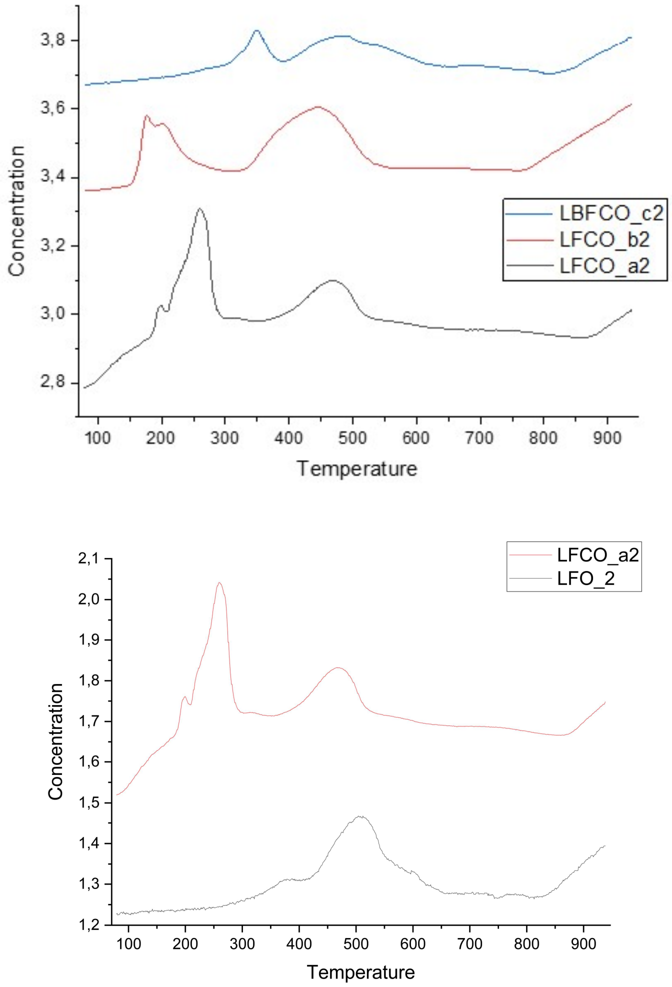

Figure 46: TPR spectrum of the copper-doped perovskite and comparison with the starting undoped perovskite (LFO_2, LFNO_a2 template impregnation)

Significant differences are observed in the three samples containing copper. In sample LFCO_a2 the reduction is centered at around 250°C whereas in LFCO_b2 two reduction peaks are observed at 180 and 200 °C, moreover the amount of H2 consumed is differently distributed in the two cases, with a relevant amount of H2 uptake at about 250 °C for LFCO_a2 and at about 450°C in LFCO_b2. These results suggest that the presence of copper on the surface of the perovskite (as a consequence of the specific preparation procedure) enhance the reducibility of the sample whereas when copper is obtained by exsolution this effect is less evident.

It is interesting to note that the deposition of copper on the undoped sample allowed to drastically lower the reduction temperature of the perovskite compared to the undoped one: in fact, the first peak of the LFCO_a2 sample can be observed at about 200°C compared to 350 °C of the first peak of the LFO_2 sample. The insertion of Ba as a dopant in site A seems to decrease the reducibility of the catalyst: signals move toward higher temperature and are less intense.

Fig. 47 shows TPR spectra obtained from Ni-Cu alloy B-doped samples: the results are between those found for Ni doped samples and those found for Cu doped samples.

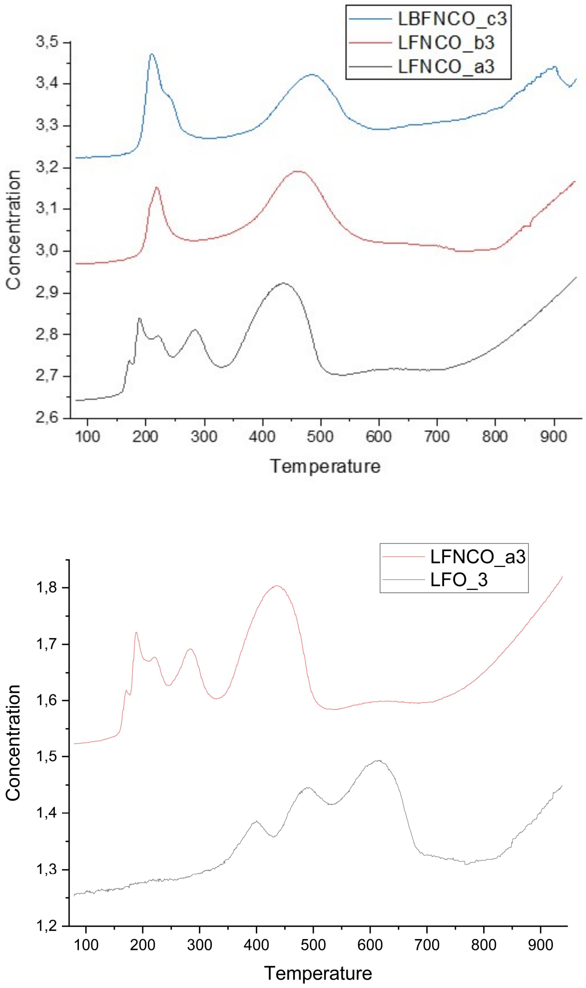

Figure 47: TPR spectrum of the nichel-copper-doped perovskite and comparison with the starting undoped perovskite (LFO_3, LFNCO_a3 template impregnation)

Also, in this case it is observed that the reduction of the doped sample (LFNCO_a3) starts at much lower temperatures than the starting undoped one (LFO_3), furthermore in the doped perovskite there is no peak at temperatures between 500 and 700°C.

As a result of B doping of perovskite with both nickel and copper, two well defined peaks are observed: the former is found at temperatures of about 150-200°C, the latter is observed at temperatures between 400 and 500°C.

The first peak represents the hydrogen consumption due to complete reduction of all copper oxide species: several component, in fact, seem to be present in this signal so suggesting the presence of Cu(II) in different enviroments. The second peak represents the reduction of nickel superimposed to the reduction of the iron cations of the supporting perovskite.

However, it must be considered that the defectiveness of lanthanum introduces increasing distortions on the surface and in the bulk.

Fig. 48 shows TPR spectra obtained from A doped samples, with different B site dopants: it is noticeable that A doped samples do not share any similarity in their behaviour, except the peak at 450-500 °C, which is common for all perovskite samples.

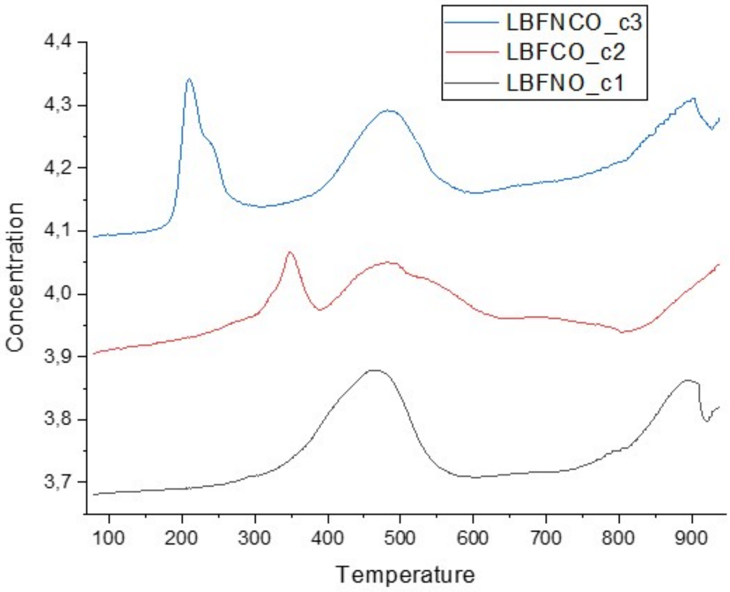

Figure 48: TPR spectrum of perovskite doped in A with barium and in B with nickel (c1), copper (c2) and nickel-copper (c3)

The greater deformation stimulates the formation and presence of defective layers inactive for combustion. This decreases the reducibility increasing the reduction temperature. This is less evident in the catalyst doped in B with both Cu and Ni.

From the calculation of the area under the curve it was possible to determine the percentage of hydrogen consumed as a function of the temperature (Table 10):

Table 10: percentage of hydrogen consumption by the sample, as a function of its mass

	Sample mass (g)	Hydrogen consumed (mol)
LFO_1	0.05	0.22
LFO_2	0.05	0.22
LFO_3	0.05	0.35
LFNO_a1	0.05	0.25
LFCO_a2	0.05	0.26
LFNCO_a3	0.05	0.43
LFNO_b1	0.05	0.25
LFCO_b2	0.05	0.60
LFNCO_b3	0.05	0.63
LBFNO_c1	0.05	0.30
LBFCO_c2	0.05	0.57
LBFNCO_c3	0.05	0.36

Samples LFO_1 and LFO_2 show a similar behavior while LFO_3 seems to have a higher hydrogen absorption, due to the basification of the synthesis mixture until a pH equal to 7 is reached. A slight increase of hydrogen consumption is observed in the Ni-doped catalysts, particularly when Ni is deposited by template deposition. The same goes for the samples doped with Cu: in this case, however, a significant increase in the consideration of hydrogen absorption in the exsolved sample is evident. From table 9 it is possible to notice that the samples doped in A site have a similar tendency to consume hydrogen compared to the other samples, this implies that the doping in A does not cause important variations on the reducibility of the sample. However, the catalyst deposition method has an important impact on the reduction: it can be observed that the samples whose catalysts have been deposited by template impregnation (LFNO_a1, LFCO_a2 and LFNCO_a3) consume less hydrogen than those in which the catalysts have been placed directly in the synthesis solution (LFNO_b1, LFCO_b2 and LFNCO_b3).

Therefore, it is expected to have better catalytic performances for the samples doped in A with barium and in B with the NiCu alloy, and worse performances for the samples whose dopants have been deposited by template impregnation.

3. Scanning electron microscopy (SEM)

Because of the application in heterogeneous catalysis, it is important to investigate the size, shape and morphology of the prepared nanomaterials. The synthesis conditions influence the structure, morphology and size distribution of the nanostructures.

In view of this, the morphology of La-perovskite nanoparticles was studied by SEM analysis.

The SEM results show that the different synthesis modes originate different morphologies. The perovskites synthesized by sol-gel method have an open flake-type morphology characterized by a large surface area; similar consideration holds for, those whose active cations been deposited by template-impregnation:

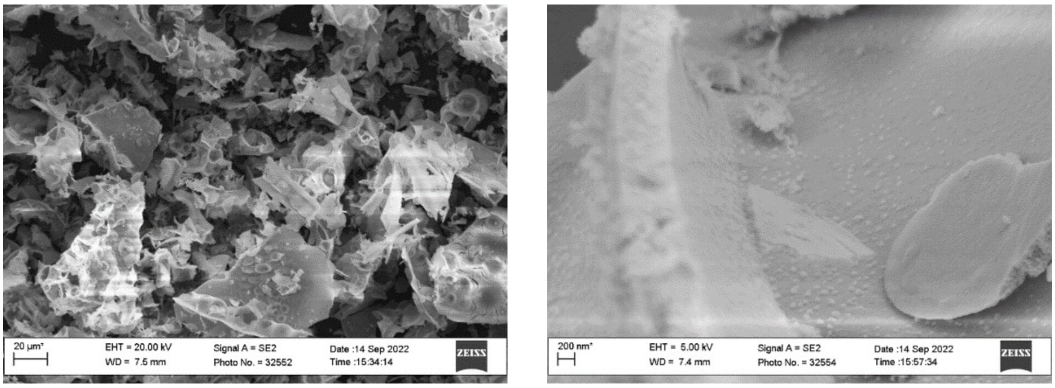

Figure 49: SEM photo of LFO_1 at 1000 and 50.000 magnification

In Figure 49, as an example, we can see the morphology of the undoped sample LFO_1, which was synthesized with an excess of citric acid. This has an open flake structure, with very large crystals.

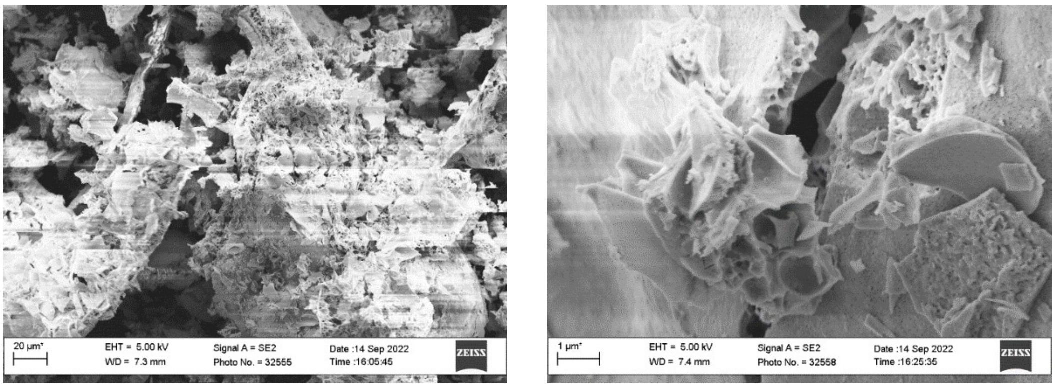

Figure 50: SEM photo of LFO_2 at 1000 and 25000x magnification

With the decrease in the quantity of citric acid, a structure is always obtained with open flakes but with a slight tendency to agglomeration: figure 50 shows a section of the sample LFO_2, in the highlighted area it is possible to observe the agglomeration, given by a set of approximately spherical particles (Fig. 51).

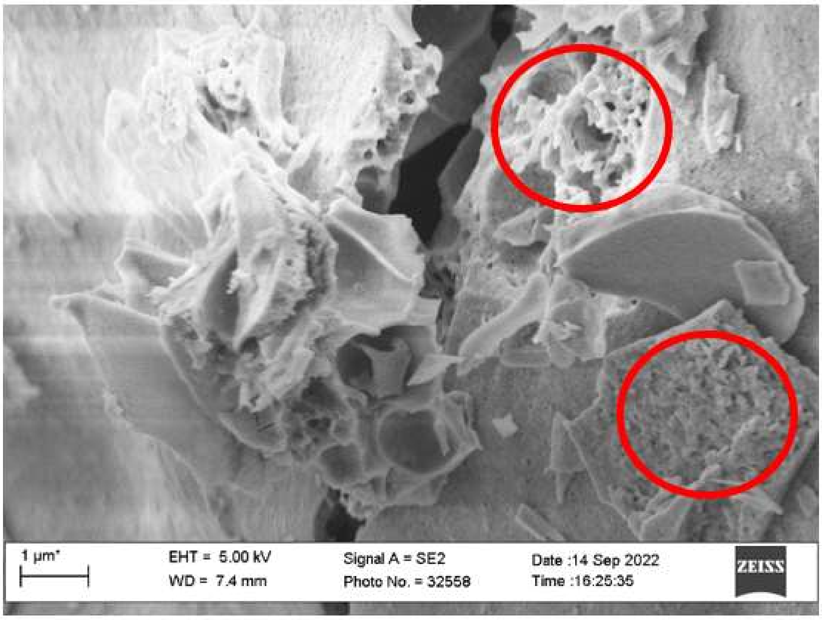

Figure 51: Highlighting areas with agglomeration.

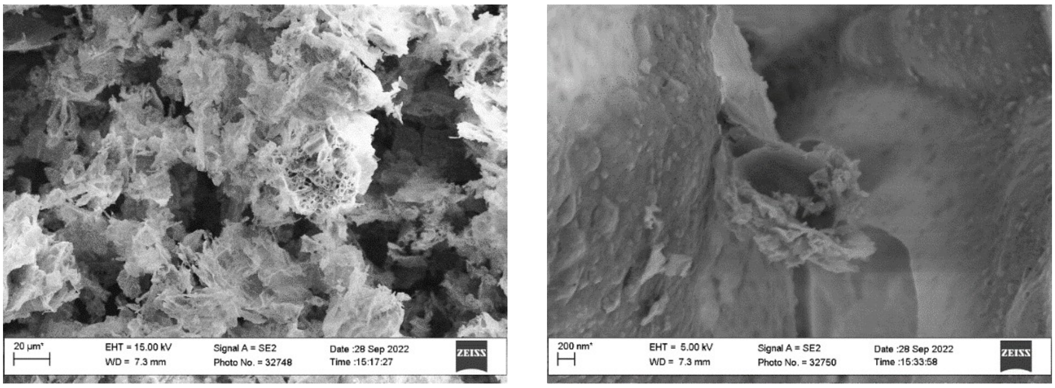

Figure 52: SEM photo of LFO_3 at 1000 and 25000x magnification

Figure 52 instead shows the images of the LFO_3 sample, which was basified during the synthesis. Also in this case, as in the LFO_1 sample, an open flake morphology with large particles is observed.

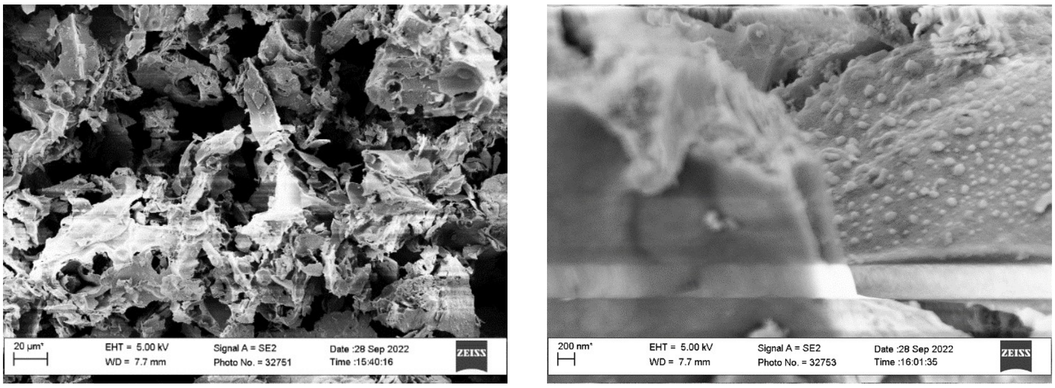

Figure 53: SEM photo of LFNO_a1 at 1000 and 50000x magnification

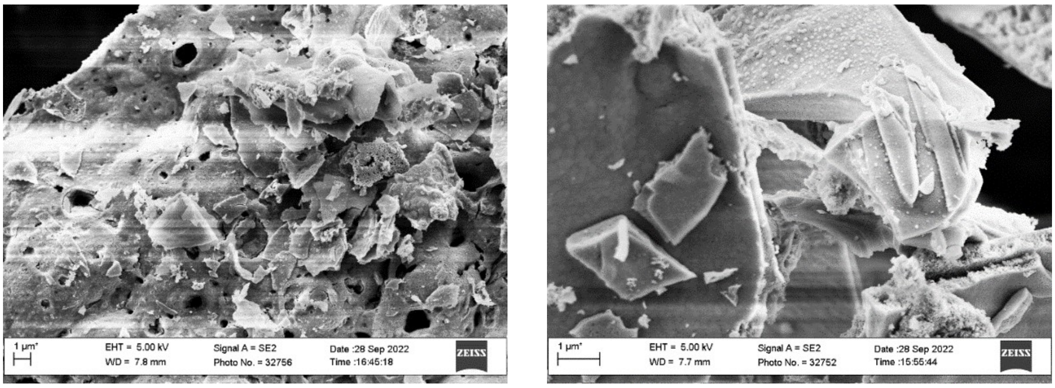

Figure 54: SEM photo of LFCO_a2 at 10000 and 25000x magnification

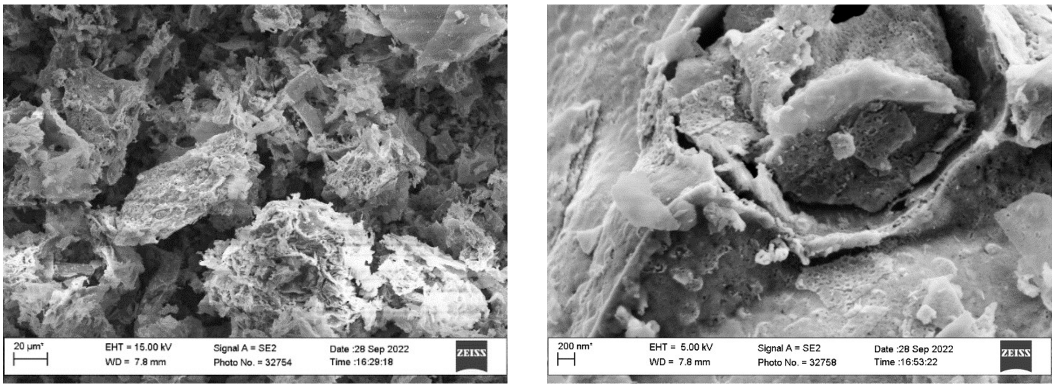

Figure 55: SEM photo of LFNCO_a3 at 1000 and 50000x magnification

In Figures 53, 54 and 55 the doped LFNO_a1, LFCO_a2 and LFNCO_a3 samples are compared; these catalysts have been, produced by template impregnation of the LFO_1, LFO_2 and LFO_3 samples, their morphology is not different from the previous images thus underlying that the deposition of the active cation does not affect the morphology.

For the B-doped samples, whose dopants have been included during the synthesis, there is always an open flake structure, but a tendency to agglomeration can be observed, with the formation of structures with approximately spherical morphology. However, it was not possible to observe this structure at higher magnifications as the sample has a tendency to become electrically charged, thus giving an out-of-focus image, with black and other white areas. The morphology of these specimens can therefore be observed only up to 50000x magnification (Figure 56):

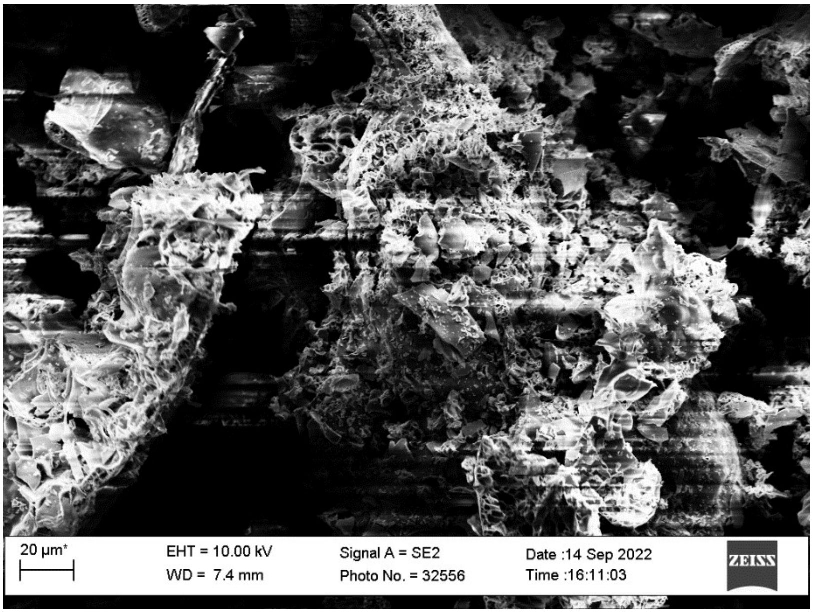

Figure 56: sample picture with sample load

As an ideal reference, results obtained by Kaiwen et al in 2015 (46) during the SEM analysis of pure phase perovskite samples produced through the same methods adopted in this study - co-precipitation (a) and combustion (b) - are reported in Figure 57.

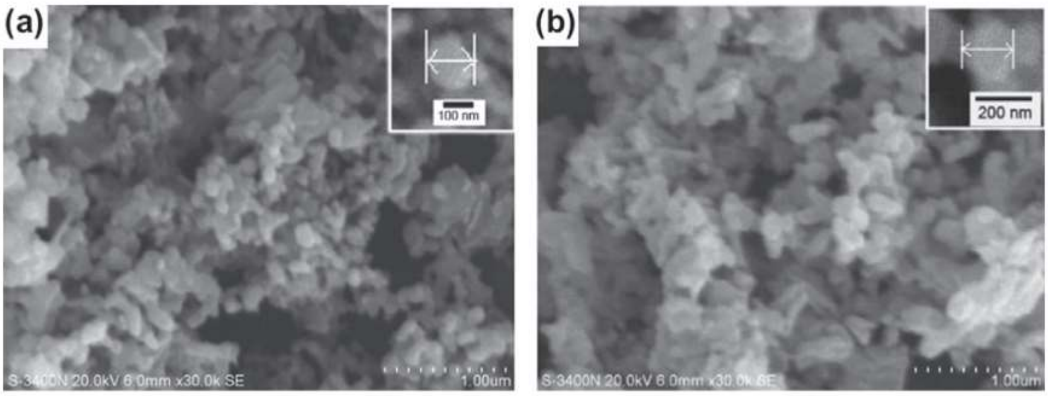

Figure 57: SEM images of two LaFeO3 samples from literature (46)

In LFNO_b1, LFCO_b2 and LFNCO_b3 a marked agglomeration is observed with the formation of compact sheets (Fig. 58, 59 and 60).

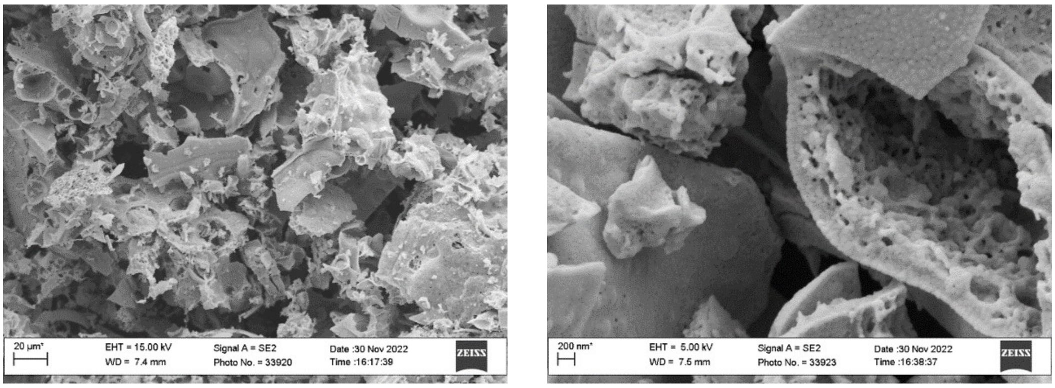

Figure 58: SEM photo of LFNO_b1 at 1000 and 50000x magnification

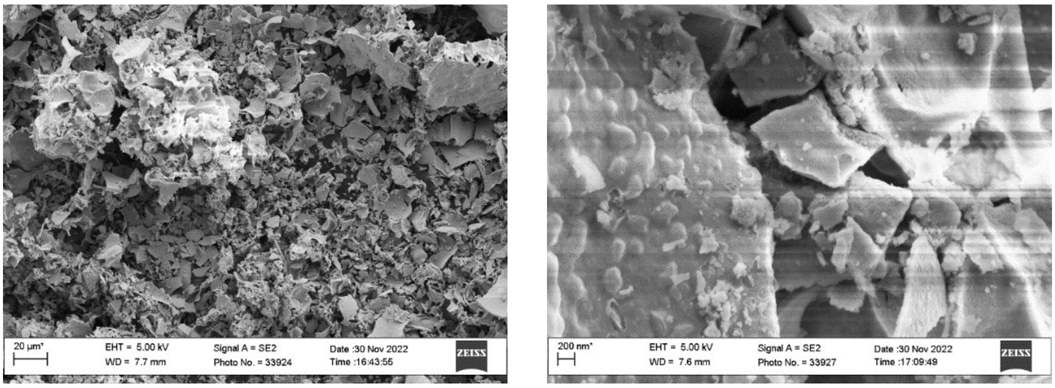

Figure 59: SEM photo of LFCO_b2 at 1000 and 50000x magnification

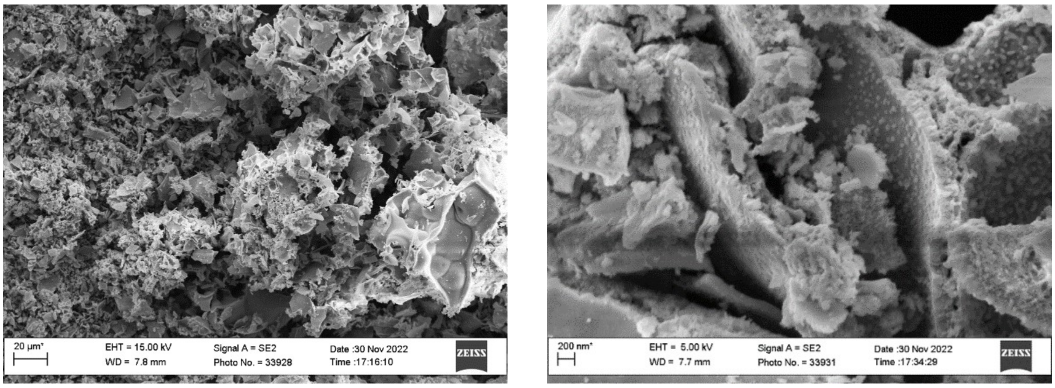

Figure 60: SEM photo of LFNCO_b3 at 1000 and 50000x magnification

As regards the samples doped in both A and B, an open flake structure with a tendency to agglomeration is always observed. However, even in this case it was not possible to obtain images at high magnifications, the greatest magnification obtained was that at 25000x (Fig. 61, 62 and 63).

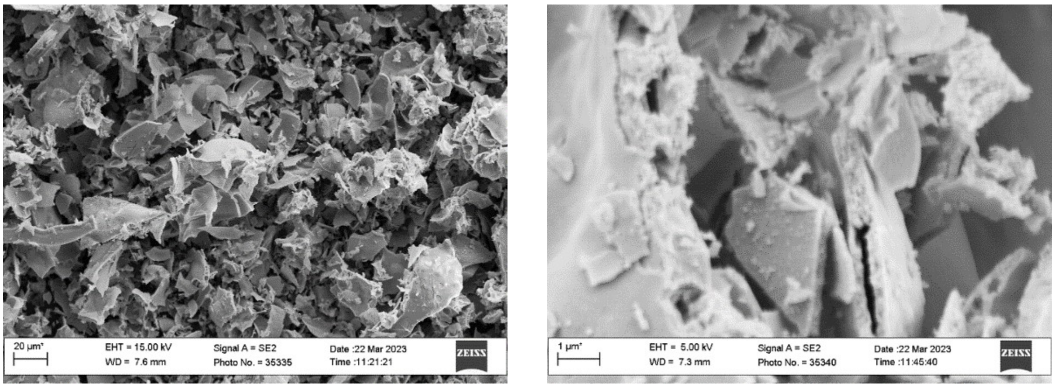

Figure 61: SEM photo of LBFNO_c1 at 1000 and 25000x magnification

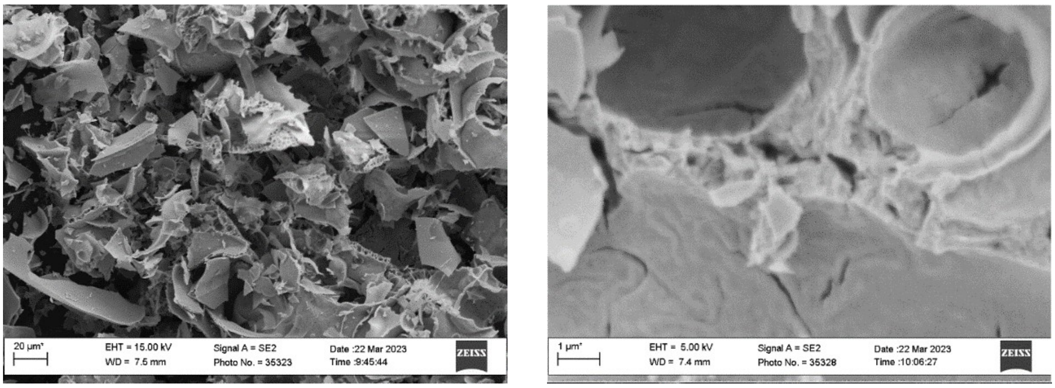

Figure 62: SEM photo of LBFCO_c2 at 1000 and 25000x magnification

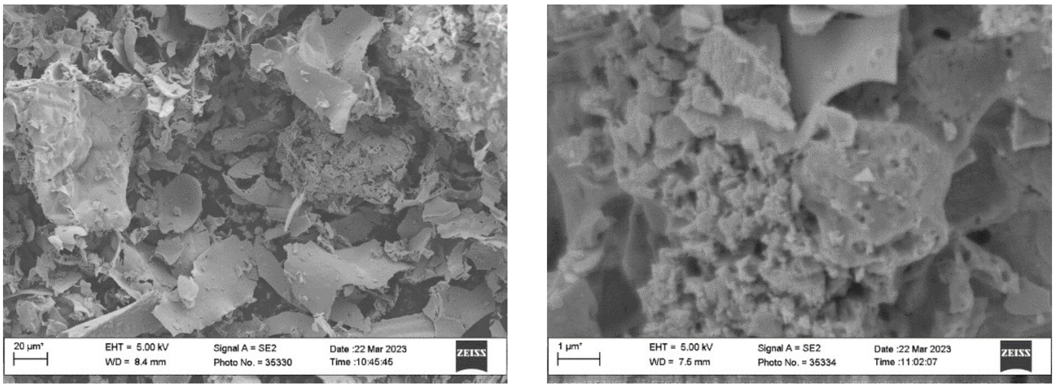

Figure 63: SEM photo of LBFNCO_c3 at 1000 and 25000x magnification

In conclusion, from the SEM images it can be seen that the different methods of inclusion of the dopant in the system cause the formation of different morphologies:

- in the case of template impregnation a flaky structure is obtained with a very small surface area, having large particle sizes
- in the case of inclusion of the dopant during the synthesis, a structure formed by agglomerates of small size particles with a spherical structure is obtained.

4. X ray energy dispersion (EDX)

Elemental analysis of the sample is performed using energy dispersive X-ray spectrometer (EDX). As a general consideration EDX result clearly shows that the samples contain La, Fe, Cu, Ni and Ba without any impurities.

Quantitative EDX analysis verified that dopants Cu, Ni and Ba are present in amounts close to the expected concentration.

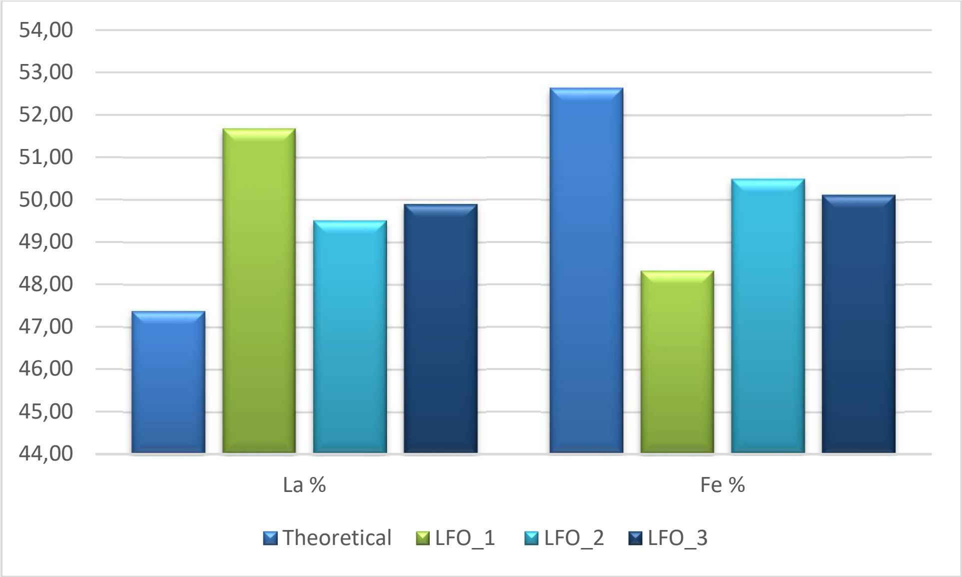

Figure 64: comparison of the theoretical and real atomic percentage of the elements present in the undoped samples

Table 11: stoichiometric La/Fe ratios for undoped samples

	Theoretical	LFO_1	LFO_2	LFO_3
La/Fe	0,90	1,07	0,98	1,00

The elemental composition of the $LaFeO_3$ nanoparticles for the undoped samples, obtained both by EDX analysis are compared with the theoretical ones determined by the weighted amounts. As can be seen in figure 64, the percentage quantities of the elements making up the sample are not agreement with the theoretical data, given that all the undoped samples show very high quantities of lanthanum and low quantities of iron. However, the atomic ratio La:Fe in the prepared sample was found to be 0,90:1,07 which is rather consistent with the theoretical value determined from the weighted amount of precursors (Table 11); such different observations between atomic percentages and ratios may be due to a tendency for lanthanum to position itself in the bulk of the material and for iron to position itself on the surface. This indicates that the entire metal content of the precursors was successfully transferred to the final sample under the synthesis conditions: It is worth mentioning that no carbon content was detected in these nanoparticles which can be attributed to the complete decomposition of the carbonaceous compounds from the gel by the calcination process the optimized temperature, i.e. 600°C.

A second EDX analysis was performed on the samples doped in B by template impregnation (fig. 65):

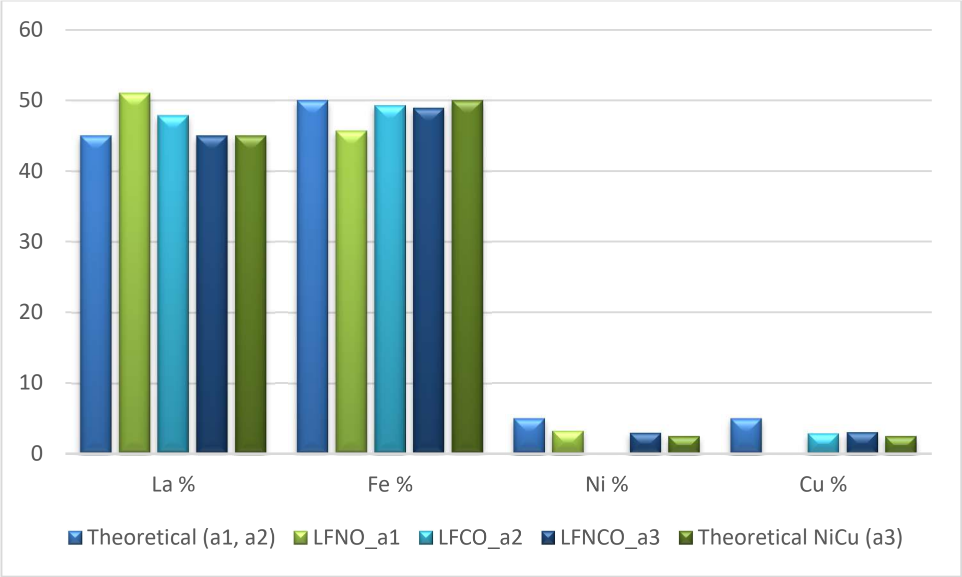

Figure 65: comparison of the theoretical and real atomic percentages of the elements present in the B-doped samples by template impregnation

The B-doped samples via template impregnation show good agreement between theoretical and experimental atomic percentages. Except for the catalysts which tend to have slightly lower percentages, due to their presence on the surface of the material.

This can be confirmed by analyzing the stoichiometric ratios between the various elements (tab. 12):

Table 12: stoichiometric ratios between the various elements that make up the samples doped by templated impregnation

	Theoretical	LFNO_a1	LFCO_a2	LFNCO_a3
La/Fe	0,9	1,12	0,97	0,92
La/Ni	18	15,54		14,94
La/Cu	18		16,46	14,68
Fe/Ni	20	13,91		16,23
Fe/Cu	20		16,96	15,95

From table 12 it is possible to observe that the ratio between the elements that form the perovskite (La and Fe) remains unchanged. However, the stoichiometric ratios La/dopants tend to be slightly lower, this may be due to the presence of the catalyst on the surface, due to the method of its deposition; the segregation of the active phase on the surface could be very beneficial for catalysis.

As regards the B-doped samples, whose dopants were introduced into the precursor solution, a third EDX analysis campaign was performed (fig. 66):

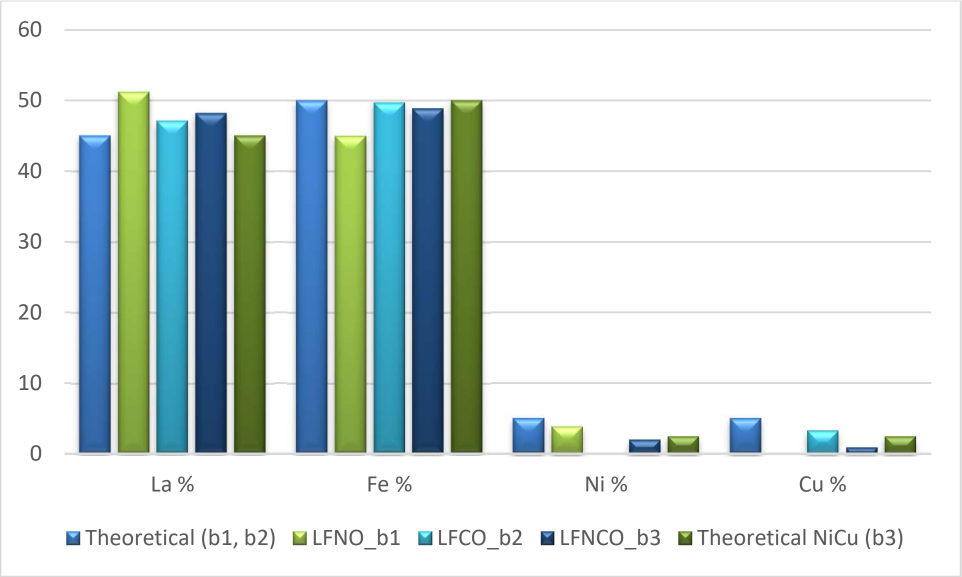

Figure 66: comparison of the theoretical and real atomic percentages of the elements present in the samples doped in B.

Also in this case it can be observed that the atomic percentages of the elements constituting the samples are close to the theoretical value, with La always present in a higher amount respect to the expected stoichiometry and Fe sub-stoichiometric in LFNO_b1. Ni and Cu seems to be present in slightly high amount in LFNO_b1 and LFCO_b2, respectively. For a broader vision it is necessary to study the atomic ratios between the cations (tab. 13):

Table 13: stoichiometric ratios between the various cations composing the doped samples.

	Thetoretical	LFNO_b1	LFCO_b2	LFNCO_b3
La/Fe	0,9	1,14	0,95	0,99
La/Ni	18	13,24		23,79
La/Cu	18		14,46	51,55
Fe/Ni	20	11,64		24,13
Fe/Cu	20		15,26	52,29

The La/dopant atomic ratios seem lower than the theoretical value suggesting a higher presence of dopant. In the double doped sample, in contrast, La and Fe are prevailing and this is particularly evident for the copper containing sample.

Lastly, a final EDX analysis was also performed for the doped samples in both A and B (fig. 67):

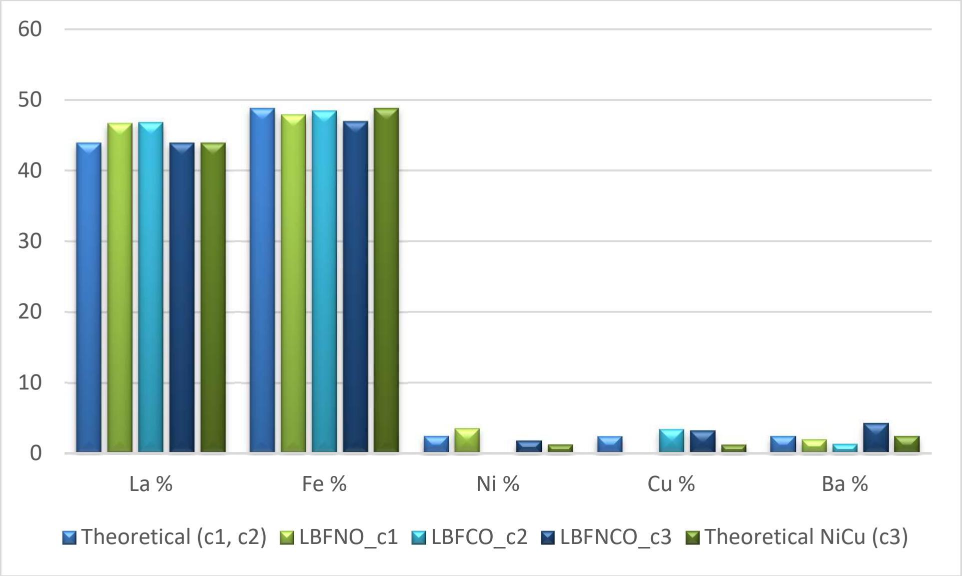

Figure 67: atomic percentages of the doped samples in both A and B

From this graph it seems that the atomic percentages of La in LBFNO_c1 and LBFCO_c2 are higher than expected while in LBFNCO_c3 the opposite is observed. The sample LBFNCO_c3 shows a higher amount of Ba with respect to the expected one while this is not observed in the other samples. Ni is present in slightly higher % in LBFNO_c1 and the same is true for Cu in LBFCO_c2. The atomic ratios are significantly different as can be seen in table 14:

Table 14: stoichiometric ratios between the various elements that make up the doped samples both in A and in B.

	Theoretical	LBFNO_c1	LBFCO_c2	LBFNCO_c3
La/Fe	0,9	0,97	0,97	0,93
La/Ni	18	13,33		24,89
La/Cu	18		13,57	13,72
Fe/Ni	20	13,68		26,63
Fe/Cu	20		14,04	14,68
La/Ba	18	23,73	35,39	10,43
Fe/Ba	20	24,35	36,61	11,16

Also, in this case this may be due to the presence of dopants in the structure, again due to the synthesis method used, since the precursors of the dopants were introduced directly into the reaction mixture.

5. X ray photoelectron spectroscopy (XPS)

The oxidation state of the main elements of $LaFeO_3$ samples can be determined by XPS.

The binding energies obtained in the XPS analysis are standardized for the sample charge using C 1s as a reference at 284.8 eV. Fig. 68 shows the XPS spectrum of La $3d_{5/2}$ core levels: two binding energy peaks are detected at 839.0 and 835.7 eV. The peak position and shape (with particular reference to the shake-up component at 839 eV) are consistent with the presence of La(III).

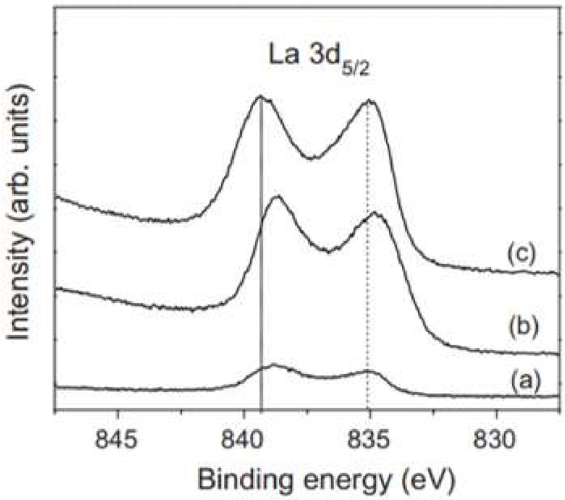

Figure 68: XPS spectra of La 3d for samples LBFCO_c2 (a), LFNO_b1 (b) and LFNCO_a3 (c)

The LBFCO_c2 sample has two slight peaks, probably because of the reduction in the intensity of the bond determined by the presence of A site doping with barium, which shows a tendency to deformation of the bonds involved in the structure. The LFNO_b1 and LFNCO_a3 samples show peaks of similar intensity: these samples are identical in composition, with the exception of B doping; the amount of dopant, however, is too low to be detected by XPS. However, these samples differ in the type of synthesis with which were produced: in the LFNO_b1 sample the catalyst precursors (Ni) were deposited directly in the synthesis mixture, while in the

LFNCO_a3 sample the catalysts (Ni and Cu) were deposited by template impregnation.

Figure 69 shows the XPS spectrum of Fe2p core levels, in detail $2p_{3/2}$ and $2p_{1/2}$, whose peaks are located at 709.8 and 724.3 eV, respectively. This peak position are consistent with the presence of Fe(III) in oxides.

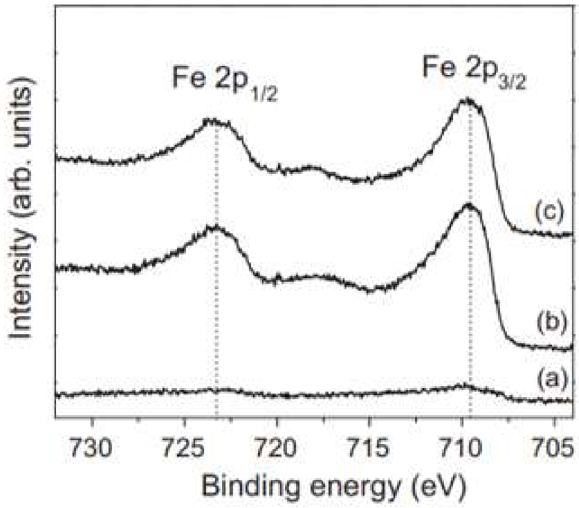

Figure 69: XPS spectra of Fe2p for samples LBFCO_c2 (a), LFNO_b1 (b) and LFNCO_a3 (c)

Also in this case a much lower intensity is observed for peaks relating to the LBFCO_c2 sample, presumably due to the presence of doping in A that induces the surface segregation of barium.

The O1s peak shows a main contribution at a binding energy of 530.7 eV (Fig. 70):

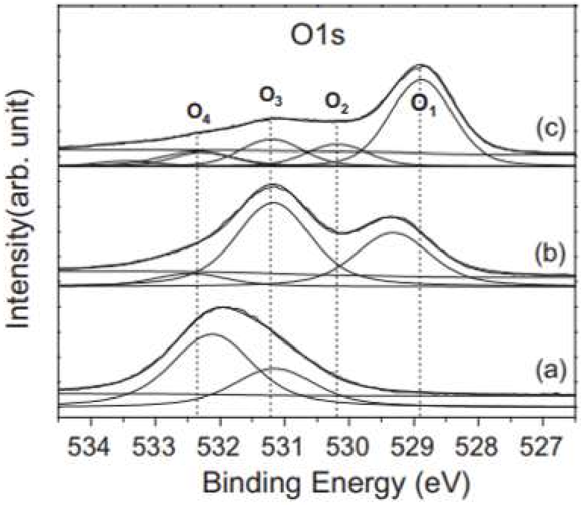

Figure 70: XPS spectra of O1s for samples LBFCO_c2 (a), LFNO_b1 (b) and LFNCO_a3 (c)

XPS O 1s spectra are broad and asymmetric, demonstrating that there are different types of O characterized by different chemical enviromental. Thus, XPS O 1s spectra were fitted with four components at 528,98eV (O1), 530,26eV (O2), 531,22eV (O3) and 532,47eV (O4). The O1 XPS signal is attributed to the contribution of La–O and Fe–O in the $LaFeO_3$ crystal lattice and its peak position is at approximately 528.8 eV. The components at higher binding energy are likely due to hydroxide and carbonate groups.

Surface elemental composition (%) was reported in Table 15 and Figure 71 for the LFNCO_a3 sample, respectively post reaction and post exsolution:

Table 15: atomic percentages of the cationic components of LFNCO_a3

	Exsolution	**Reaction**
La	14,18	23,90
Fe	13,34	21,14
C	63,54	43,96
Cu	7,65	6,50
Ni	1,28	4,50

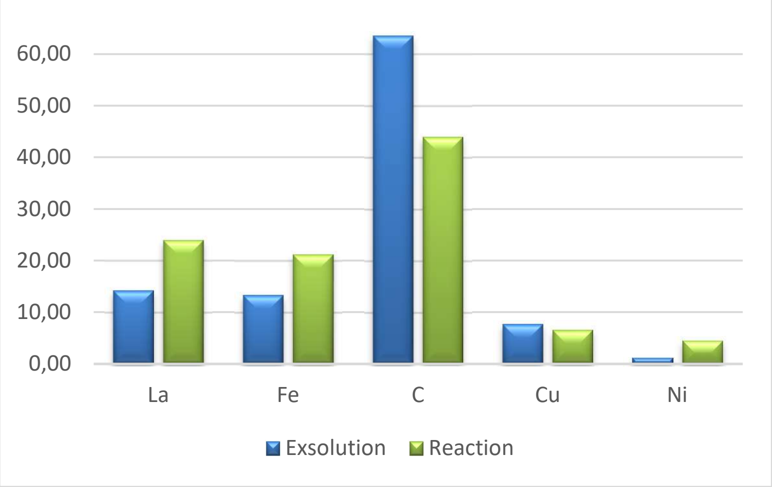

Figure 71: comparison of the percentage composition of the LFNCO_a3 sample by XPS after reduction and after reaction

Higher percentages in the post reaction LFNCO_a3 sample, compared to post exolution, suggest catalyst retention on the surface of the material, which may be explained by the theory of protection of nickel by copper against coke poisoning.

By making a comparison with the EDX data (which can be considered more representative of bulk with respect to XPS) of the reduced sample in table 16 and figure 72, it can be noticed that EDX results shows a high atomic percentage of La and Fe, thus suggesting their presence in the bulk of the material: on the other hand, a lower atomic percentage of catalysts is observed, suggesting that those tend to be found on the surface of the material, also due to the deposition method of the dopants. XPS confirms the formation of the catalyst nanoparticles on the surface of the sample: in fact, a higher atomic percentage of the same is observed.

Table 16: EDX-XPS atomic percentage comparison of sample LFNCO_a3

	Nominal	EDX	XPS
La	46,14	45,01	38,9
Fe	51,27	48,91	36,6
Cu	1,29	3,07	21
Ni	1,29	3,01	3,5

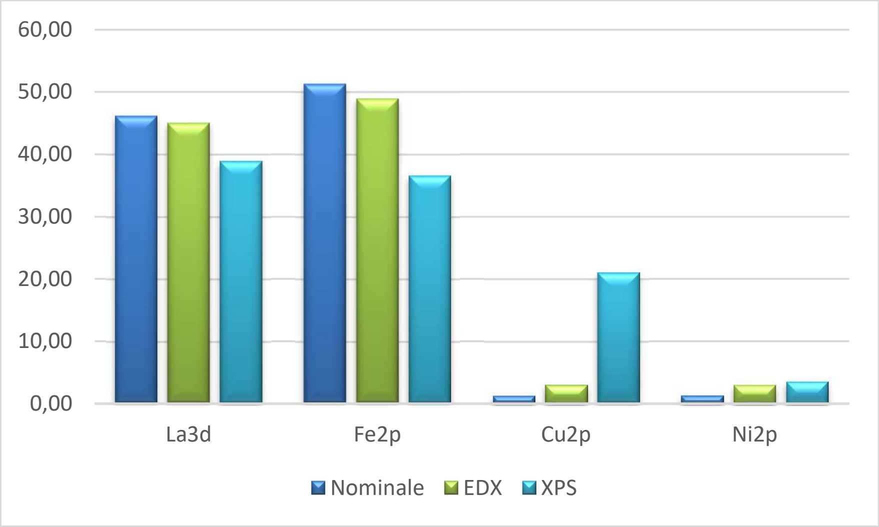

Figure 72: EDX-XPS atomic percentage comparison of sample LFNCO_a3

Table 17 and Figure 73 show the XPS atomic percentages of the constituents of the LFNO_b1 sample:

Table 17: atomic percentages of the components of LFNO_b1

	Exsolution	Reaction
La	20,80	15,64
Fe	21,30	13,61
C	55,59	67,19
Ni	2,31	3,55

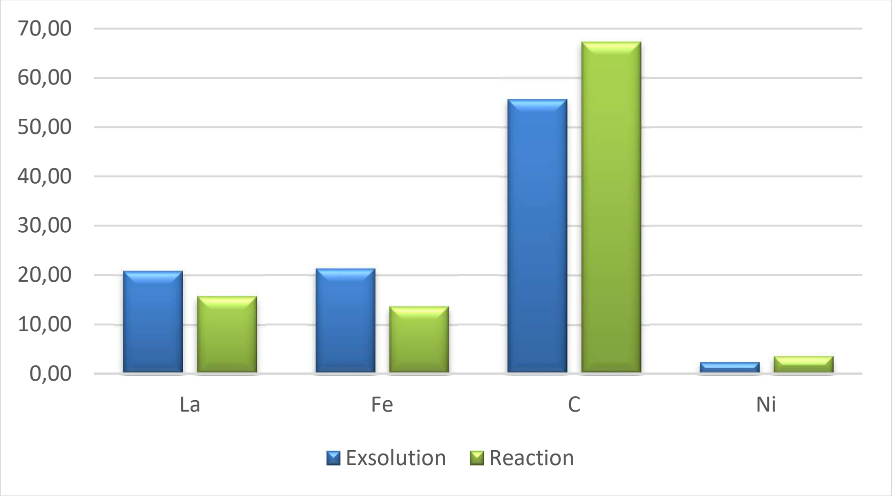

Figure 73: comparison of the percentage composition of the LFNO_b1 sample by XPS after reduction and after reaction

The atomic percentages of La remained approximately unchanged, but the atomic percentage of iron decreased during the reaction whereas Ni increases; this suggest the idea that Ni surface segregates as a consequence of reaction being thus the active element. In this comparison the amount of oxygen has been excluded as data could be offset by its presence in the atmosphere and in the quartz wool used as a sample support inside the reaction reactor.

Comparing with the EDX data we observe:

Table 18: Comparison of EDX-XPS atomic percentages of sample LFNO_b1

	Nominal	EDX	XPS
La3d5	39,01	38,13	39,01
Fe2p	43,08	43,81	43,08
Ni	7,89	10,10	7,89

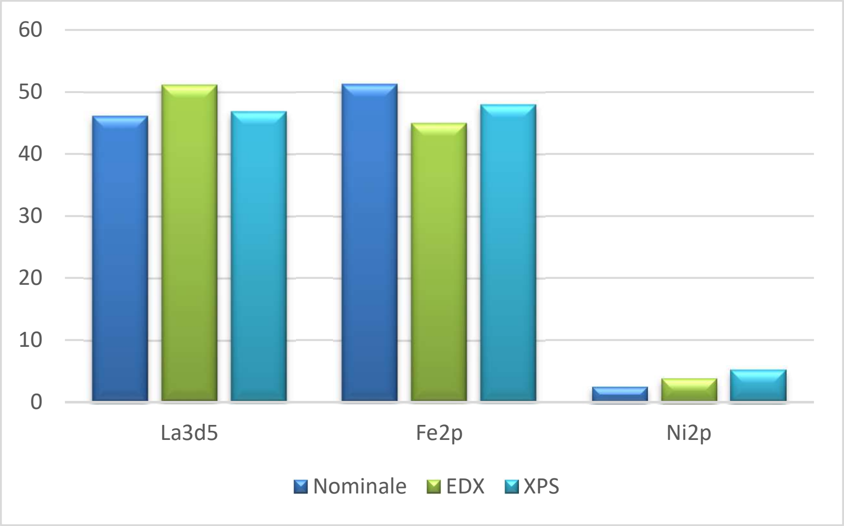

Figure 74: EDX-XPS atomic percentage comparison of the LFNO_b1 sample

From table 18 and from figure 74 it can be observed that EDX shows a very high atomic percentage of La and Fe, suggesting their presence in the bulk of the material. On the other hand, lower atomic percentages of the Ni catalyst is observed, also due to the low doping (5%) of the sample. The XPS data doesn't give much information about the location of the catalyst.

Lastly, in table 19 and figure 75 it is possible to observe the XPS atomic percentages of the constituents of the LBFCO_c2 sample:

Table 19: atomic percentages of the components of LBFCO_c2

	Exsolution	**Reaction**
La	17,76	18,30
Fe	19,61	21,03
C	54,48	51,99
Cu	3,59	4,85
Ba	4,56	3,82

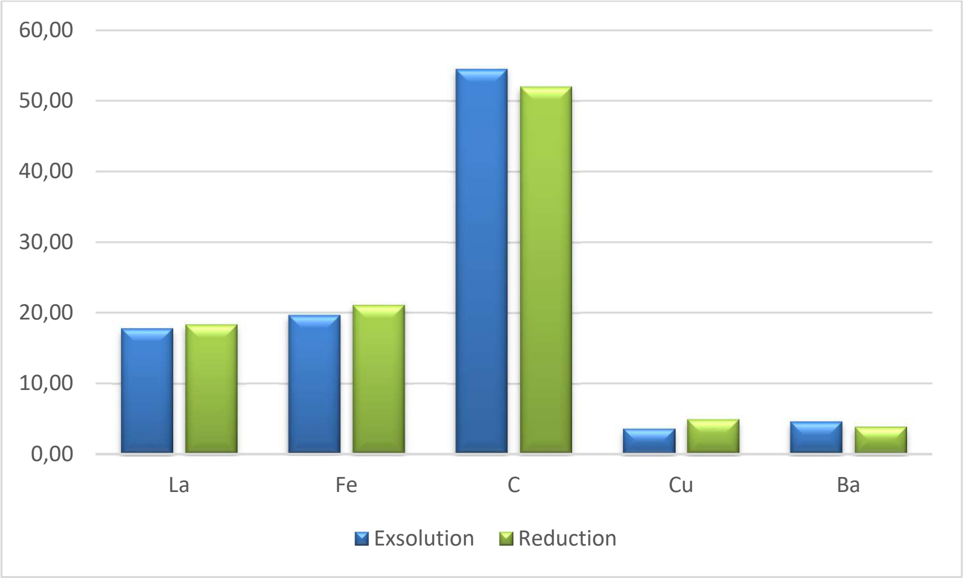

Figure 75: comparison of the percentage composition of the LBFCO_c2 sample by XPS after reduction and after reaction

The post reaction LFNO_b1 and LBFCO_c2 samples show the same atomic percentages, however in both cases, post reaction there is an increase in the amount of carbon on the sample surface, probably due to the sensitivity of the material to CO2. Since the La3p surface was sensitive to H2O and CO2 in the atmosphere, the carbonation process could occur with the formation of La-O-CO2 (47). Interesting is the increment of Cu and of Ni observed after the reaction underlining that these species are involved in the reaction.

Comparing EDX and XPS we observe:

Table 20: Comparison of EDX-XPS atomic percentages of the LBFCO_c2 sample

	Nominal	**EDX**	**XPS**
La3d5	45,00	46,81	39,01
Fe2p	50,00	48,42	43,08
Cu2p	2,50	3,45	7,89
Ba3d	2,50	1,32	10,01

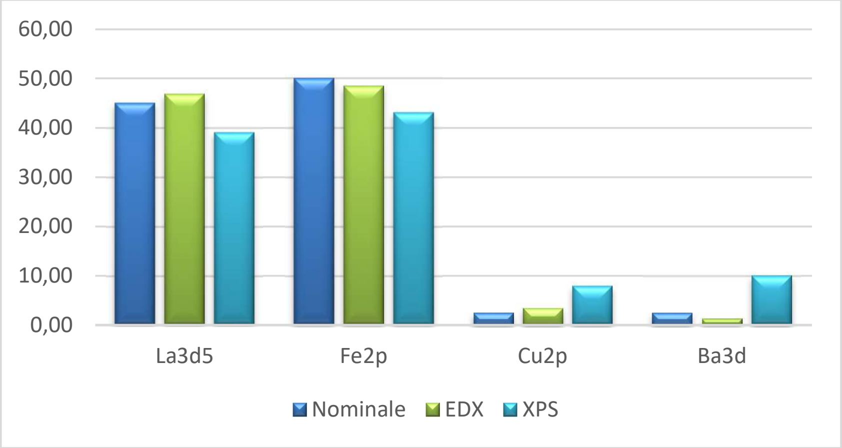

Figure 76: EDX-XPS atomic percentage comparison of the LBFCO_c2 sample

From table 20 and from figure 76 it can be seen that the EDX analysis shows an amount of La and Fe similar to the nominal one whereas XPS results underline the surface segregation of Cu and Ba. La and Fe, suggesting their presence in the bulk of the material, while a low atomic percentage of the Cu catalyst is observed, also due to the low doping (5%) of the sample. The difference in atomic percentage of Cu and Ba.

In conclusion, it is observed that the catalysts tend to increase after the reaction only with the deposition by template impregnation. This may be due to the different deposition method as, with the impregnation, the catalysts will position themselves on the surface of the sample, thus being less anchored to the sample. The other two samples were doped by inserting the metal precursors in the synthesis mixture, in this way the catalyst nanoparticles will position themselves inside the structure, thus protecting themselves from potential external pollutants.

6. Catalytic tests

The elements Ni and Cu have been used as active species in the $LaFeO_3$ perovskite, to study the effect of nanocatalysts on CO_2 conversion and CH_4 selectivity.

Functional activity assessment was carried out by the use of GC (Gas Chromatography) technique at atmospheric pressure. The inlet composition was varied according to the following CO2:H2 ratios: 1:4 (stoichiometric ratio, selected as the standard testing protocol). A quartz reactor (6 mm ID) with a packed bed of powders is employed, the temperature is monitored by a thermocouple right upstream of the bed. The inert carrier used was Ar and the reaction mixture was made up by H2 and CO2. The temperature of the bed was varied between RT and 500°C. The vapor in the outlet gas was condensed to avoid its presence in the GC columns (which could alter the detection results) and, as previously mentioned, the mixture was continuously analyzed by GC (Agilent 7820).

It can be seen from the reactivity of the catalysts determined at different temperatures (Fig. 77, 78, 79) that the conversion rates of CO_2 by doped $LaFeO_3$ are significantly higher than those of pure $LaFeO_3$, showing that doping can effectively improve the rate of CO_2 conversion.

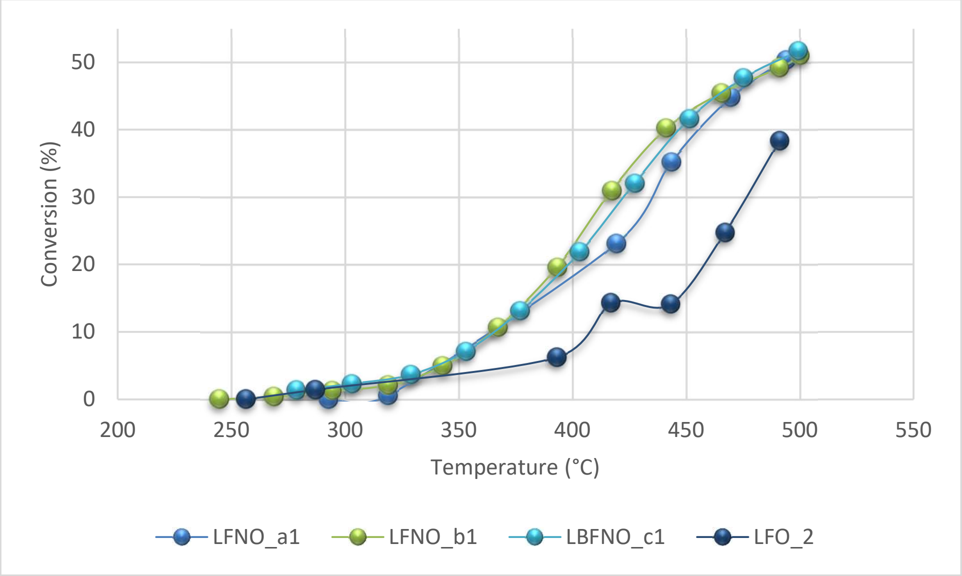

Figure 77: conversion-temperature graph of the Ni-doped samples

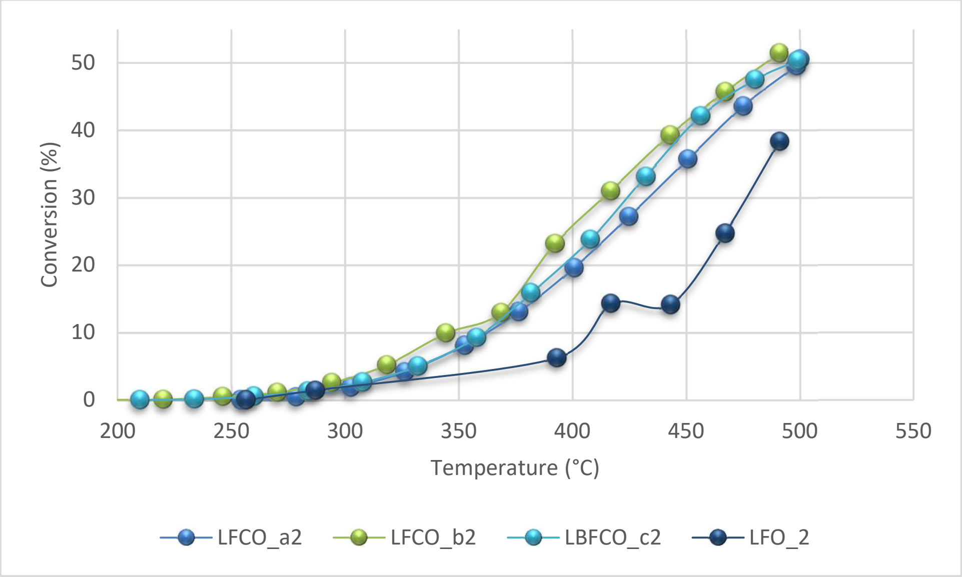

Figure 78: conversion-temperature graph of the Cu-doped samples

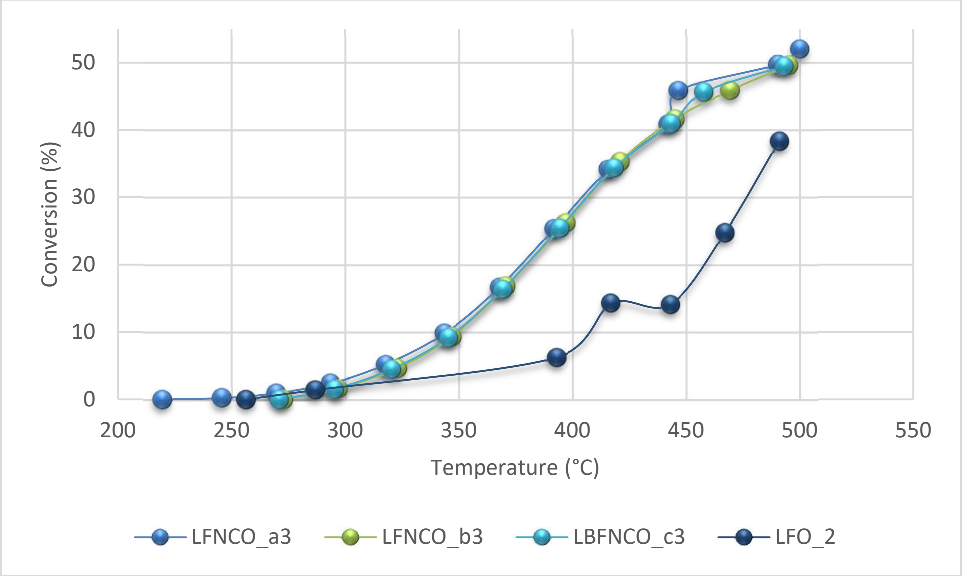

Figure 79: conversion-temperature graph of the NiCu-doped samples

Figures 80 and 81 show the conversions obtained for the LFNO_b1, LFCO_b2 and LFNCO_b3 samples. These catalysts showed better conversion than the others. In the kinetically controlled temperature range, different doping elements can lead to increased catalytic activity.

The conversion difference between 300°C and 450°C is significant. This result shows a certain sensitivity of the process in this temperature range. In general, the

Cu-containing nanocatalysts are slightly more active whereas barium seems to unfavor reactivity. The presence of both Ni and Cu, in contrast, enhances reactivity; the catalytic activity in terms of conversion, moreover, is not depending on the preparation procedure.

To investigate the performance of the samples according to the operating temperature, the CO_2 conversion kinetics were therefore evaluated through the differential conversions, calculated as follows:

$$C(T_i) = C_i - C_{i-1} = C(T_i) - C(T_{i-1})$$

Where C_i and $C_{(i-1)}$ are the conversions measured at temperatures T_i and $T_{(i-1)}$.

Fig. 78 shows the differential conversions for the LFNO_b1, LFCO_b2 and LFNCO_b3 samples (obtained by thermal treatment under reducing atmosphere of the precursor perovskite): from the graph, it can be seen that the optimal working temperature for the samples under examination is in a range indicatively between 370 °C and 450 °C.

Although the performance of the NiCu doped sample is slightly lower, it is interesting to note that the NiCu doping allows for the reduction of CO_2 starting from lower temperatures and the conversion peak is maintained in a wider temperature range (370°C – 430°C). Focusing on the Ni-doped samples, the presence of this active species promotes a higher conversion but at higher temperatures and with a sharp decrease when departing from the optimum temperature.

Doping with the NiCu alloy can show a good catalytic effect and an improvement in the CO_2 conversion activity: this could be explained by the "ensemble control" theory: as explained by Wang and Lua (2015) (15) during investigation of the catalytic activity of Ni-Cu alloy nanoparticles, “ensemble control” involves the dilution of the nickel with the copper, the separation of the Ni active sites from each other and thus reduces the rate of encapsulation and carbon formation.

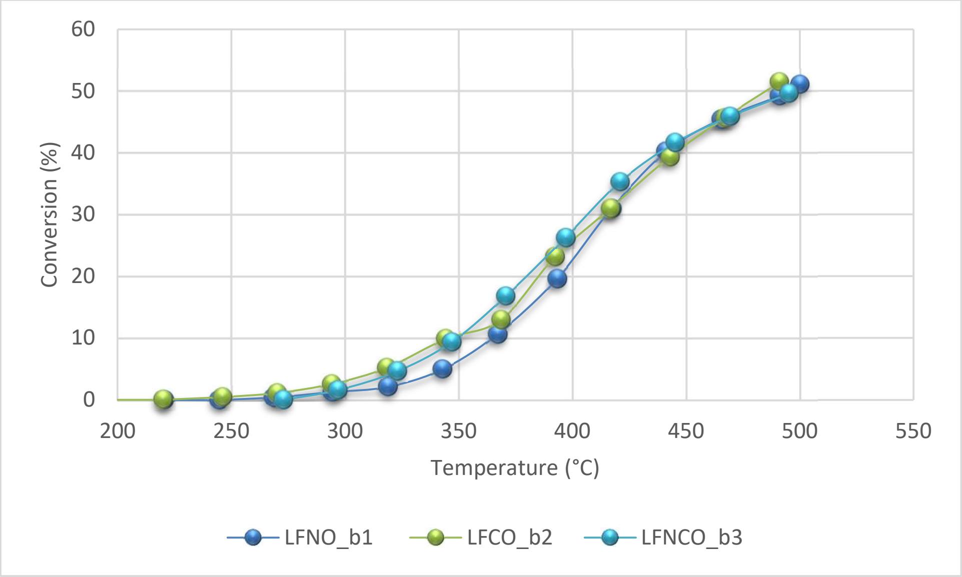

Figure 80: Conversion temperature graph for samples with different drugs (LFNO_b1, LFCO_b2 and LFNCO_b3), whose dopants were deposited during synthesis

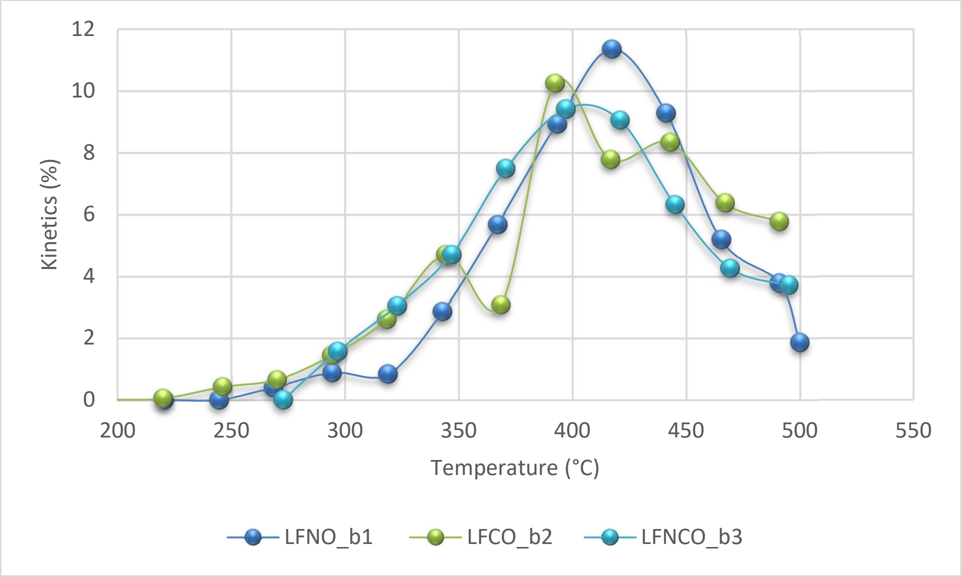

Figure 81: differential conversion-temperature plot for samples obtained by exsolution from the precursor perovskite and characterized by different dopings (LFNO_b1, LFCO_b2 and LFNCO_b3)

The sample activated with Ni is more efficient at higher temperatures.

The Cu doped sample showed an irregular behavior as a function of temperature (figure 82): it is considered implausible that this behavior is characteristic of the catalyst and is rather due to an experimental error. This makes also difficult to evaluate the effect of the different preparation procedure. The co-doping wirh barium, however, seems to favor the catalytic activity only at 470-500°C.

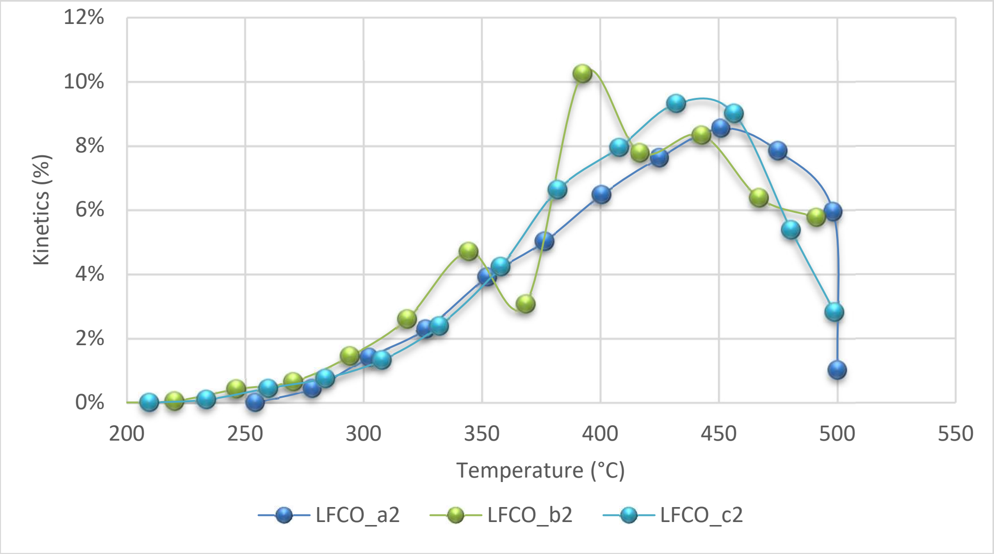

Figure 82: Conversion-temperature differential plot for Cu-doped samples (LFCO_a2, LFCO_b2 and LBFCO_c2)

As reported by Toniolo et al. in 2012 (48), the number of oxygen species affects the catalytic activity to some extent, and the conversion of carbon dioxide demonstrates that the doped catalyst increases the number of oxygen species on the surface by promoting the combination of CO_2 with hydrogen, thus agreement with XPS results.

The mechanism behind higher reaction efficiency of A doped samples is also proposed by Lim et al in 2021 (49) during investigations of the impact of doping on CO_2 hydrogenation: after exsolution, Ba and the different catalysts (Ni, Cu and NiCu) are completely reduced to metal, and CO_2 molecules undergo methanation following the dissociative hydrogenation of the Ba- junction nanoparticle to form methane. At 600°C the LBFNO_c1, LBFCO_c2 and LBFNCO_c3 samples were reduced in such a way as to expose the active site of the metal nanoparticles, which favored the combination of carbon dioxide with hydrogen.

As reported by Fan and Tahir in 2021 (50) during investigations about the impact of metals on CO_2 hydrogenation, metallic Ni is more active than metallic Cu during methane production, therefore the activity of the nickel-doped perovskite is better than the copper-doped one (Fig. 83): it is however interesting to note that metallic

Cu allows to achieve its maximum yield from low temperatures (300 °C), with minimal variations as the temperature increases.

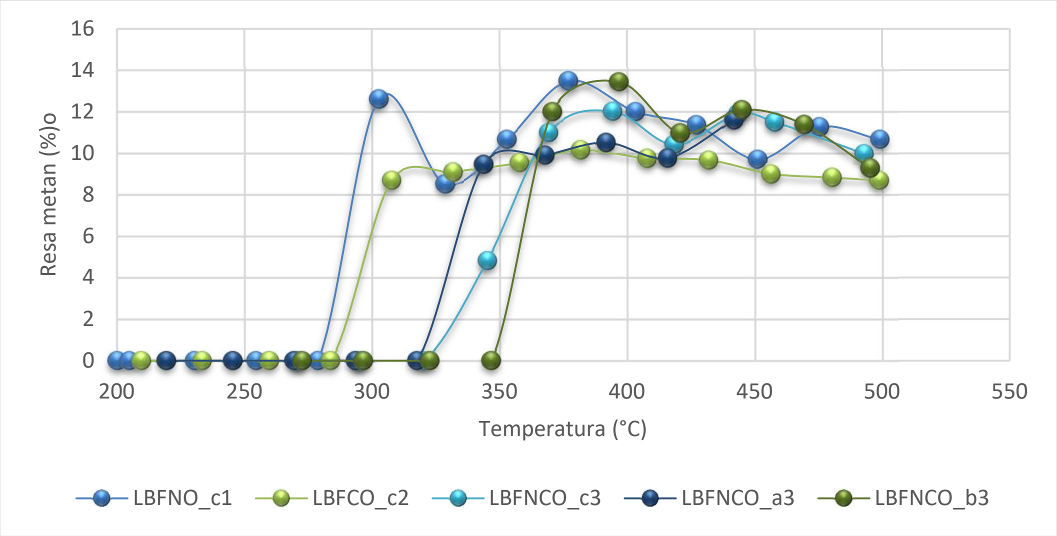

Figure 83: absolute methane-temperature yield graph for doped samples LBFNO_a3, LFCO_b3, LBFNO_c1, LBFCO_c2 and LBFNCO_c3

By comparing the selectivity of the conversion reaction of CO_2 to methane (understood as the percentage of methane produced on the amount of CO_2 converted), it is interesting to note that the reaction is fairly selective (percentages from 60% upwards) in the temperature range between 300 °C and 370 °C (Figure 84): above these temperatures, the production of CO prevails. It is also interesting to note that the Cu-doped sample has better selectivity from low temperatures (300°C) and maintains this selectivity over a wide temperature range (up to 400°C).

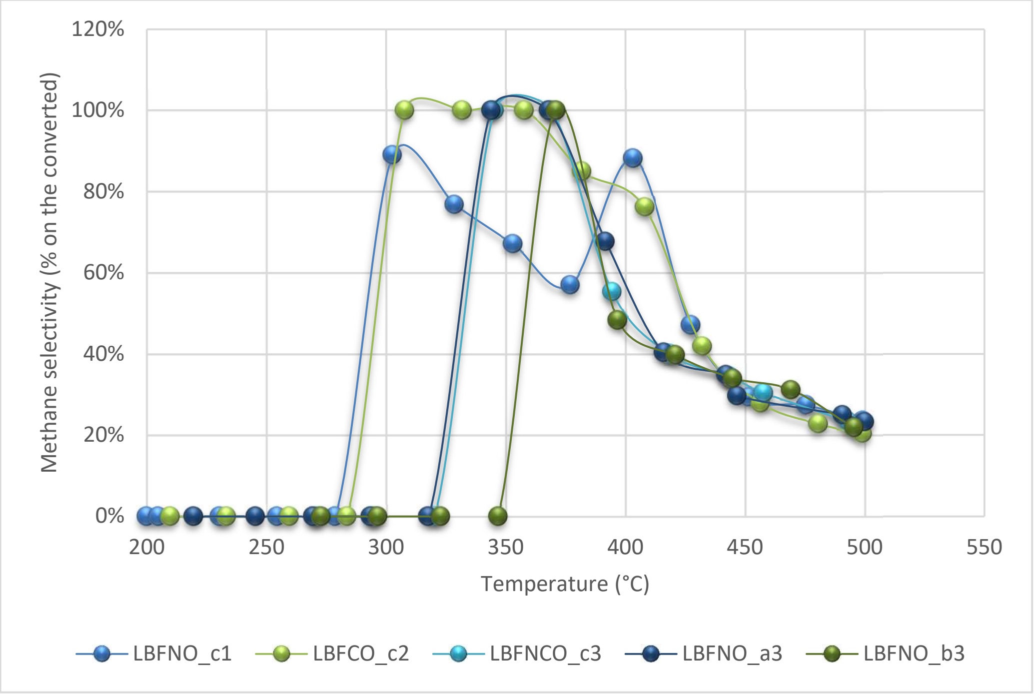

Figure 84: temperature selectivity of the reaction for doped samples LFNCO_a3, LFNCO_b3, LBFNO_c1, LBFCO_c2 and LBFNCO_c3

However, in the thermocatalytic hydrogenation of CO_2 to methane, the main byproduct affecting methane selectivity is CO, so it is necessary to reduce the conversion of CO_2 to CO and thus improve the selectivity of CH4. As can be seen in Fig. 85a and 85b, carbon monoxide is the main product above 400°C, with a CO percentage above 50%.

A limited production of CO (Fig. 85a) or the absence of CO (Fig. 85b) is observed for temperatures below 350 – 400 °C: above this temperature, there is a significant increase in the production of CO, with significant dilution of the methane produced.

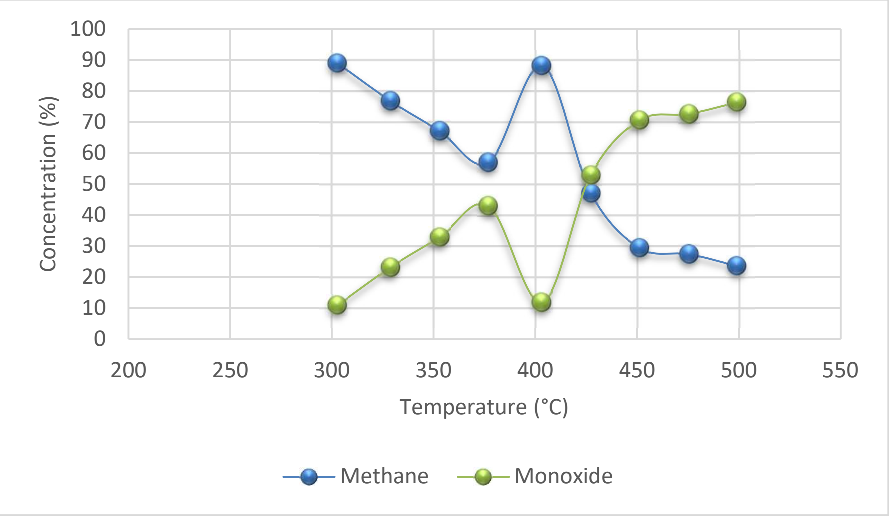

Figure 85a: concentration-temperature comparison for methane and monoxide species in the LBFNO_c1 sample

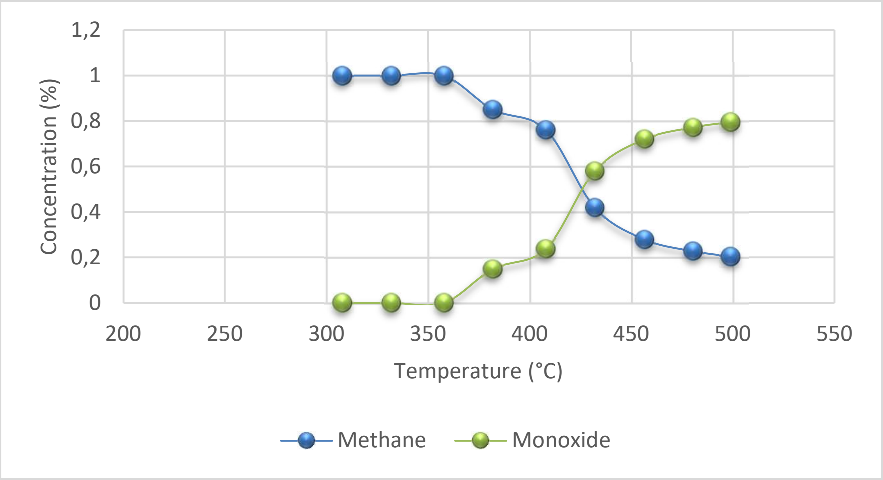

Figure 85b: concentration-temperature comparison for methane and monoxide species in the LBFCO_c2 sample

In conclusion it can be stated that:

- the sample doped in A with barium and in B with copper is the best from the point of view of the production of methane, as it allows to obtain a discrete quantity of CH_4 even in a very wide range of temperatures (Fig. 8).
- The different synthesis method does not have great influence on the conversion of CO_2, however it has been observed that the samples in which the catalyst precursors have been introduced directly into the synthesis mixture are more stable.

- As regards the conversion of CO_2, the catalysts work in approximately the same way by converting approximately 50% of the carbon dioxide introduced into the reactor, but in any case the best results are obtained in a temperature range between 350°C and 450°C.
- For the production of methane it is convenient to dope the perovskite also in A: the doping with barium has allowed to obtain CH_4 even with only nickel nanocatalysts and only copper nanocatalysts, which have given a better selectivity for methane. However, without doping in A, it is possible to produce methane by exploiting the NiCu alloy as catalyst, which however has a lower selectivity.

IV. Conclusions

Many disciplines and topics have converged in this project: from environmental knowledge, in fact, chemistry and materials science have been called to address both the issue of sustaining energy production and reducing CO_2 emissions through heterogeneous catalysis systems.

In order to facilitate the industrial preparation of perovskitic catalysts, the project was developed considering the design of the materials involved in the reactions, by adopting “poor” raw materials instead of expensive ones. For all synthesis methods, an extensive material characterization was performed in order to rationalize the result of catalytic tests.

Both enviromental and technical challenges were therefore addressed, by developing and optimizing nanocatalyst-supported materials capable of efficiently converting carbon dioxide to methane by thermal catalysis, with little to no amounts of by-products such as carbon monoxide and methanol. This project regarded the assessment of the impact of perovskite doping on its capacity to reduce CO_2 and to produce CH_4: doping of perovskite through Ni, Cu and NiCu nanoparticles was achieved through different techniques such as template impregnation and exsolution.

The interaction between the active catalyst and the perovskite support is the main factors which was accounted for. Besides, sustainability of material production was another crucial issue to consider: therefore, an active effort is made to reduce the amount of catalyst needed.

The results are promising: a careful tuning of the interaction between support and supported metal can enhance the characteristics of the catalyst with surprising results, even at atmospheric pressure and low temperatures (below 400°C).

All doped samples displayed notable performance, with a CO_2 reduction efficiency around 50%. In some cases, methane has been successfully produced, with a yield around 8%-12%.

Catalytically active materials were obtained introducing catalysts on the surface or in the bulk of the perovskite: in this last case the active nanoparticles were extracted from the material by exsolution.

Extensive characterization was also performed to gather information on structure, composition and micromorphology through SEM measurements and reductive functionality. Lastly, catalytic tests were performed to evaluate the samples in terms of CO_2 reduction capacity and CH_4 production capacity.

The synthetic procedures employed here have proven effective:

1. SEM-EDX images show homogeneous samples.
2. Reduction tests performed at 600°C with a hydrogen concentration of 5% showed that the nanocatalysts are completely reduced to their metallic oxidation state, under the correct exsolution conditions. However, the XRD reduction result performed before and after the reduction tests does not confirm Ni, Cu and NiCu. XPS analysis was also performed to evaluate post catalytic coking, which occurred to a small degree for all samples

In conclusion, stable materials displaying the presence of nanocatalyst particles on the surface were successfully produced.

The catalytic performance of the obtained materials is rather good:

- Slightly higher conversion of CO_2 was achieved by B-doped samples, almost regardless of the catalyst used, with a minimum process temperature of 300°C and the optimal temperature ranging between 350°C and 450°C.
- Synthesis methodology does not highly impact CO_2 reduction. However, samples doped by template impregnation performed slightly worse: this may be due to the presence of the nanoparticles on the surface, making them less stable.
- The Ni-Cu alloy doped samples showed a good capacity to produced CH_4
- A-doped samples with Barium were able to produce methane regardless of the nanocatalyst in the B site.
- Among A-doped samples, single metal B-doped samples achieved the best performances; in particular:
    - nickel allows to obtain large quantities of methane (about 13%) starting from low temperatures (300°C), but performance quickly decreases at higher temperatures;

- copper performed slightly worse than Nickel, but its performance remained consistent throughout a wide temperature range (from 310°C to 500°C).

V. Bibliography

(1) Hepburn, C.; Adlen, E.; Beddington, J.; Carter, E. A.; Fuss, S.; Mac Dowell, N.; Minx, J. C.; Smith, P.; Williams, C. K. The Technological and Economic Prospects for CO2 Utilization and Removal. *Nature* **2019**, *575* (7781), 87–97. https://doi.org/10.1038/s41586-019-1681-6.

(2) Quéré, C.; Andrew, R.; Friedlingstein, P.; Sitch, S.; Hauck, J.; Pongratz, J.; Pickers, P.; Ivar Korsbakken, J.; Peters, G.; Canadell, J.; Arneth, A.; Arora, V.; Barbero, L.; Bastos, A.; Bopp, L.; Ciais, P.; Chini, L.; Ciais, P.; Doney, S.; Gkritzalis, T.; Goll, D.; Harris, I.; Haverd, V.; Hoffman, F.; Hoppema, M.; Houghton, R.; Hurtt, G.; Ilyina, T.; Jain, A.; Johannessen, T.; Jones, C.; Kato, E.; Keeling, R.; Klein Goldewijk, K.; Landschützer, P.; Lefèvre, N.; Lienert, S.; Liu, Z.; Lombardozzi, D.; Metzl, N.; Munro, D.; Nabel, J.; Nakaoka, S. I.; Neill, C.; Olsen, A.; Ono, T.; Patra, P.; Peregon, A.; Peters, W.; Peylin, P.; Pfeil, B.; Pierrot, D.; Poulter, B.; Rehder, G.; Resplandy, L.; Robertson, E.; Rocher, M.; Rödenbeck, C.; Schuster, U.; Skjelvan, I.; Séférian, R.; Skjelvan, I.; Steinhoff, T.; Sutton, A.; Tans, P.; Tian, H.; Tilbrook, B.; Tubiello, F.; Van Der Laan-Luijkx, I.; Van Der Werf, G.; Viovy, N.; Walker, A.; Wiltshire, A.; Wright, R.; Zaehle, S.; Zheng, B. Global Carbon Budget 2018. *Earth Syst. Sci. Data* **2018**, *10* (4), 2141–2194. https://doi.org/10.5194/essd-10-2141-2018.

(3) Thema, M.; Bauer, F.; Sterner, M. Power-to-Gas: Electrolysis and Methanation Status Review. *Renewable and Sustainable Energy Reviews*. Elsevier Ltd September 1, 2019, pp 775–787. https://doi.org/10.1016/j.rser.2019.06.030.

(4) Wang, W.; Gong, J. Methanation of Carbon Dioxide: An Overview. *Front. Chem. Eng. China* **2011**, *5* (1), 2–10. https://doi.org/10.1007/s11705-010-0528-3.

(5) Vogt, C.; Monai, M.; Kramer, G. J.; Weckhuysen, B. M. The Renaissance of the Sabatier Reaction and Its Applications on Earth and in Space. *Nat. Catal.* **2019**, *2* (3), 188–197. https://doi.org/10.1038/s41929-019-0244-4.

(6) Rönsch, S.; Schneider, J.; Matthischke, S.; Schlüter, M.; Götz, M.; Lefebvre, J.; Prabhakaran, P.; Bajohr, S. Review on Methanation - From Fundamentals to Current Projects. *Fuel* **2016**, *166*, 276–296. https://doi.org/10.1016/j.fuel.2015.10.111.

(7) Mykhailo Pidburtnyi, Bryan Zanca, Claude Coppex, Santiago Jimenez-Villegas, and Venkataraman Thangadurai; A Review on Perovskite-Type LaFeO3 Based Electrodes for CO2 Reduction in Solid Oxide Electrolysis Cells: Current

Understanding of Structure–Functional Property Relationships **2021**, 33, 12, 4249–4268. https://doi.org/10.1021/acs.chemmater.1c00771

(8) Goldschmidt, V. M. Die Gesetze Der Krystallochemie. Naturwissenschaften 1926, 14 (21), 477−485.

(9) Falcón, H.; Goeta, A. E.; Punte, G.; Carbonio, R. E. Crystal Structure Refinement and Stability of LaFexNi1-XO3Solid Solutions. J. Solid State Chem. 1997, 133 (2), 379−385.

(10) Selbach, S. M.; Tolchard, J. R.; Fossdal, A.; Grande, T. Non-Linear Thermal Evolution of the Crystal Structure and Phase Transitions of LaFeO 3 Investigated by High Temperature X-Ray Diffraction. J. Solid State Chem. 2012, 196, 249−254.

(11) Gateshki, M.; Suescun, L.; Kolesnik, S.; Mais, J.; Świerczek, K.; Short, S.; Dabrowski, B. Structural, Magnetic and Electronic Properties of LaNi0.5Fe0.5O3 in the Temperature Range 5−1000 K. J. Solid State Chem. 2008, 181 (8), 1833−1839.

(12) S. G.A, Introduction to Surface Chemistry and Catalysis, Wiley, 1994.

(13) Shan He, Changming Li, Hao Chen, Dangsheng Su, Bingsen Zhang, Xingzhong Cao, Baoyi Wang, Min Wei, David G. Evans, and Xue Duan. A Surface Defect-Promoted Ni Nanocatalyst with Simultaneously Enhanced Activity and Stability. https://doi.org/10.1021/cm303517z

(14) Manoj B. Gawande, Anandarup Goswami,François-Xavier Felpin, Tewodros Asefa, Xiaoxi Huang, Rafael Silva, Xiaoxin Zou, Radek Zboril and Rajender S. Varma. Cu and Cu-Based Nanoparticles: Synthesis and Applications in Catalysis. https://doi.org/10.1021/acs.chemrev.5b00482

(15) Wang, H. Y., & Lua, A. C. (2015). Methane decomposition using Ni–Cu alloy nano-particle catalysts and catalyst deactivation studies. Chemical Engineering Journal, 262, 1077–1089. https://doi.org/10.1016/j.cej.2014.10.063

(16) A. Mishra and R. Prasad, "Preparation and application of perovskite catalysts for diesel soot emissions control: An overview", Catal. Rev. - Sci. Eng., vol. 56, no. 1, pp. 57–81, 2014, doi: 10.1080/01614940.2014.866438.

(17) Dragos Neagu, Vasileios Kyriakou, Ioan-Lucian Roiban, Mimoun Aouine, Chenyang Tang, Angel Caravaca, Kalliopi Kousi, Ingeborg Schreur-Piet, Ian S. Metcalfe, Philippe Vernoux, Mauritius C. M. van de Sanden, and Mihalis N.

Tsampas. In Situ Observation of Nanoparticle Exsolution from Perovskite Oxides: From Atomic Scale Mechanistic Insight to Nanostructure Tailoring

(18) M A Moram and M E Vickers 2009 Rep. Prog. Phys. 72 036502. X-ray diffraction of III-nitrides

(19) M. Pennetta, A. Trocciola, 2017, "Sinuessa , Un Approdo Sommerso Di Epoca Romana", Enea.

(20) B.E. Warren (1941). X-Ray Diffraction Methods., 12(5), 375-. Doi: 10.1063/1.1712915

(21) Giordano, F., Trovarelli, A., de Leitenburg, C., & Giona, M. (2000). A Model for the Temperature-Programmed Reduction of Low and High Surface Area Ceria. Journal of Catalysis, 193(2), 273–282. doi:10.1006/jcat.2000.2900

(22) MONTI, D. (1983). Temperature-programmed reduction. Parametric sensitivity and estimation of kinetic parameters. Journal of Catalysis, 83(2), 323–335. doi:10.1016/0021-9517(83)90058-1

(23) Bradbury, S., Bracegirdle, B., 1998. Introduction to Light Microscopy, second ed. BIOS.

(24) Mertz, J., 2009. Introduction to Optical Microscopy. Roberts and Company Publishers. ISBN: 13: 978-0981519487.

(25) Reimer, L., Kohl, H., 2008. Transmission Electron Microscopy: Physics of Image Formation, fifth ed. Springer. ISBN: 13: 978-0387400938.

(26) Spence, J.C.H., 2013. High-resolution Electron Microscopy, fourth ed. Oxford University Press. ISBN: 13: 978-0199552757.

(27) Stokes, D., 2008. Principles and Practice of Variable Pressure: Environmental Scanning Electron Microscopy. Wiley-Blackwell. ISBN: 13: 978-0470065402.

(28) Egerton, R., 2011. Electron Energy-loss Spectroscopy in the Electron Microscope, second ed. Springer Handbooks. ISBN: 978-1-4419-9583-4.

(29) Pennycook, S.J., Nellist, P.D. (Eds.), 2011. Scanning Transmission Electron Microscopy: Imaging and Analysis. Springer.

(30) Williams, D.B., Carter, C.B., 2009. Transmission Electron Microscopy. Springer.

(31) Kuo, J. (Ed.), 2014. Electron Microscopy: Methods and Protocols (Methods in Molecular Biology), third ed. Humana Press. ISBN: 13: 978-1627037754.

(32) Goldstein, J., Newbury, D.E., Joy, D.C., Lyman, C.E., Echlin, P., Lifshin, E., et al., 2007. Scanning Electron Microscopy and X-ray Microanalysis, third ed. Springer.

(33) ISO 22309:2011 Microbeam Analysis—Quantitative Analysis Using Energy-Dispersive Spectrometry (EDS) for Elements With an Atomic Number of 11 (Na) or Above. Geneva, Switzerland: ISO.

(34) J. Mielke, S. Rades, E. Ortel, T. Salge, V.-D. Hodoroaba, Improved spatial resolution of EDX/SEM for the elemental analysis of nanoparticles, Microsc. Microanal. 21 (Suppl. 3) (2015) 1713–1714.

(35) V.-D. Hodoroaba, C. Motzkus, T. Mace, S. Vaslin-Reimann, Performance of high-resolution SEM/EDX systems equipped with transmission mode (TSEM) for imaging and measurement of size and size distribution of spherical nanoparticles, Microsc. Microanal. 20 (2014) 602–612.

(36) V.-D. Hodoroaba, S. Rades,W.E.S. Unger, Inspection of morphology and elemental imaging of single nanoparticles by high-resolution SEM/EDX in transmission mode, Surf. Interface Anal. 46 (2014) 945–948.

(37) N. Ritchie, DTSA-II available free at, www.cstl.nist.gov/div837/837.02/epq/dtsa2/index.html

(38) R. G. Steinhardt and E. J. Serfass, Anal. Chem. 23, 1585 (1951).

(39) Fred A. Stevie, and Carrie L. Donley (2020). doi.org/10.1116/6.0000412. Introduction to x-ray photoelectron spectroscopy

(40) M. P. Seah and W. A. Dench, Surf. Interface Anal. 1, 2 (1979).

(41) C. J. Powell, J. Vac. Sci. Technol. A 38, 023209 (2020).

(42) J. F. Watts and J. Wolstenholme, An Introduction to Surface Analysis by XPS and AES (Wiley, Chichester, 2020), p. 19.

(43) J. F. Watts and J. Wolstenholme, An Introduction to Surface Analysis by XPSand AES (Wiley, Chichester, 2020), p. 47.

(44) J. Wu, J.P. Dacquin, N. Djelal, C. Cordier, C. Dujardin, P. Granger, Calcium and copper substitution in stoichiometric and La-deficient LaFeO3 compositions: a

starting point in next generation of three-way-catalysts for gasoline engines, Appl. Cat. B: Environ. 282 (2021), 119621, https://doi.org/10.1016/j.

(45) Spinicci, R., Tofanari, A., Delmastro, A., Mazza, D., & Ronchetti, S. (2002). Catalytic properties of stoichiometric and non-stoichiometric LaFeO3 perovskite for total oxidation of methane. Materials Chemistry and Physics, 76(1), 20–25. doi:10.1016/s0254-0584(01)00498-9

(46) Kaiwen, Z., Xuehang, W., Wenwei, W., Jun, X., Siqi, T., & Sen, L. (2013). Nanocrystalline LaFeO3 preparation and thermal process of precursor. Advanced Powder Technology, 24(1), 359–363. doi:10.1016/j.apt.2012.08.009

(47) J.M. Giraudon, A. Elhachimi, G. Leclercq, Catalytic oxidation of chlorobenzene over Pd/perovskites, Appl. Catal. B 84 (2008) 251–261.

(48) F.S. Toniolo, R.N.S.H. Magalh˜ aes, C.A.C. Perez, M. Schmal, Structural investigation of LaCoO3 and LaCoCuO3 perovskite-type oxides and the effect of Cu on coke deposition in the partial oxidation of methane, Appl. Catal. B-Environ. 117–118 (2012) 156–166.

(49) H.S. Lim, M. Lee, Y. Kim, D. Kang, J.W. Lee, Low-temperature CO2 hydrogenation to CO on Ni-incorporated LaCoO3 perovskite catalysts, Int. J. Hydrog. Energy 46 (2021) 15497–15506.

(50) W.K. Fan, M. Tahir, Recent trends in developments of active metals and heterogenous materials for catalytic CO2 hydrogenation to renewable methane: a review, J. Environ. Chem. Eng. 9 (2021), 105460.

Ringraziamenti

Ringrazio la Prof.ssa Antonella Glisenti per avermi seguita in questi mesi senza mai farmi mancare il suo sostegno e i suoi preziosi consigli, aiutandomi e accompagnandomi nella realizzazione della tesi.

Un ringraziamento speciale al gruppo di ricerca IMPACT che in questo lavoro ha avuto un ruolo fondamentale: mi ha accompagnata passo a passo in questo percorso, insegnandomi e chiarendomi dubbi e incertezze ogni qualvolta ne ho avuto bisogno.

Un immenso grazie alla mia psicologa, la dott.ssa Martina Frascara e al centro formazione Wonderful, per avermi aiutato a capire quanto valgo e a tirare fuori il meglio di me.

Ai miei genitori, che sono il mio punto di riferimento e che mi hanno sostenuta sia economicamente che emotivamente e che mi hanno permesso di percorrere e concludere questo cammino.

A mio fratello Emanuele (Grazie, Graziano, Grazie al ca***, cit.) e a mia cognata Alice, che nel momento peggiore mi hanno aiutato a uscire dalla situazione in cui mi trovavo.

Grazie perché senza di voi non sarei mai arrivata fino in fondo a questo difficile, lungo e tortuoso cammino. Questa tesi la dedico a voi che siete la mia famiglia, il mio più grande sostegno e la mia guida.

Voglio ringraziare una persona unica e speciale, Alessandro, il mio ragazzo. Grazie per essere stato sempre il mio fan #1, grazie per essere sempre stato al mio fianco in ogni momento e anche oggi, in questo giorno importante, sei qui con me a festeggiare insieme questo traguardo.

Grazie a tutti i miei amici: gli ingegneri dell’unipd per avermi fatto passare serate di spensieratezza e avermi reso tutto più leggero, e i corvi perché nonostante la distanza mi hanno sempre sostenuto.

Grazie a Davide perché la nostra amicizia poggia su solidissime basi: l’oroscopo e il fondamentale invio quotidiano di meme e reels molto stupidi.

Infine, grazie a me, perché se io per prima non ci avessi creduto fino alla fine, questo traguardo non lo avrei mai raggiunto.

Nella speranza che questo traguardo possa essere l'inizio di una lunga e brillante carriera,

GRAZIE

Gruppo di ricerca IMPACT